A CALORIMETER FOR THE STUDY OF PHOTOPRODUCTION AT HIGH TRANSVERSE MOMENTUM

A Thesis Submitted for the Degree of

DOCTOR OF PHILOSOPHY

in the

UNIVERSITY OF LONDON

by

R. M. NAMJOSHI

Blackett Laboratory
Imperial College of Science and Technology
South Kensington
London S.W.7

November, 1982.

ABSTRACT

This thesis describes the operation of a lead-scintillator sandwich electromagnetic calorimeter used in the NA-14 photoproduction experiment at the CERN SPS.

A review of the principles of calorimetry and details of the performance of the calorimeter in a test beam are presented. The computer aided online monitoring facilities and the offline photon reconstruction procedures are described. Finally, preliminary results are presented on the inclusive high P_t ($\geq$ 1.65 GeV/c) spectrum of photoproduced neutral pions reconstructed by the calorimeter.

ACKNOWLEDGEMENTS

I would like to express my thanks to the following people for their assistance during my period of research.

J. P. Astbury, my supervisor.

All members of the NA-14 collaboration, especially A. Duane, P. Kyberd, I. Siotis and D. M. Websdale for guidance and numerous enlightening discussions.

I. Butterworth for the opportunity of working with the High Energy Nuclear Physics group of Imperial College.

My parents for their continued support and encouragement.

This thesis was printed on the IBM 3800 Laser Printer Subsystem at CERN, Geneva. The formatting of the text was performed by the SYSPUB and SCRIPT programs of the University of Waterloo, Ontario. Most of the diagrams were produced using the CERN histogram and graphics packages HBOOK, HPLOT and HTV.

CONTENTS

ABSTRACT ii

ACKNOWLEDGEMENTS iii

CONTENTS iv

LIST OF FIGURES vi

LIST OF TABLES viii

Chapter page

I. INTRODUCTION 1

- Background 1
- Photon Hard Scattering 2
- The NA-14 Experiment 5
  - A Description of the Spectrometer 7
  - The Tagged Photon Beam 9

II. CALORIMETRY 15

- Electromagnetic Showers 16
  - Analytic Calculations 18
  - Longitudinal Development 20
  - Lateral Development 24
  - Transition Effects 29
  - Energy Resolution 31
- Hadronic Showers 38
- Position Measurements in Electromagnetic Calorimeters 42
- Particle Identification 45

III. ILSA-THE IMPERIAL COLLEGE LEAD SCINTILLATOR ARRAY 47

- The H5 Tests 51
  - Experimental Layout 51
  - Data Acquisition 53
  - Calibration and Monitoring 53
  - Linearity and Energy Resolution of ILSA 54
  - Linearity of Ariadne 59
  - Position Resolution 62
  - Attenuation Corrections 67
  - Electron-Hadron Separation 69
  - Conclusions 75
- ILSA at NA-14 75

Layout 77
Electronics 79
The High Voltage System 80
The Photon Trigger 81

IV. DATA ACQUISITION AND ONLINE MONITORING 85

The Monitoring Computer 85
The Data Acquisition System 87
Triggers 87
Event Readout 90
Start of Run Operations 93
Monitoring Tasks 94

V. PHOTON RECONSTRUCTION 99

Ariadne Clusterization 100
Cluster Association and Energy Sharing 101
The Pizero 106
Pattern Recognition Inefficiencies 113
Reconstruction Efficiency 119

VI. PRELIMINARY RESULTS 123

Data Analysis 123
The Inclusive π^0 P_t Spectrum 126
Conclusions 126

LIST OF FIGURES

Figure		Page
1.1	Photon scattering diagrams	4
1.2	Photon structure function	6
1.3	The NA-14 Spectrometer	8
1.4	Photon beam production	10
1.5	Photon beam energy spectrum	13
2.1	Fractional useful track length as a function of E_c/ϵ	21
2.2	Longitudinal energy deposition for EM showers	23
2.3	Lateral energy deposition for EM showers	27
2.4	Integrated lateral shower profile	28
2.5	Volume that contains 95% of the shower energy	34
2.6	Angular distribution of shower electrons	35
2.7	Centre of gravity vs. true shower position	44
3.1	Structure of an ILSA module	48
3.2	Structure of an Ariadne module	50
3.3	The H5 test setup	52
3.4	A, B, C, D Pulseheights 6 GeV electrons	55
3.5	ILSA energy resolution 6 GeV electrons	57
3.6	ILSA fractional energy resolution vs. energy	58
3.7	ILSA linearity	60
3.8	Lateral shower profile at various energies	61
3.9	Exponential fit to the lateral shower profile	63
3.10	Ariadne number of particles vs. energy	64

Figure		Page
3.11	Centre of gravity distribution 6 GeV electrons	66
3.12	Ariadne attenuation curve	68
3.13	Visible energy 6 GeV electrons and hadrons	70
3.14	A+C vs. B+D 6 GeV electrons	71
3.15	A+C vs. B+D 6 GeV hadrons	72
3.16	NA-14 Calorimeter acceptance	76
3.17	Layout of an ILSA quadrant	78
4.1	PDP 11/34 hardware configuration	86
4.2	Computer trigger logic	89
4.3	Event readout flowchart	92
5.1	Trigger photon energy spectrum	104
5.2	Trigger photon P_t spectrum	105
5.3	γ-γ effective mass distribution	107
5.4	π^0 energy spectrum	109
5.5	π^0 P_t spectrum	110
5.6	π^0 decay photon asymmetry	112
5.7	Cluster Y separation vs. Z separation	114
5.8	π^0 decay photon azimuth	117
5.9	γ-γ effective mass for split clusters	118
6.1	ILSA inclusive π^0 P_t spectrum	127
6.2	OLGA inclusive π^0 P_t spectrum	128

LIST OF TABLES

Table		Page
1.1	NA-14 beam parameters	11
2.1	Properties of electromagnetic showers	22
2.2	Spatial development of EM showers	25
2.3	Factors limiting energy resolution for EM calorimeters	32
2.4	Properties of hadronic showers	39
3.1	ILSA energy resolution and linearity	59
3.2	Ariadne position resolution vs. energy	65
3.3	Centre of gravity vs. true shower position	67
3.4	Hadron rejection as a function of energy	74
5.1	π^0 reconstruction statistics	120

Chapter I

INTRODUCTION

1.1 Background

Over the past few years several experiments have provided evidence supporting the view that the strong interactions of sub-atomic particles can be described within the framework of Quantum Chromodynamics (QCD). QCD is an SU3 symmetric field theory in which hadrons are constructed out of a limited number of quark types or flavours. In addition, each quark flavour posseses the quantum number of colour, an extra degree of freedom that allows a state consisting of three otherwise identical quarks to have an overall antisymmetric wave function. In order to make the SU3 symmetry of colour 'local' (gauging of the colour charge) it is necessary to introduce an octet of massless coloured vector bosons; the gluons.

Interactions between coloured objects (quarks and gluons) are mediated by the exchange of gluons in much the same way as the interactions between electrically charged particles are mediated by photon exchange in Quantum Electrodynamics (QED). There is, however, one important difference; the gluons themselves carry colour and can thus interact amongst themselves. A consequence of this is 'asymptotic freedom'; the effective coupling between the fields decreases at short distances (large momentum transfers). A field theoretical analysis of hadron-hadron interactions is plagued by severe 'technical' difficulties, however, it has been conjectured (eg. see [ELL]) that it may be possible to exploit the asymptotic freedom of QCD and use a perturbation theory approach to make predictions about large transverse momentum final states. In this hard scattering model, the interaction between hadrons is dominated by the large angle scattering of the hadronic constituents at sufficiently large values of the constituent centre of mass energy.

The use of this model has enabled many predictions to be made on processes such as inclusive hadron and jet production in proton-proton interactions (eg. see [FEY77], [FEY78]) and much experimental effort has been directed towards testing these predictions. These experiments have provided answers to many questions but much remains to be learned about the nature of the strong interaction and the structure of hadrons.

1.2 Photon Hard Scattering

Interest in the study of high P_t processes involving real photons is due mainly to the fact that unlike hadrons, the photon can act like an elementary object and couple directly with a quark in a point-like manner. Since the energy of the photon does not have to be shared amongst constituent quarks, it is more efficient than a hadron in the production of high P_t secondaries and is a useful tool for probing the structure of the hadron in order to test the predictions of QCD. The lowest order diagrams in which the photon couples directly to a quark are shown in Figure 1.1a. In the QED Compton process, the photon interacts with a quark to give a final state consisting of a quark and a photon. The QCD Compton process is identical except that the final state photon is replaced by a gluon. In the photon-gluon fusion process, the photon interacts with a gluon via a quark-antiquark pair to give a final state consisting of a quark and an antiquark. The presence of the strong coupling constant α_s in the second vertex of the last two processes means that they dominate over the QED Compton process.

In addition to its point like coupling, the photon can also materialize into a quark-antiquark pair before the interaction. The quark-antiquark pair can radiate gluons and thus the photon can also serve as a source of quarks and gluons. The distribution of quarks and gluons within the photon is expressed in terms of a structure function. This component of the photon has two distinct parts [WIT], [LLE]:

1. The perturbative (anomalous structure function) part in which the quark-antiquark pair do not interact with each other before the interaction with the target.
2. The hadronic part in which the quark-antiquark pair interact with each other via miltiple gluon exchange and build up a form factor. The photon then essentially behaves as a superposition of vector mesons (VMD : vector meson dominance).

Figure 1.1

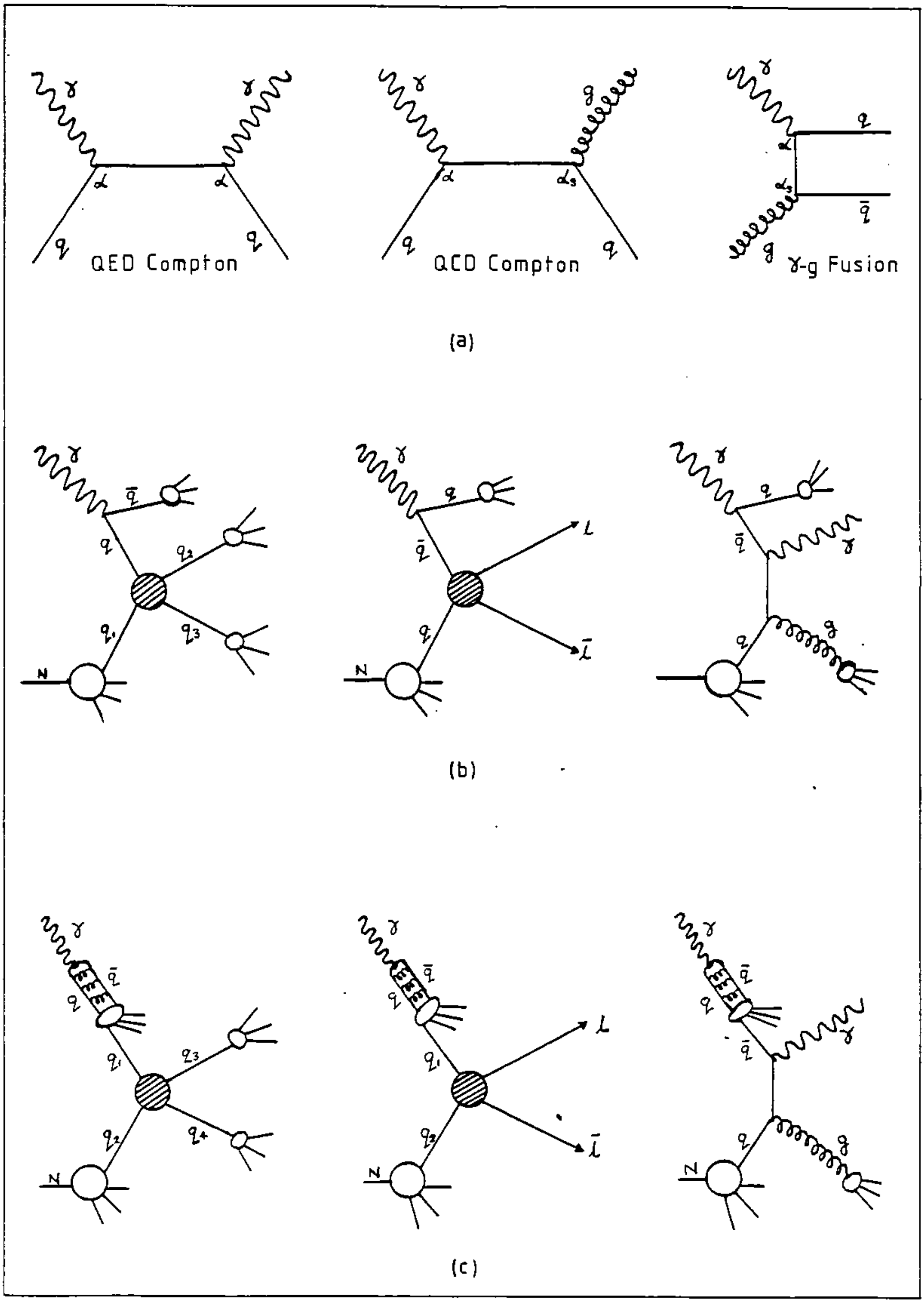

The lowest order diagrams in which the photon interacts by materializing into a quark-antiquark pair before interacting with the target are shown in Figures 1.1b and 1.1c.

The perturbative part is exactly calculable within QCD and grows like $\ln[Q^2]$ at large Q^2 to leading logarithmic order. It dominates over the non-perturbative or hadronic part except at very small values of x - Figure 1.2.

A study of the Compton QED and QCD processes is interesting for several reasons. Apart from testing the QCD prediction for the structure function of the photon it would also provide valuable information on the distribution of quarks and gluons within the nucleon and, via the measurement of an inclusive cross section, information on the fragmentation functions of quarks and gluons [IGU], [IGU80].

1.3 The NA-14 Experiment

The NA-14 experiment was set up to perform a program of photoproduction studies at the CERN SPS with particular emphasis on the study of the hard scattering of real photons.

At first it would concentrate on the QED Compton process by triggering on final states having a photon at high transverse momentum. Having understood the problems associated with isolating this process it would proceed to study the kinematically equivalent QCD Compton process in which the final state photon of the QED process is replaced by a gluon.

Figure 1.2

Photon Structure Function[IGU]

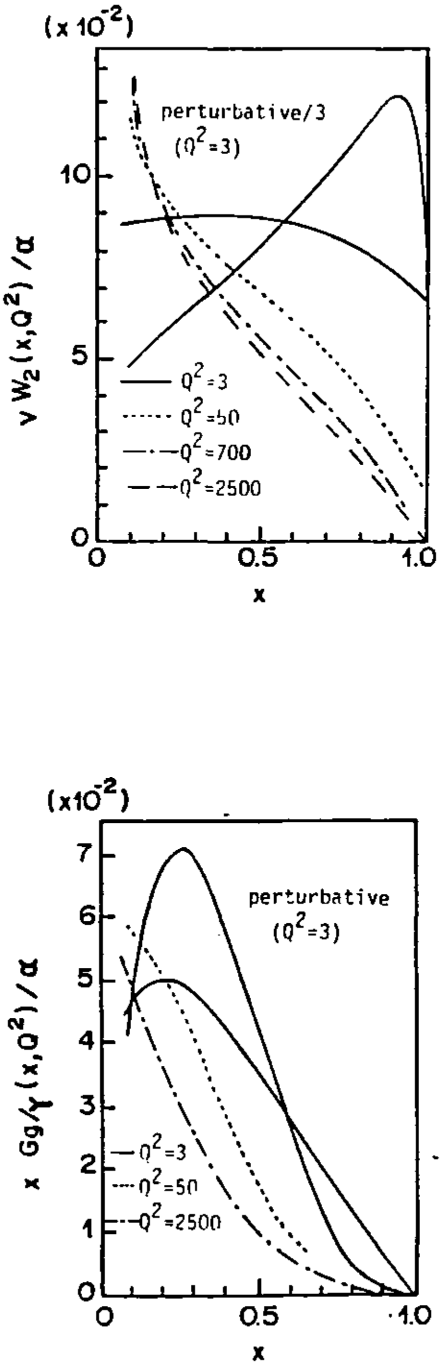

The study of these processes would require a high-intensity high-energy tagged photon beam and a spectrometer providing good e/γ detection and charged particle identification.

1.3.1 A Description of the Spectrometer

The layout of the NA-14 spectrometer is shown in Figure 1.3. It has two magnets with a total integrated field strength of 4 Tm. The AEG magnet serves to sweep away the electromagnetic background of soft ($\lesssim$ 100 MeV) electron positron pairs. It also deflects low momentum tracks so that their momentum can be measured. The Goliath magnet deflects higher momentum tracks. The trajectories of the charged tracks are measured by three stacks of Multiwire Proportional Chambers. These are located in field free regions to avoid the problem of spiralling soft electrons and positrons. The large chambers have a desensitized horizontal region in the median plane and this region is covered by small fast chambers. A hodoscopic Cerenkov counter provides K/π identification.

Good coverage for the detection of electrons and photons is provided by three electromagnetic calorimeters. The central lead-glass detector (OLGA) covers an acceptance of ± 80 mrad. Large angle (150-300 mrad) coverage is provided by the CROWN lead-glass calorimeter. The region in between is covered by a lead-scintillator sandwich calorimeter, ILSA, the subject of this thesis. Each of these calorimeters is equipped with two dimensional scintillator hodoscope arrays used to provide position measurements.

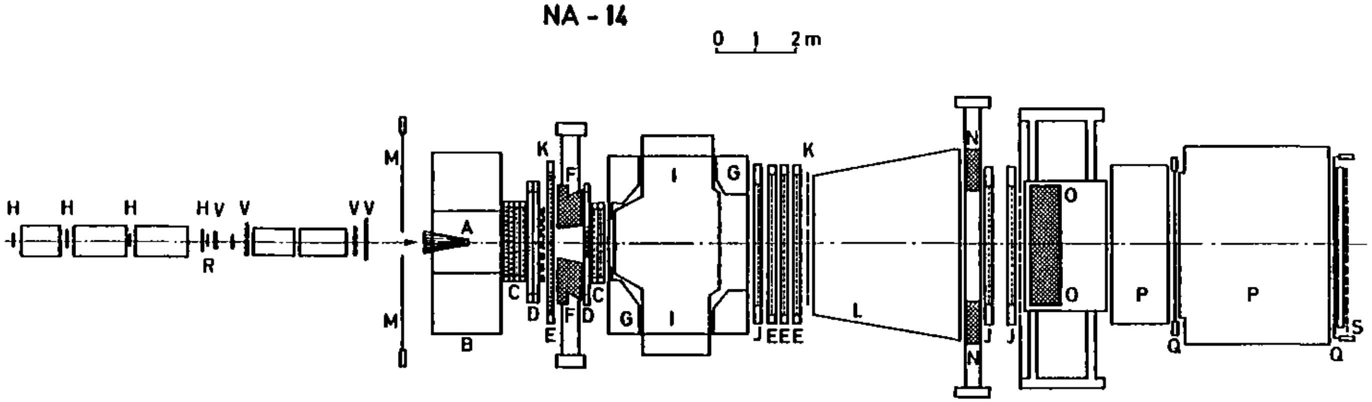

Figure caption:

H,V	tagging hodoscopes	F	"crown" lead glass calorimeter		
M	muon veto	G	Goliath Magnet		
A	active target	I,L	Čerenkov Counters	O	Olga-Penelope Calorimeter
B	AEG vertex magnet	K	trigger hodoscopes	P	iron filter
C,D,E,J	MWPC's	N	Imperial College Calorimeter	Q,S	μ hodoscopes

Experiment NA 14: Photoproduction at high energy and high intensity

Figure 1.3

An iron wall and scintillator hodoscopes located downstream of OLGA allow for the possibility of triggering on muons.

1.3.2 The Tagged Photon Beam

The high-energy and high-intensity photon beam used in the experiment is produced by what is known as the "Classical Two Step Method". The photon beam is obtained from the bremsstrahlung of a beam of electrons. The electron beam is derived from a primary photon beam produced by the decay of neutral pions. This method produces a photon beam with a very low hadron contamination ($\approx 10^{-5}$). The beam layout is shown in Figure 1.4 and its parameters are summarized in Table 1.1. Complete details of the beam production and the tagging system have been given elsewhere [WIN], [COU].

The first stage in the process is to produce a photon beam from the decay of neutral pions. Incident high energy (400 GeV) protons from the SPS interact with a 500 mm long Beryllium target. About 70% of the protons interact in the target. Amongst the secondary particles produced is a large number of neutral pions. These decay almost instantaneously into two photons. The length and composition of the production target is a compromise between efficient use of the incident protons and the loss of photons via pair production before they can emerge from the target.

Sweeping magnets just after the production target deflect all charged secondaries and the primary protons that have not interacted into a wall of iron 4 m thick. The neutral hadron contamina-

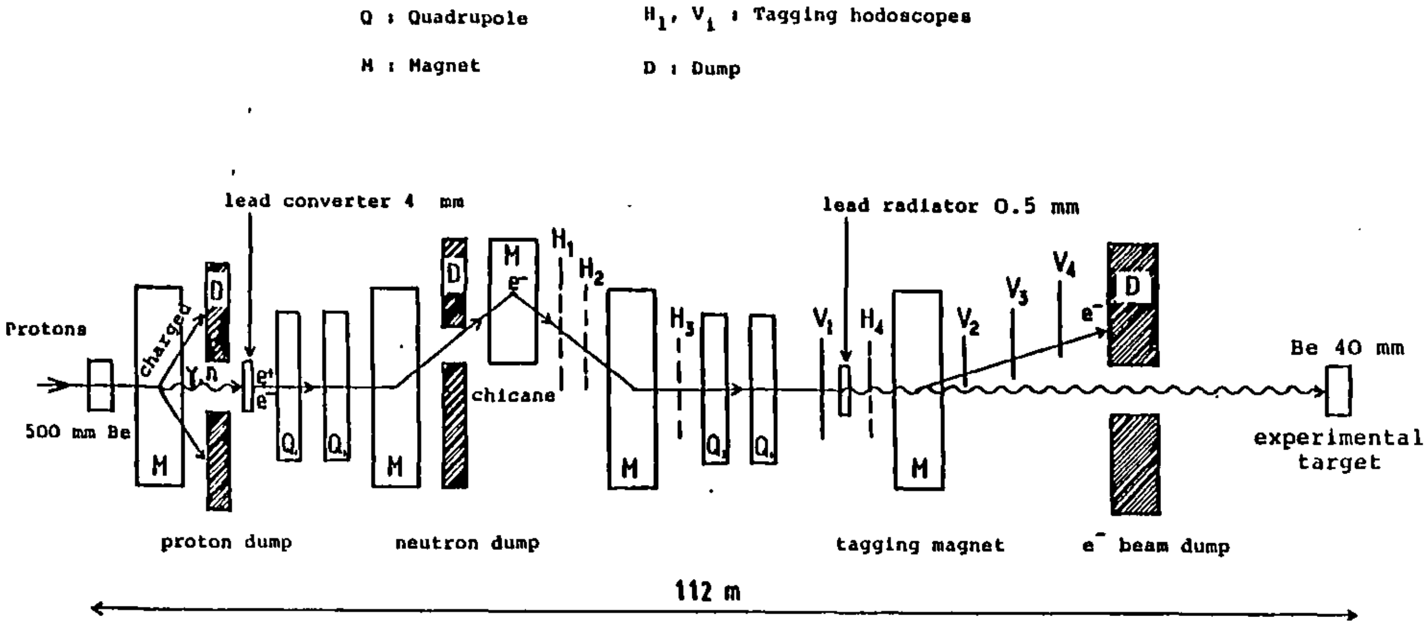
Q : Quadrupole
H_i, V_i : Tagging hodoscopes
M : Magnet
D : Dump
lead converter 4 mm
lead radiator 0.5 mm
Protons
500 mm Be
charged
γ
n
e+
e−
D
M
Q
Q
M
D
M
e−
chicane
H1
H2
M
H3
Q
Q
V1
H4
M
V2
V3
V4
e−
D
Be 40 mm
experimental target
proton dump
neutron dump
tagging magnet
e− beam dump
112 m

Figure 1.4

TABLE 1.1

NA-14 Beam Parameters

Primary proton beam	intensity energy	2.0 10^{12} 400 GeV
Electron Beam	intensity energy range mean energy	10^{8} 120-250 GeV 140 GeV
Tagged Photon Beam Intensity with a 10% radiation length radiator and photon energy > 65 GeV.	 mean energy	5 10^{6} 100 GeV.
Beam size (2σ)	horizontal vertical	± 34 mm ± 22 mm
Hadronic contamination		10^{-5}
Luminosity (10 days + safety factors + 40 mm Be target)		5 10^{35} cm^{-2}

tion of the beam at this stage is mainly due to neutrons, kaons and lambdas.

The next stage in the process is to produce a beam of electrons by inducing the photons to pair produce. This is accomplished by the converter which is a sheet of lead 4 mm thick placed 14 m downstream of the production target. Its thickness and composition is a compromise between the flux and energy spectrum of the produced electrons and the minimization of the probability of a neutral hadron interacting with it to produce a negatively charged particle that would contaminate the electron beam. Increasing its thickness would result in a higher flux of electrons but their mean energy would decrease. About 60% of the photons convert into electron-positron pairs. The mean energy of the electrons is about 140 GeV. Electrons are chosen, rather than positrons, to reduce the muon contamination of the beam. Since the incident protons are positively charged, the flux of μ^+ is about a factor of two larger than the flux of μ^-.

The electron beam is purified and its momentum range selected by deflecting it through a chicane with the help of five magnets; M_1 to M_5. The two quadrapole doublets Q_1, Q_2 and Q_3, Q_4 serve to focus the electron beam. Positively charged and neutral particles are dumped in an iron wall 4 m thick. The positive particles are mainly positrons, pions and protons. The pions and protons are the result of the decays $K^0_S \rightarrow \pi^+\pi^-$, $\Lambda^0 \rightarrow \pi^-p$, $\bar{\Lambda}^0 \rightarrow \pi^+\bar{p}$.

The final stage is the production of the bremsstrahlung photon beam. The electron beam interacts with the radiator which is a sheet of lead 0.5 mm thick. This thickness is chosen to maximize the probability of the production of a single high energy photon per electron. An increase in the thickness of the radiator would result in a higher photon flux but would also increase the probability of multiple bremsstrahlung. This would degrade the energy resolution of the tagging system. About 10% of the electrons radiate to produce a single high energy bremsstrahlung photon. The energy spectrum of the produced photons, measured during a test run in November 1981, is shown in Figure 1.5

The photon beam is tagged by measuring the electron energy before and after the bremsstrahlung. This is accomplished by measuring the electron trajectory with scintillator hodoscope

Figure 1.5

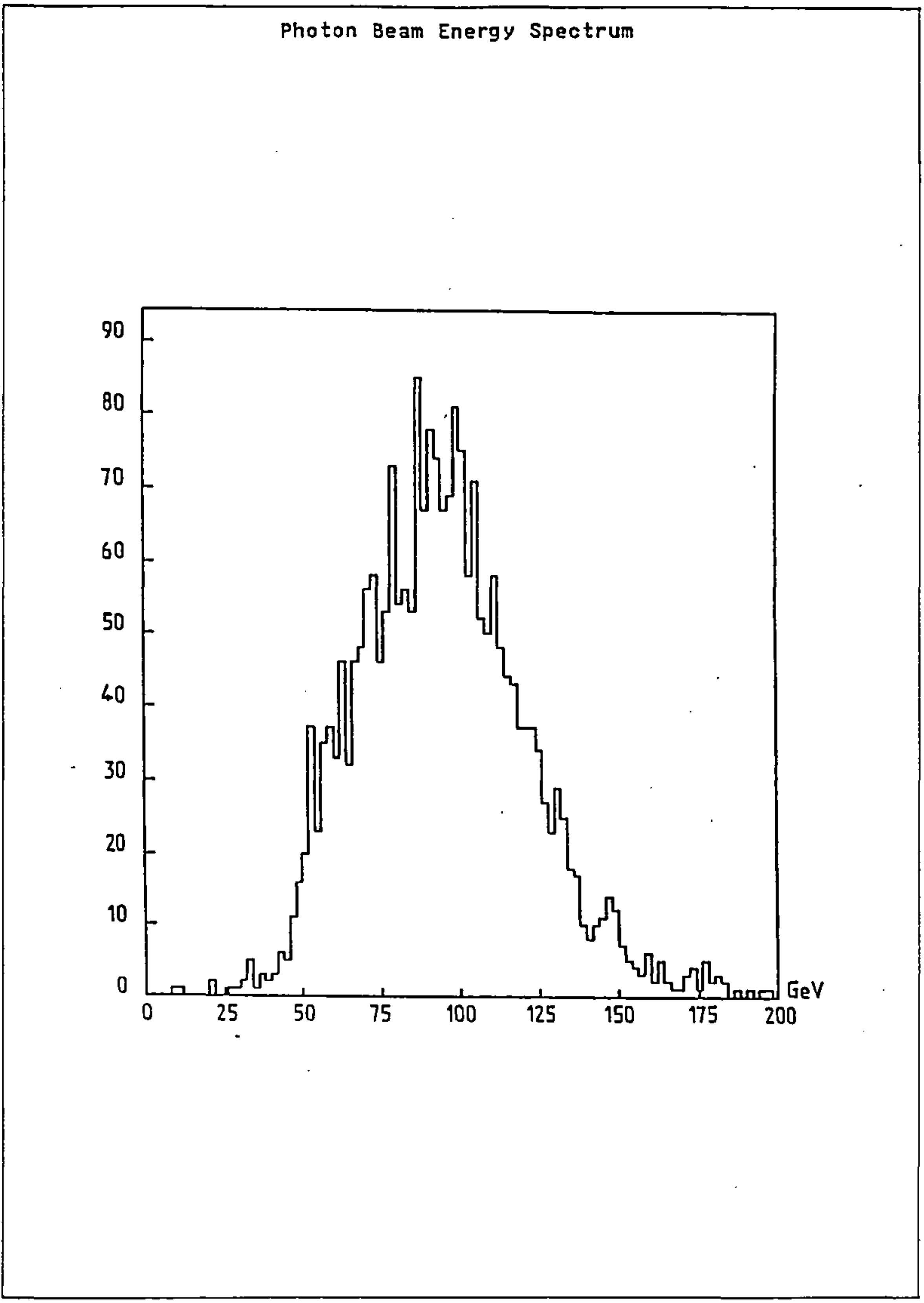
Photon Beam Energy Spectrum
90
80
70
60
50
40
30
20
10
0
0
25
50
75
100
125
150
175
200
GeV

arrays equipped with very fast photomultipliers. The hodoscope arrays H_1-H_4 measure the electron momentum before bremsstrahlung from its deflection in the field of M_4 and M_5. The vertical deflection in the field of the tagging magnets is measured by the hodoscope arrays V_1-V_4.

A fast hardware processor being developed at CERN will use the information from these hodoscopes to provide an online calculation of the photon momentum. It will generate a trigger signal if the momentum exceeds a certain threshold. By demanding a coincidence between this signal and the trigger from the calorimeters it will be possible to impose an online cut on the momentum of the incident photon.

Chapter II

CALORIMETRY

In the context of High Energy Physics, a Calorimeter is a total absorption detector used to provide a measure of the energy of a particle. Depending on its construction, it may also provide spatial information and some degree of particle identification.

Conceptually, it consists of a block of matter with which the primary particle interacts and deposits its energy in a shower or cascade of increasingly lower energy particles. Most of the energy deposited eventually appears in the form of heat. A small fraction of it, proportional to the total energy of the particle, can appear as scintillation light, Cerenkov light or ionization charge. It is this energy that can be measured to provide an estimate of the energy of the primary particle. The uncertainty in the measurement is governed by statistical fluctuations in the development of the cascade and the resolution σ/E improves as $1/\sqrt{E}$ with increasing incident particle energy E.

Apart from statistical fluctuations, the nature and development of the shower is significantly different for Electromagnetic and Hadronic primary particles. It is worthwhile considering each of them in some detail since these differences will be exploited to distinguish between the two.

2.1 Electromagnetic Showers

For electromagnetic particles, such as the photon or the electron, the cascade develops primarily through the processes of bremsstrahlung and pair production. Since the cross-section for these processes is essentially energy independent above 1 GeV/c, the longitudinal development is determined by the composition of the material traversed. This is parametrized by the radiation length X_0. An electron that traverses one radiation length of a material experiences an energy loss of a factor of e ($\simeq 2.718$) on average. For a material of atomic number Z and mass number A, an approximation to X_0, correct to within 20% for $13 \lesssim Z \lesssim 92$, is

$$X_0 = 180A/Z^2 \text{ g/cm}^2$$

In terms of the radiation length, the absorption length or mean-free-path for photons, determined by pair production, is given by

$$\lambda = 9X_0/7$$

For electrons of energy E, the equivalent of the absorption length, defined as the mean-free-path before losing the minimum detectable energy k_m by radiation is

$$\lambda_e = X_0/\ln(E/k_m)$$

This definition is inappropriate at low energies since the energy loss through ionization becomes significant.

An electron or photon entering a material will, on average, interact with an atom after one mean-free-path, to produce more electrons or photons. This multiplication process is repeated several times until the average energy of the secondaries is below the critical energy ϵ after which no further multiplication takes place. The critical energy ϵ is the energy at which the rate of energy loss by radiation is equal to the rate of energy loss by collision. An approximation to ϵ valid to within 10% for $13 \lesssim Z \lesssim 92$ is

$$\epsilon \simeq 550/Z \text{ MeV}.$$

The shower then dissipates slowly, ionization loss and Compton scattering being the dominant processes for electrons and photons respectively. Hadronic interactions, their cross-sections being so much smaller, play no significant part in the energy deposition.

Although the basic sub-processes involved are fairly well understood, the process of shower development is so complicated that no complete analytic description exists. In order to obtain accurate information on the development of electromagnetic showers, one has to actually do an experiment or resort to Monte-Carlo simulations. Several sophisticated Monte-Carlo programs exist; the most widely used is probably EGS (Electron-Gamma-Shower) [FOR]. Typically, these programs track individual shower particles through the detector geometry until their energy is below a certain threshold. All possible interaction processes are statistically sampled for each particle. These programs give results that are in fair agreement with experimental results, however, they are expensive in computer time, especially for large values of incident energy and low values of the threshold energy.

Another way to do the simulation is to assume some parametrization of the shower differential energy deposit and to simulate fluctuations by:

1. Randomly varying the position of the first significant interaction.
2. Smearing the energy of the incident particle to simulate the energy resolution of the calorimeter.
3. Randomly varying the length of the shower by scaling some of the parameters.

This method is of no use in an attempt to predict the energy resolution of a calorimeter, but it is useful in the study of position resolution and pattern recognition problems, and is not so demanding on computer resources as a full Monte-Carlo simulation.

2.1.1 Analytic Calculations

The most useful simple analytic calculations are based on ROSSI'S APPROXIMATION B [ROS]. In this model the following assumptions are made:

1. The energy dependence of all cross-sections is neglected and their asymptotic values are used.
2. The problem is reduced to one dimension, multiple Coulomb scattering and the finite production angles of the particles is ignored.
3. A constant energy loss of ϵ per X_0 is assumed for all secondary electrons.
4. Compton scattering is neglected and explicit solutions are only obtained in the limit $E_c = 0$. The cutoff energy E_c is the minimum kinetic energy of an electron that can be detected in the calorimeter.

The results obtained using this approximation are in fair agreement with experiment. As is to be expected, the predictions tend to be valid for light materials only. Low energy processes are ignored and so this model does not correctly describe the low energy component of the shower. The results are identical for all substances provided that distances and energies are measured in units of X_0 and ϵ respectively.

The quantity used to describe the spatial development of the shower is the differential distribution of T, the track length. T is defined to be the sum of the length of all the charged particle tracks in the shower. It depends on the cutoff energy E_c, for $E_c = 0$ all electrons are detected and the total track length in units of X_0 is given by E/ϵ where E is the energy of the incident particle. For increasing values of the cutoff energy, the useful track length decreases. Using Rossi's Approximation B, it is possible to calculate the fraction of the total track length seen on average as a function of E_c and ϵ [ROS]. It is given by

$$F(z) = ze^{z} \int_{z}^{z_e} e^{-s}/s^{2}\, ds$$

where $z = 2.29\, E_c/\epsilon$ and $z_e = E/\epsilon$; E being the energy of the primary particle. If $E \gg E_c$, then after integrating by parts, the above equation can be re-written as

$$F(z) = 1 + ze^{z}\, Ei(-z)$$

where Ei(-z) is the Exponential Integral, defined as

$$Ei(-z) = -\int_{z}^{\infty} e^{-s}/s\, ds$$

An approximation to F(z), valid for $z < 0.3$ and $E \gg E_c$ is

$$F(z) \simeq e^z[1 + z\ln(z/1.526)]$$

which is correct to within 10% in the specified range. Figure 2.1 shows how the available track length changes as a function of E_c/ϵ.

It has been shown [AMA] that the data for different materials can be put on an almost universal curve if the variable z is redefined as

$$z = 4.58\ ZE_c/A\epsilon$$

So the total track length can be written as

$$T = F(z)EX_0/\epsilon$$

Thus calorimetry is possible because for any given value of E_c, the total track length is proportional to E. Table 2.1 summarises the general features of electromagnetic showers.

2.1.2 Longitudinal Development

The longitudinal development of electromagnetic showers scales in units of the radiation length. Figure 2.2 shows the energy deposit as a function of depth for various materials. The energy deposition is well parametrized [LON] by

$$\frac{dE}{dt} = E_0\frac{b^{a+1}\ t^a\ e^{-bt}}{\Gamma(a+1)}$$

where E_0 is the incident particle energy, t is the depth from the start of the shower measured in units of X_0 and Γ is the Gamma function. The parameters a and b are energy dependent with $b \simeq 0.5$ (at $E_0 \simeq 0.5$ GeV) and a related to it through the position

Figure 2.1[AMA]

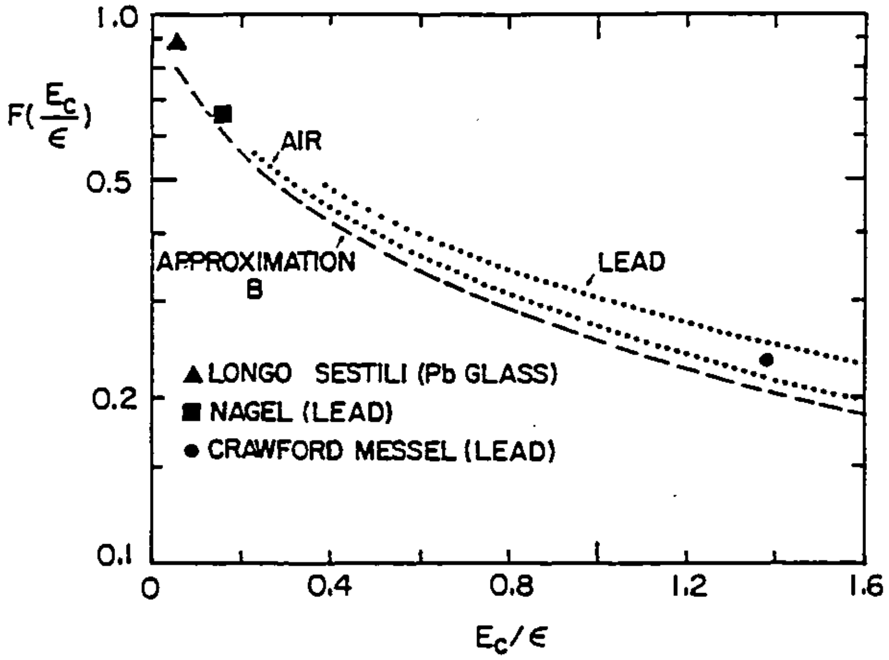

TABLE 2.1

Properties of Electromagnetic Showers

General properties	
Multiplication process	Pair production and Bremsstrahlung
Secondary particles	e^+, e^-, γ. Below the critical energy $\epsilon \simeq 550\mathrm{MeV}/Z$ ionization loss only. Inelasticity $\xi = 1$ (all energy given to particle production)
Absorption length	$9X_0/7$ for γ's $X_0/\ln(E/k_m)$ for e's $X_0 \simeq 180A/Z^2$ g/cm^2 k_m : Minimum detectable energy loss by radiation
Inefficiently detectable energy	Low energy γ's
Largest source of fluctuation	Depth of the first interaction

of the shower maximum $t_{max} = a/b$. The median depth, the depth by which half of the incident energy is deposited, is given by

$$t_{med} \simeq \ln(E_0/\epsilon) + \alpha$$

where $\alpha = 0.4$ for electrons and 1.2 for photons.

The decay of the shower after the maximum can be expressed functionally as $\exp(-t/\lambda_{att})$ where λ_{att} is the longitudinal attenuation length. Experimentally determined values [BAT], [NEL] for λ_{att} are typically of the order of 23 g/cm^2 $\simeq 3.6\ X_0$ for lead. This number is close to the mean-free-path of photons that have a minimum attenuation in a given material. Thus the tail of the

Figure 2.2[FAB]

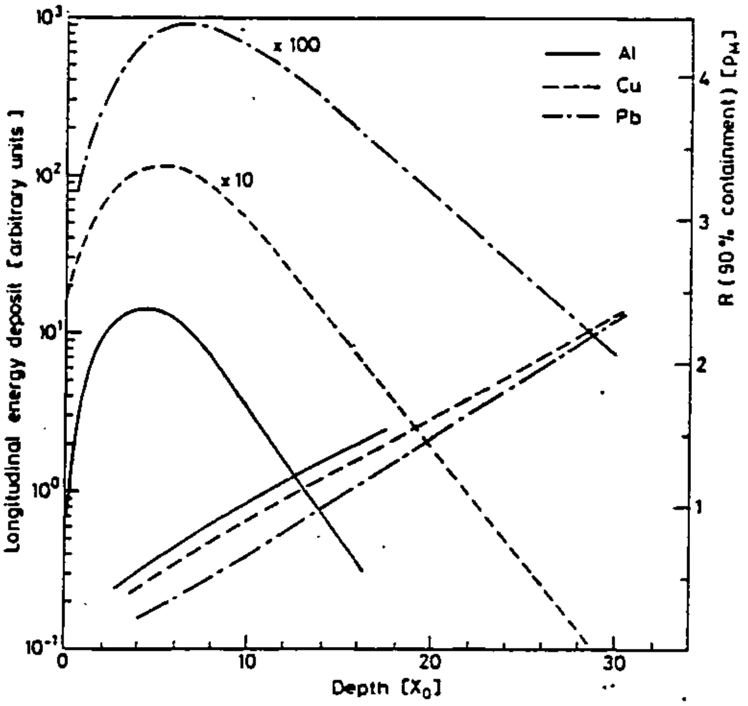

shower consists of an equilibrium particle spectrum of mainly minimum attenuation photons and their interaction products. If this is the case one would expect the dependance of λ_{att} on the primary energy to be negligible and this is borne out by experimental observations [BAT], [NEL] up to energies of 6 GeV/c. It is however material dependant. Table 2.2 summarises the principal features of the longitudinal and lateral development of electromagnetic showers.

2.1.3 Lateral Development

The lateral spread of an electromagnetic shower is mainly due to multiple Coulomb scattering of electrons that do not radiate but have enough energy to travel far from the shower axis. The angular spread caused by bremsstrahlung and pair production being much smaller. The lateral distribution scales in units of the Moliere radius R_m which is the mean lateral spread of an electron beam of energy ϵ after traversing one X_0.

$$R_m = E_s X_0 / \epsilon$$

where E_s = 21 MeV, the constant* of multiple scattering theory [ROS]. R_m may be approximated by

$$R_m \simeq 7A/Z \text{ g/cm}^2$$

---

* The mean square angular deflection of a relativistic particle of energy E after traversing a thickness x of material is

$$\langle \theta^2 \rangle \simeq \frac{x}{X_0} \left[\frac{E_s}{E} \right]^2$$

where

$$E_s = m_e \sqrt{4\pi/\alpha}$$

m_e being the electron mass and α the Fine Structure Constant

TABLE 2.2

Spatial Development Electromagnetic Showers

Average Longitudinal Shower Dimensions	
Energy deposition	Scales in X_0
Rise	Rapid $t_{max} \simeq \ln E[GeV]/\epsilon[MeV]-\alpha$ $\alpha \simeq 1.0$ for e's $\alpha \simeq 0.5$ for γ's
Peak	$\simeq \ln E$ $t_{med} \simeq \ln E/\epsilon + \alpha$ $\alpha \simeq 0.4$ for e's $\alpha \simeq 1.2$ for γ's
Tail	Slow exponential $\lambda_{att} \simeq 3\text{-}4\ X_0$
Length	$\simeq \ln E$
Depth for 95% longitudinal containment	$L \simeq t_{max} + .08Z + 9.6$
Average Lateral Shower Dimensions	
Energy deposition	Scales in R_m $R_m \simeq 7A/Z\ gm/cm^2$
Tail	Fast exponential with a small tail
Radius for 95% radial containment	$R \simeq 2R_m$

which is valid to within 10% for $13 \lesssim Z \lesssim 92$.

The profile consists of a large central component, sharply collimated and a peripheral component decaying slowly. It is well approximated by the superposition of two exponentials with different lateral attenuation lengths,

$$Y(y,t) = C_1\exp[-|y|/\lambda_1(t)] + C_2\exp[-|y|/\lambda_2(t)]$$

where y is the distance from the shower axis and t is the depth from the face of the calorimeter. The long tail is primarily due to the isotropic propagation of minimum attenuation photons. The attenuation length λ_1 for the central component increases with longitudinal depth, Figure 2.3, and is much larger when a lighter material is inserted in the shower (the transition effect see 2.1.4). The asymptotic value of the average angle of the shower electrons relative to the shower axis, well beyond the shower maximum is given by $\langle 1/\cos\theta \rangle \simeq 1.5$ [YUD], [NAG]. For the non-central component, the attenuation length is experimentally determined to be $\lambda_2 \simeq \lambda_{att}/\sqrt{3}$ [YUD] where λ_{att} is the longitudinal attenuation length. It is this fact that suggests that as for the case of the longitudinal development, the tail is due to the isotropic propagation of minimum attenuation photons. In contrast to λ_1, λ_2 does not depend much on the depth of the shower, however, its relative significance changes.

If the lateral depth is measured in units of Moliere radii, the dominance of scattering effects leads to the profile for the central component being material independent. The peripheral part, however, violates this scaling since the coefficient for minimum attenuation photons has no simple unit of scale independent of the choice of material. Figure 2.4 shows the integrated lateral profile. The radius needed for 95% containment of the lateral component of the shower is approximately

$$2R_m \simeq 42X_0/\epsilon \simeq 14A/Z \text{ g/cm}^2$$

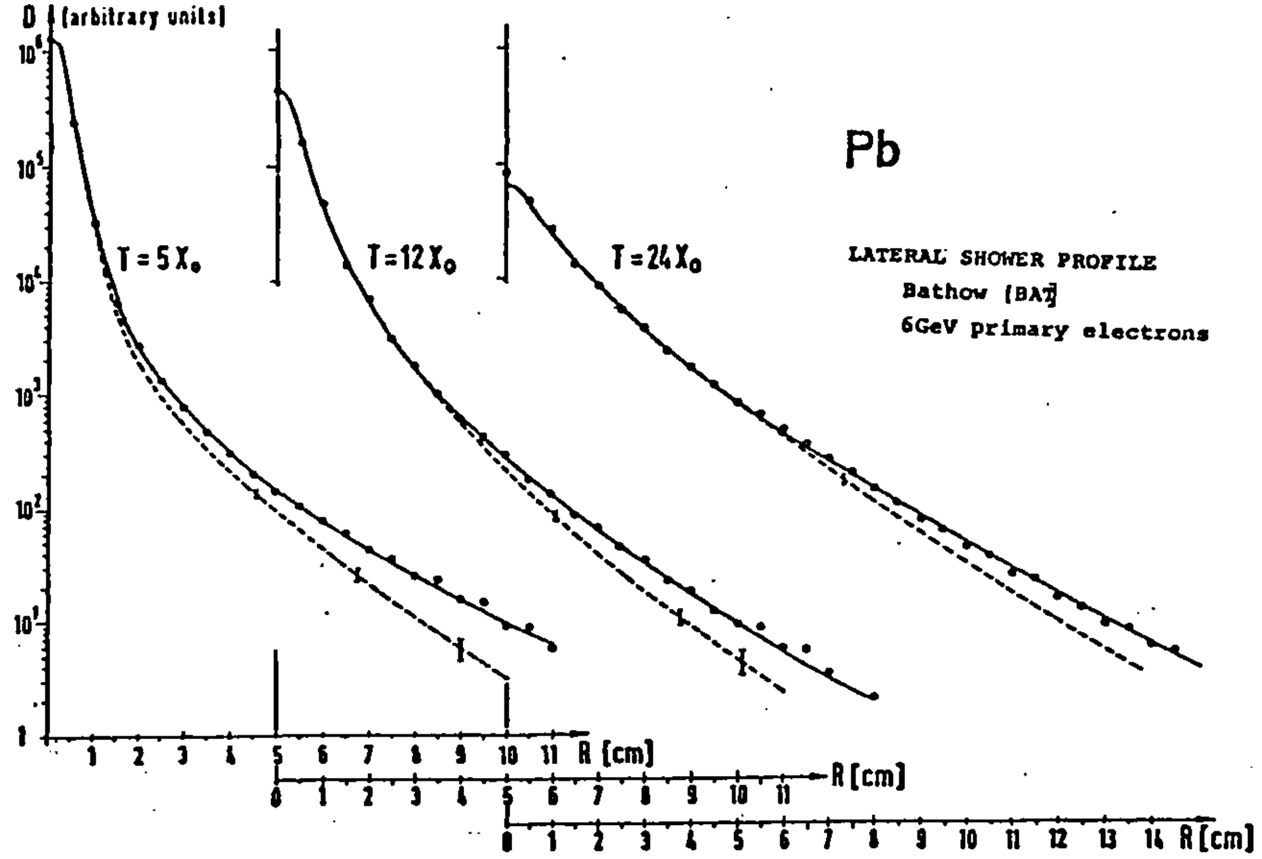

Measured lateral shower distribution for lead (circles) in comparison with Monte-Carlo results (dotted line with error bars)

Figure 2.3

Figure 2.4

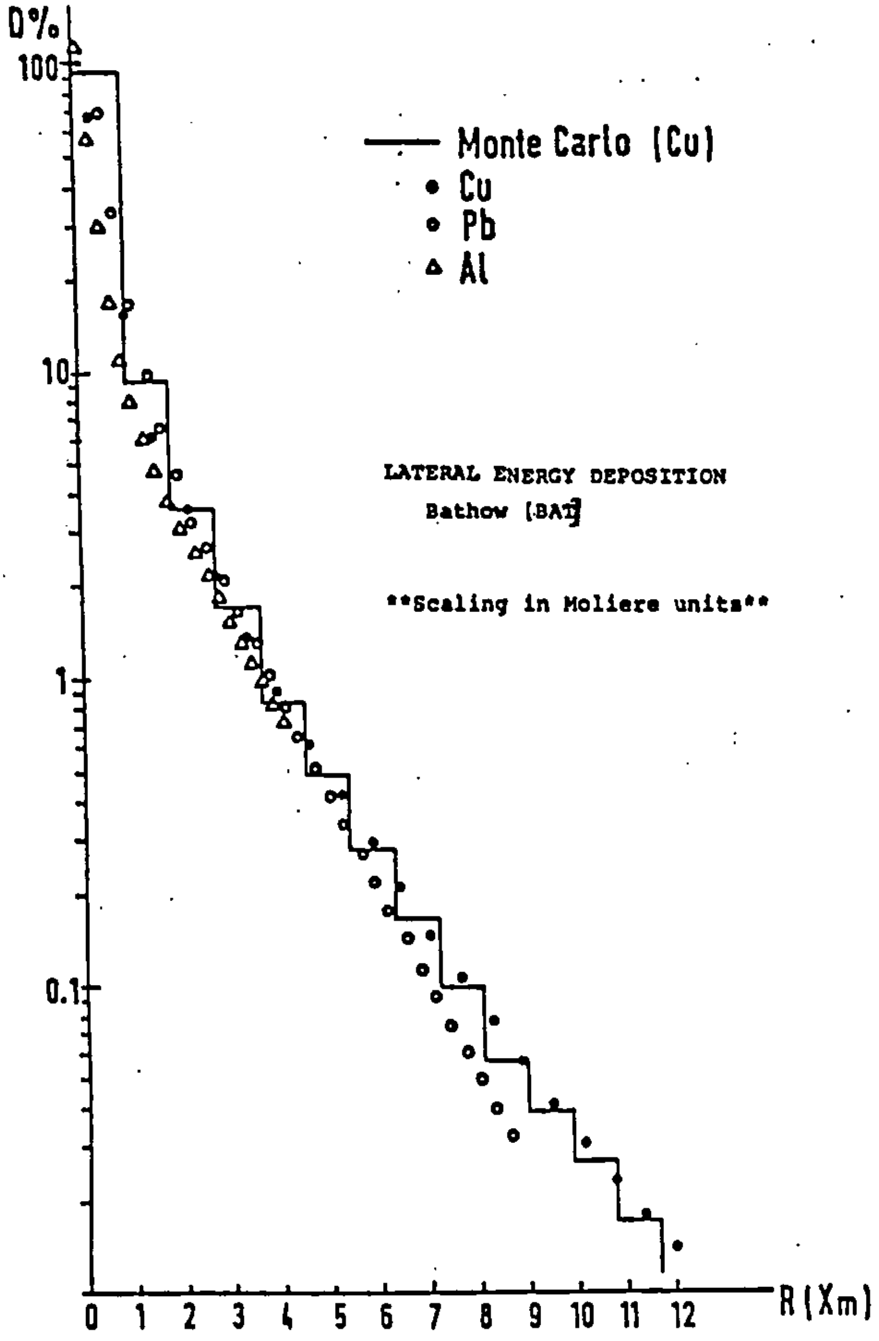

Energy deposition integrated over depth for Pb, Cu and Al. For comparison, a histogram of Monte-Carlo results for copper is shown.

2.1.4 Transition Effects

The flux and energy spectrum of electrons or photons traversing the boundary between two materials having different critical energies undergoes a transition. The reason for this is the difference in the electron ionization loss rate and atomic interaction cross-sections in the two materials. Since the multiple scattering rate is also different, the energy spectrum is distorted by the change in effective path length and backscattering rate. This local readjustment of the shower spectrum after such a boundary is called the Transition Effect and significantly influences the low energy component of a shower.

Since a boundary is required, it is only of importance in Sampling Calorimeters where it influences the absolute value of the observed deposited energy. Provided the calorimeter is calibrated directly with electrons or photons, the transition effect is only of academic interest. Its effect is apparent when the calorimeter is calibrated using particles of known momentum such as muons moving perpendicularly through its active and passive layers of thickness x_a and x_p [AMA]. If P_a is the pulse height measured in one of the active layers, the "number of equivalent particles" of a completely contained shower that produces a pulse height P_{sh} is given by $n_{eq} = P_{sh}/P_a$ and the visible energy -

$$E_{vis} = n_{eq}[x_a(\Delta E/\Delta x_a) + x_p(\Delta E/\Delta x_p)]$$

where the average rates of energy loss have to be computed using the momentum of the particles used for the calibration. The experimentally observed value for E_{vis}/E where E is the energy of the incident electron is always less than unity. This discrepancy is usually attributed to the transition effect on encountering the light active material (usually plastic scintillator). The electron collision losses increase by a factor of

$$\epsilon_a/\epsilon_p = Z_p/Z_a$$

while the materialization rate per radiation length for photons remains the same. This disturbs the γ/e equilibrium resulting in a decrease of the electron flux.

The magnitude of the effect can be computed using Approximation B [PIN] and has also been measured experimentally [YUD], [CRA]. A 0.9 cm thick layer of acrylic scintillator placed after a sheet of lead reduces the electron flux by about 20%. In a sandwich counter composed of alternate layers of dense and light material, the next absorber contributes to the energy sampled by the active layer in front by a backscattered component. This can recover the electron flux reduction by up to 10% [CRA].

Before the shower maximum, the shower contains a few particles each carrying a large fraction of the primary energy, so the magnitude of the transition effect is small. Just after the shower maximum however, the majority of shower particles have energies less than the critical energy ϵ_a and it is at this stage of the shower that the magnitude of the transition effect is at a maximum.

2.1.5 Energy Resolution

The intrinsic energy resolution* of a calorimeter of infinite dimensions is limited only by the statistics of the elementary processes involved and has been computed to be [LON]

$$\frac{\sigma(E)}{E} = \frac{\sigma(T)}{T} \simeq \frac{0.7\%}{\sqrt{E[\mathrm{GeV}]}}$$

for $E_c/\epsilon = 0.5/11.8 = 0.04$. In practice, there are several effects that contribute to a degradation in the obtainable energy resolution. Table 2.3 summarises the principal factors limiting energy resolution. I shall describe only those that are relevant to sampling calorimeters.

Containment

If the shower is not fully contained in the calorimeter, the energy measurement is incorrect and its distribution for monochromatic electrons acquires a tail extending towards zero. The effect on the resolution is small if the leakage is not too large, and $\sigma(E)/E$ is proportional to $\log(E)$ [FAB]. Longitudinal losses are much more serious than lateral ones. A 5% lateral loss has a much smaller effect on the resolution than a 2% longitudinal loss [FAB].

---

* The symbol σ is used to represent the R.M.S resolution. Where the resolution is measured by the Full Width at Half Maximum, the expression $\sigma(\mathrm{FWHM})$ is used.

TABLE 2.3

Factors Limiting Energy Resolution for EM showers

Contributing mechanism (add in quadrature)	Magnitude of the effect
Intrinsic fluctuations	Track length fluctuations $\sigma/E \simeq 0.007/\sqrt{E}[\mathrm{GeV}]$
Sampling fluctuations*	$\sigma/E \simeq 0.04\sqrt{\Delta E/E}$
Instrumental effects	Noise and Pedestal width $\sigma/E \simeq 1/E$ -determines minimum detectable signal -limits low energy performance Calibration errors and Non uniformities $\sigma/E \simeq$ constant -limits high energy performance Photoelectron statistics
Incomplete containment of the shower	$\sigma/E \simeq \log E$ For leakage $\gtrsim$ few % Non-linear response and Non-gaussian tail

* ΔE = Energy lost by a single charged particle in one sampling layer measured in MeV, E = Total energy GeV.

Fluctuations in the number of crossings

In Approximation B, the shower has no lateral spread and if $E_c = 0$, the total track length is given by

$$T = EX_0/\epsilon$$

Thus in an infinitely long medium, a set of layers of thickness x intercepts a number of tracks given by T/x independent of the longitudinal distribution of the shower. So the number of crossings

$$N = EX_0/\epsilon x = E/\delta E$$

where δE is the energy lost by a minimum ionizing particle traversing one of the layers of thickness x. If one assumes that the crossings are independent and follow a normal distribution, the r.m.s error in the energy measurement due only to sampling fluctuations is given by [AMA]

$$\frac{\sigma(E)}{E} \simeq \frac{1}{\sqrt{N}} = \frac{\sqrt{\delta E}}{\sqrt{F(z)E}} \simeq 3.2\% \frac{\sqrt{\epsilon t}}{\sqrt{F(z)E}}$$

where the factor F(z) takes into account the shortening of the track length due to a finite value of the cutoff energy E_c and $t = x/X_0$, the thickness of a calorimeter layer expressed in units of radiation length.

This estimate is based on Approximation B and is thus valid only for light materials. In a heavy material, one would expect the transverse dimensions of the shower to be much larger since the Moliere radius scales as

$$R_m/X_0 = E_s/\epsilon.$$

Fisher's Monte-Carlo calculation [FIS] shows that a large fraction of the low energy electrons form large angles with respect to the shower axis Figures 2.5, 2.6.

An attempt to qualitatively understand the Z dependance of this effect has been made [AMA]. For a track forming an angle θ with the shower axis, the sensitive layers appear at an effective distance of t/cosθ so that an average correction factor of

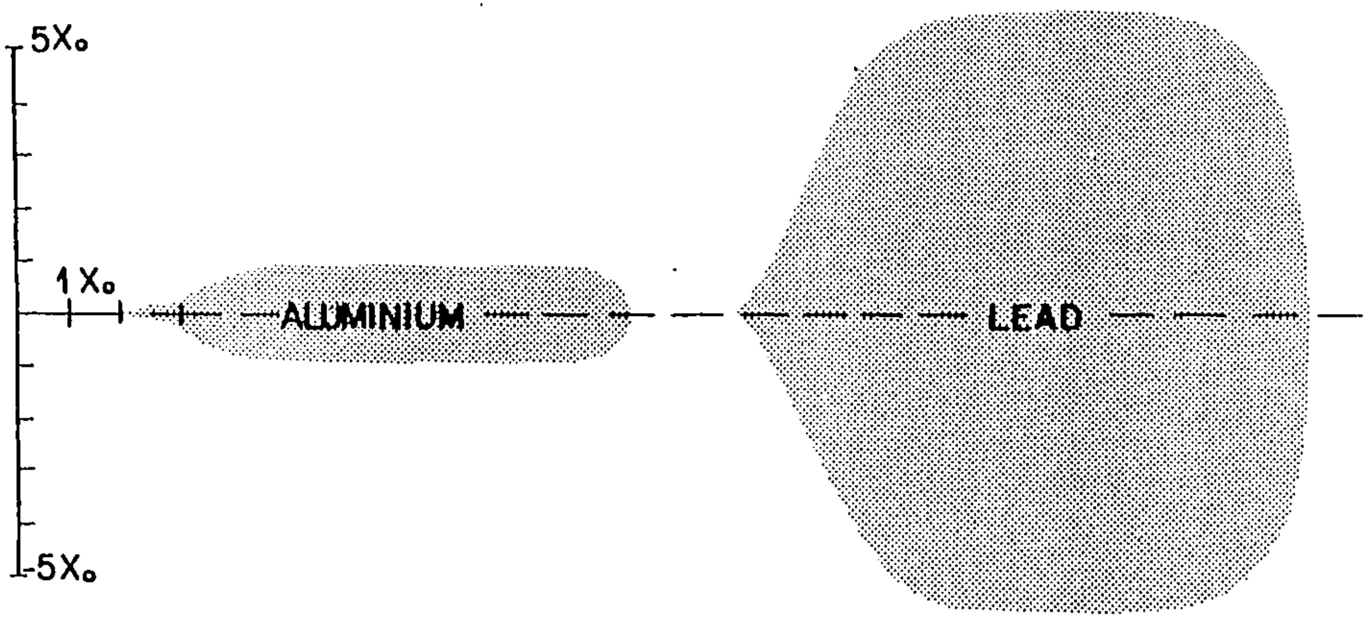

Schematic representation of the cross-section of the volume that contains, on average, about 90% of the total energy of an electromagnetic shower. The units are radiation lengths on both axes.

Figure 2.5[AMA]

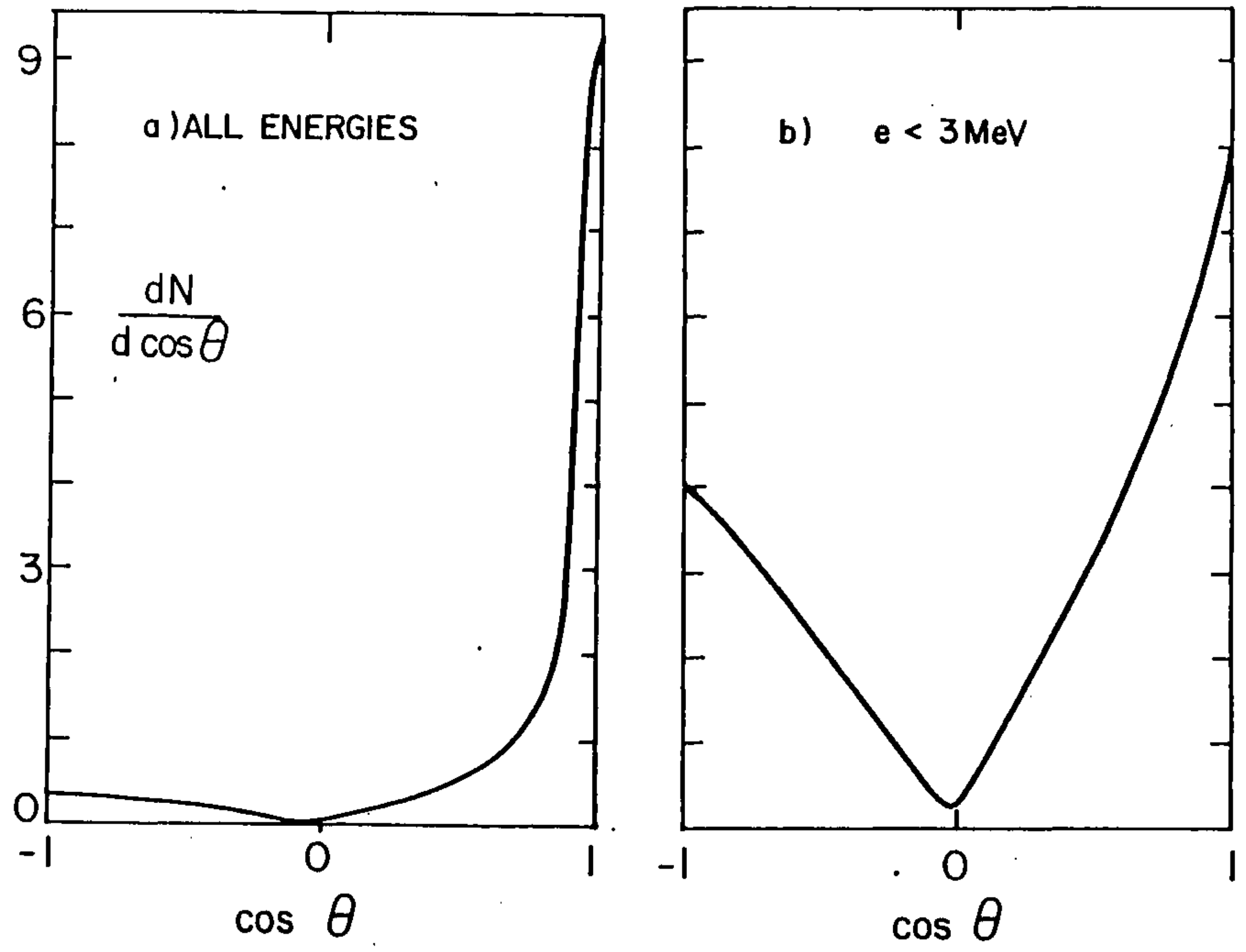

Figure 2.6[AMA]

$1/\sqrt{\langle\cos\theta\rangle}$ has to be applied. Using input from Monte-Carlo they estimate

$$\langle\cos\theta\rangle \simeq \cos(E_s/\pi\epsilon)$$

valid when the cutoff energy $E_c \lesssim 10/\epsilon$ MeV. The sampling resolution then becomes

$$\frac{\sigma(E)}{E} = 3.2\% \, \frac{\sqrt{\epsilon\ [\mathrm{MeV}]}}{\sqrt{F(z)\cos(E_s/\pi\epsilon)}} \quad \frac{\sqrt{t}}{\sqrt{E\ [\mathrm{GeV}]}}$$

Regarding the above equation, the author [AMA] makes the following points :

1. The simple estimate from Approximation B is corrected by taking into account the cutoff energy E_c and the scattering of low energy electrons. The factor $F(z)\langle\cos\theta\rangle$ includes other effects neglected by Approximation B, in particular that the assumption of constant absorption of photons for high Z materials is incorrect even for energies larger than ϵ. There are more electrons and photons than predicted.
2. The fact that $N = EX_0/\epsilon x$ overestimates the number of tracks has long been known. The discrepancy has been attributed to the fact that electrons and positrons are always created in pairs, so that the number of statistically independant crossings is N/2 and not N. This cannot be the case because it would also hold for low Z materials and would cause disagreement with experiment.
3. The effect of the cutoff energy E_c on the two correcting factors $F(z)$ and $\cos(E_s/\pi\epsilon)$. With increasing E_c the first decreases and the second increases because the isotropic

component is less well sampled. Thus one would expect a rough compensation between the two and a large range of validity for the expression.

Landau Fluctuations

These are more serious for sampling calorimeters in which the active material has a low density (eg. gas) and only contribute minor corrections to the fluctuations in solid or liquid detectors.

The distribution of energy e deposited by a minimum ionizing particle traversing a thickness x of material is asymmetric and has an r.m.s value of the form [KAT]

$$\sigma(e)/e \simeq 2/\ln(4W/E_m)$$

where W is the energy above which on average one δ-ray is produced in the thickness x. For relativistic particles of unit charge $W[\text{MeV}] \simeq 0.15\ Zx/A\ \text{g/cm}^2$ and E_m is the minimum energy of a δ-ray, usually taken to be ≃ 30 eV. Because of the tail of the Landau distribution, the contribution to the total energy resolution from N crossings is not exactly proportional to $1/\sqrt{N}$. However, an order of magnitude estimate may be obtained by using the above equation and setting $Z/A \simeq 0.5$

$$\frac{\sigma(E)}{E} \simeq \frac{1}{\sqrt{N}}\ \frac{2}{\ln(10^4 x\ \text{g/cm}^2)}$$

This increases the sampling fluctuations by less than 3% for a detector thickness of 1 g/cm².

Path length fluctuations

A large fluctuation in the path length that the electrons make in the active material of the calorimeter is caused by the wide spread in the angles that electrons make with the shower axis. Again the effect is more serious for a gas because

1. The cutoff energy is much smaller so that electrons of low energy moving along a sensitive layer deposit much more energy than electrons moving normal to the plane.
2. The multiple scattering in a dense layer is much larger than in a gas so that the electrons tend to be scattered out of the dense layer thus causing a corresponding reduction in path length fluctuations [AMA].

2.2 Hadronic Showers

Hadronic cascades are of a much more complex nature than Electromagnetic cascades and no simple analytic treatment similar to Approximation B exists to describe them. A variety of different particles are produced in energy dependant ways by different interaction and decay mechanisms. In addition, interactions with nuclei play an important role in the energy deposition. The basic processes involved are again fairly well understood and several Monte-Carlo programs have been developed to simulate hadronic showers. Table 2.4 summarises the principle features of hadron induced showers.

Hadronic interactions are characterised by their multiparticle production with limited transverse momentum $\langle P_t \rangle \simeq 0.35$ GeV/c in

TABLE 2.4

Properties of Hadronic Showers

General properties	
Multiplication process	Nuclear multiparticle production
Secondary particles	Fast nucleons, pions; medium energy (100 MeV) p's, n's;low energy (10 MeV) p, n, γ;nuclear fragments inelasticity $\simeq 0.5$
Inefficiently detectable energy	Low energy n's, γ's, decay μ, ν, nuclear fragments
Largest source of fluctuation	Energy given to π^0's in the first interaction; Depth of the first interaction
Average Shower Dimensions	
Long. energy deposition	Scales in λ_0
Rise	Rapid $t_{max}[\lambda] \simeq 0.6\ln[E] - 0.2$
Peak	$\simeq \ln E$
Tail	Slow exponential $\lambda_{att} \simeq 1\text{-}2\ \lambda_0$
Depth for 95% longitudinal containment	$L[\lambda] \simeq t_{max} + 4E^{0.15}[\text{GeV}]$
Lateral energy deposition Tail	Scales in g/cm^2 (?) Fast exponential with long tail
Radius for 95% radial containment	$R \simeq \lambda_0$

which about half of the incident energy is consumed. The remainder is carried by a fast forward going particle or cluster of particles having the same quantum numbers as the incident particle : the leading particle effect. The secondaries are mainly pions and nucleons with a multiplicity composition only weakly energy dependant above the resonance region ($E \gtrsim 1$ GeV). The average multiplicity per inelastic interaction increases slowly with the available energy ($\simeq \ln[s]$) but with a large energy independant dispersion ($\simeq$ 50% on average).

Except for a multiplication factor parametrized in powers of the mass number A, the interactions with nuclei are similar to those with isolated nucleons, since quasi-free collisions on bound nuclei dominate at high energies. The inelastic cross-sections are known to vary approximately as $A^{0.67}$ and $A^{0.75}$ for primary nucleons and mesons respectively [IWA]. The average particle multiplicity also increases as $\ln[s]$ and depends weakly on the target material. The average nuclear thickness is defined as

$$\langle \nu \rangle = A \frac{\sigma_i(N)}{\sigma_i(A)}$$

which can be interpreted as the average number of absorption mean-free-paths encountered by the incident particle in going through a nucleus. Experimentally, the overall multiplication of particles in a nucleus, relative to that on a nucleon, increases in proportion to $\langle \nu \rangle$. This slow increase of the multiplicity with nucleon size is primarily in the target fragmentation region, while the number of secondaries from beam fragmentation does not change with A [IWA].

Another source of particle emission, apart from fast particles, is the nuclear disintegration of an excited nucleus. The energy spectrum of each of the emitted particles is determined by the nuclear temperature. It is also possible that groups of nucleons are emitted, but their abundance rapidly decreases with their mass number. The most abundant are neutrons which are not effected by the Coulomb barrier. A substantial amount of energy is used to overcome nuclear binding ($\simeq$ 8 MeV per nucleon). This represents a loss of energy in the sense that the total kinetic energy of the emitted particles is less than the incident excitation energy.

The multiplication process for hadrons is parametrized by the nuclear absorption length

$$\lambda_0 = \frac{A}{N_{av}\,\rho\,\sigma_i}$$

where N_{av} is Avogadros number and σ_i the inelastic cross-section, for a material with mass number A and density ρ. The rate at which a nuclear interaction takes place at a depth t is given by

$$dn = \exp(-t/\lambda_0)/\lambda_0 \; dt$$

The nuclear absorption length is fairly constant at energies well above the resonance region and is almost the same for both the primary and secondary particles.

The first significant interaction occurs on average after one λ_0 before which a charged hadron only loses energy through ionization. In the first interaction, about half the incident energy is consumed in the production of a leading particle, about half in the production of pions and a small fraction by nuclear excitation and the recoil nucleus. Fast charged secondaries go on repeating similar interactions on different nuclei as long as their energy is high enough. Apart from neutrons, which travel long distances in various directions, nuclear fragments lose all their kinetic energy near the interaction point. About one third of the produced pions are neutral and decay almost instantaneously into two photons resulting in electromagnetic showers that die out in relatively short distances. There is a small probability for charged pions to decay into muons and neutrinos. The muons lose their energy only through ionization, while the neutrinos pass through the calorimeter without any interaction. Thus, in a marked contrast with electromagnetic showers, the hadronic shower builds up and decays in somewhat violent steps by a succession of inelastic interactions each with a considerable fluctuation.

2.3 Position Measurements in Electromagnetic Calorimeters

If the calorimeter is preceded by a track detector such as a chamber, then spatial information on charged tracks is easily obtainable. For neutral particles, the chamber can be placed after an active or passive converter. If the calorimeter is laterally segmented, the coordinates of the incident particle can be deduced from the pulse heights observed in consecutive segments. The accuracy obtainable by this method is limited by the size of the segments and fine segmentation is very expensive. Alternatively, the calorimeter segments can be fairly large and spatial information can be obtained by hodoscope arrays that sample the lateral energy deposit.

The intrinsic resolution of a position measurement is very high and the limitations are of a practical nature having to do with the longitudinal granularity and transverse size of the calorimeter segments. Position resolution obtained by recording the shower profile is subject to considerable fluctuations in the shower development with respect to the direction of the primary particle.

If the calorimeter has transverse segments of width 2Δ, an estimate of the position of the shower is obtained by measuring the centre of gravity of the lateral energy deposition.

$$x_c = 2\Delta \frac{\Sigma i A_i}{\Sigma A_i}$$

where A_i is the pulse height measured by the i'th segment. If an exponential profile is assumed for the energy distribution relative to the shower axis, the true shower position x_0 is related to the centre of gravity x_c by [BUS]

$$x_0 = b \sinh^{-1}[(x_c/\Delta)\sinh(\delta)]$$

where $|x_0| \leq \Delta$, $\delta = \Delta/b$ and b represents the characteristic shower width, equivalent to the average lateral attenuation length. Typically $b \approx 5.0$ mm for lead. The correction factor is almost identical in the case where the shower profile is represented by the superposition of two exponentials if b is replaced by the weighted sum of the individual average lateral attenuation lengths b_1 and b_2 [AKO].

Thus the accuracy of the centre of gravity measurement depends on δ which is the counter size relative to the shower width. At

Figure 2.7[IWA]

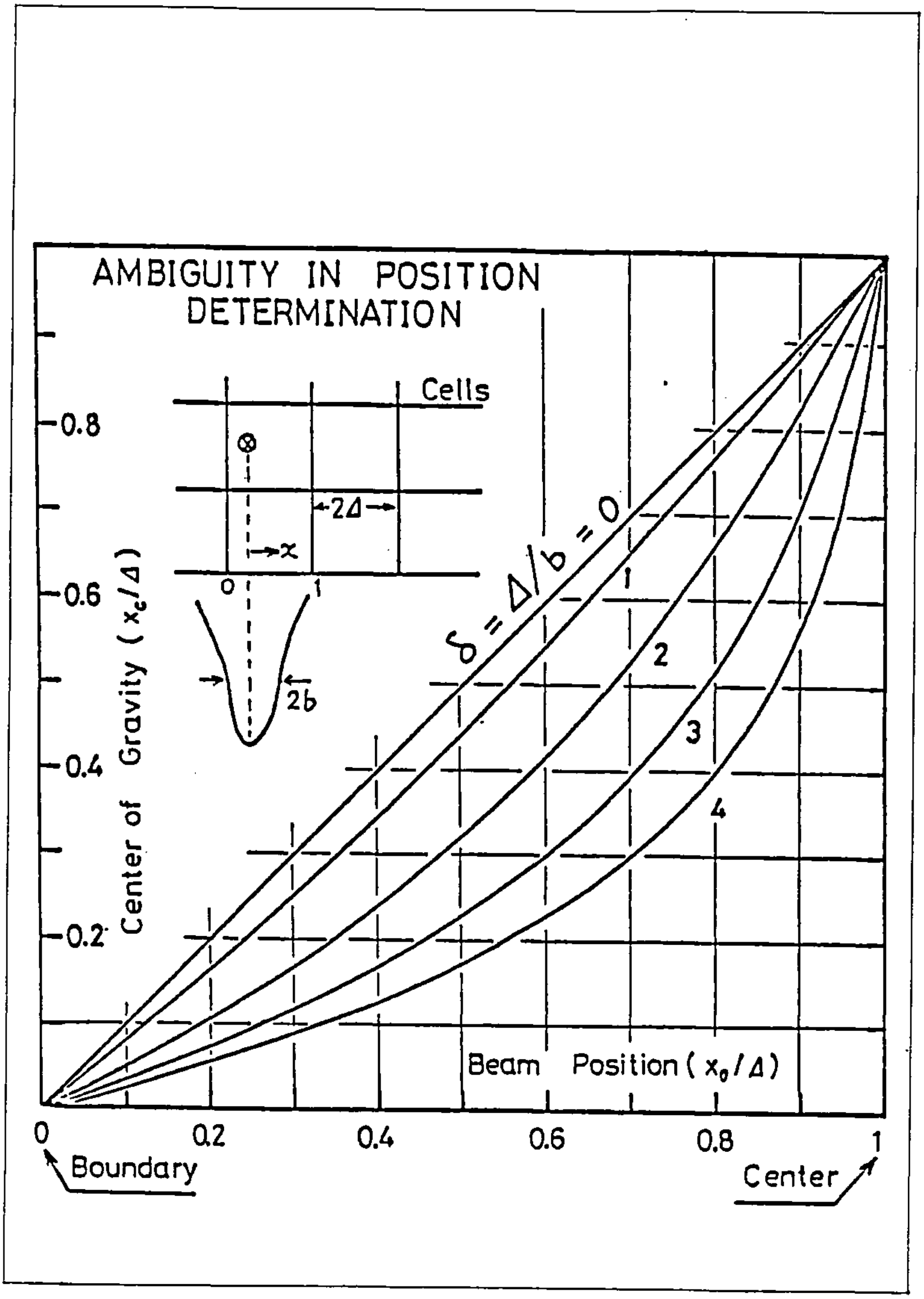

large values of δ, the centre of gravity differs considerably from the true position of the shower. Figure 2.7 shows the relationship between the true shower position and the calculated centre of gravity for different values of δ. The maximum deviation occurs when the shower hits the centre of a half segment [BUS]. For $\delta \lesssim 3$,

$$(x_0 - x_c)_{max} \simeq \frac{\Delta\delta^2}{16}\left[1 - \frac{\delta^2}{20}\right]$$

So the correction factor involved increases rapidly with increasing δ. Good spatial resolution is obtained when $\delta \simeq 1$ ie. when the width of a segment is close to the shower width. The average shower width, represented by b depends on the material and also the depth in the shower where the measurement is made. It increases slowly with increasing depth.

2.4 Particle Identification

For an electromagnetic calorimeter, the principal requirement in particle identification is the ability to distinguish between electromagnetic and hadronic showers. The showers caused by the two types of particles differ in

1. Longitudinal size and profile.
2. Lateral size.
3. Visible fraction of primary energy.
4. Typical velocity of the shower particles.

For particles of known momentum, hadrons can be efficiently rejected by applying a cut on the ratio of the measured energy to the momentum. Typically, rejection factors of about 500 are possible [IWA]. Hadron rejection capability is ultimately limited by the small (few %) fraction of showers where most of the incident energy is consumed in the production of neutral pions. These events will effectively simulate an electromagnetic shower. Some rejection against this can be made [HIT] if the energy deposit in the front part of the calorimeter can be measured (ideally using materials having a large λ_0/X_0 ratio)

A rejection factor of about 2-3 against hadrons can be achieved by examining the lateral shower profile. A passive (or active) converter of a few X_0 followed by scintillator in the front part of the calorimeter can also aid hadron rejection. A factor of about 5-10 in hadron rejection can be achieved by demanding a minimum pulse height in the scintillator equivalent to several minimum ionizing particles. Since the converter accelerates the showering of electrons while having little effect on hadrons, it also helps in the discrimination done by cutting on the fractional visible energy. Unless an active converter is used, however, its thickness is limited since it degrades the energy resolution.

Chapter III

ILSA-THE IMPERIAL COLLEGE LEAD SCINTILLATOR ARRAY

ILSA is a lead-scintillator sandwich sampling calorimeter. It is one of the three calorimeters in the NA-14 experiment used to provide a trigger on high transverse momentum photons.

It is modular in structure, using two different types of modules that differ principally in the amounts of lead and scintillator. Figure 3.1 shows the internal structure of the modules. The A and B modules are identical and are made of alternate layers of lead and scintillator. Each contains 6 plates of Plexipop scintillator of size 1080 x 245 x 5 mm^3. The light from each plate is coupled to the photomultiplier (PM) via a fishtail shaped light guide. The PMs used are RCA type 8575. Close to the PM is a block of scintillator used for PM gain equalization. Each module has embedded in its light guide a Light Emitting Diode (LED) that is used to monitor the PM gain. The whole assembly is enclosed in a light tight sheet iron box. The C and D modules are identical except that they have 9 layers of scintillator.

These modules were previously being used in the WA-11 experiment at CERN. Within the constraints of time and financial resources, they had to be modified and supplemented in whatever way possible to meet the requirements of NA-14. The primary considerations motivating the modifications were

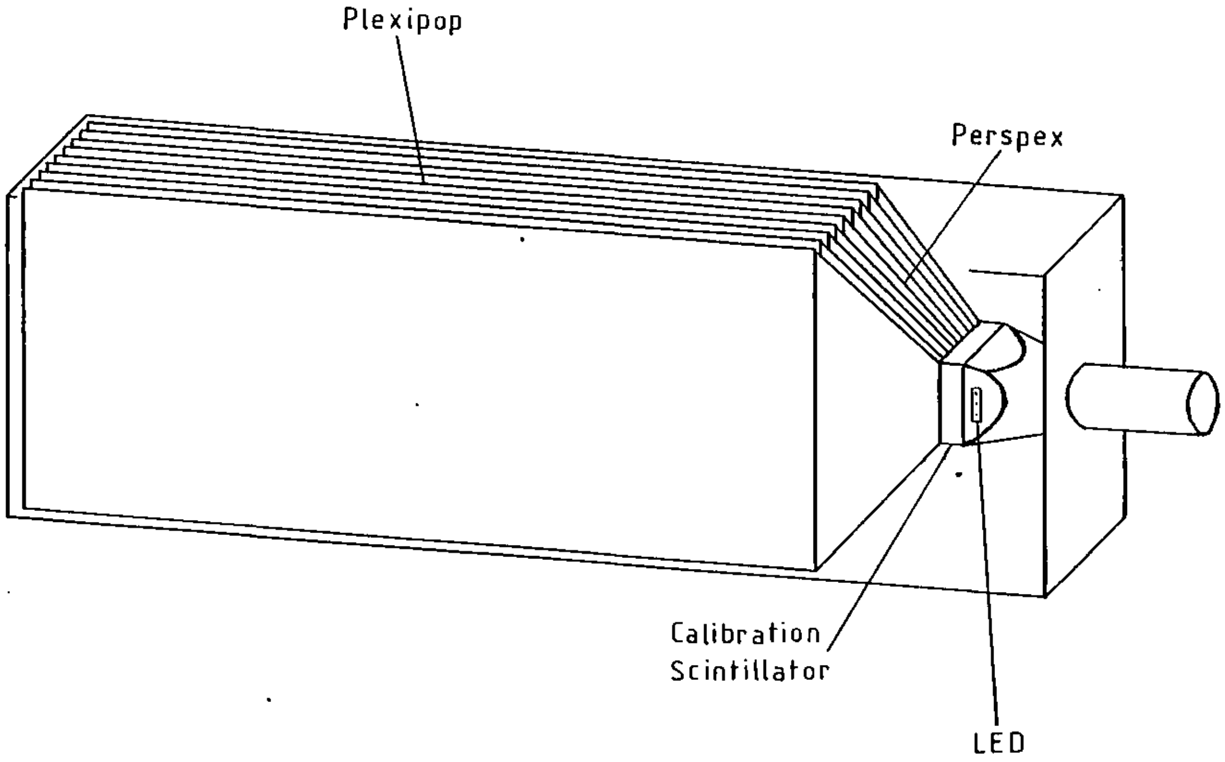

Figure 3.1

1. Improving the energy resolution (previously $\sigma(FWHM)/E \simeq 47\%/\sqrt{E}$) and linearity in detecting photons of energies up to 40 GeV.
2. Providing good spatial resolution to enable the separation of energetic π^0's from single γ's.
3. γ/hadron separation at the trigger level.

In the WA-11 experiment, the calorimeter was made of two layers of modules, one of type A and the other of type C. The A type modules had 7 layers of lead each 3 mm thick and the C type modules had 10 layers of lead each 6 mm thick. Its relatively poor resolution was due to the fact that the main portion of the shower was badly sampled. In order to improve the energy resolution it was decided to double the number of samples by decreasing the thickness of the lead sheets and having two layers of type A followed by two layers of type C. Doubling the number of samples should theoretically improve the energy resolution by a factor of $\sqrt{2}$, provided that showers traverse all of the modules, and that the fraction of energy that leaks out is small.

In order to provide spatial information, a two dimensional scintillator hodoscope array was constructed at Imperial College. This array, called Ariadne, was placed after the first layer of modules to sample the lateral energy deposition of the shower. Figure 3.2 shows the structure of an Ariadne module.

Each finger of Ariadne is a strip of NE110 type scintillator of dimensions 1470 x 15 x 10 mm^3. Light coupling with the PM is via a twisted perspex light-guide 475 mm long. The PMs are Hamamatsu

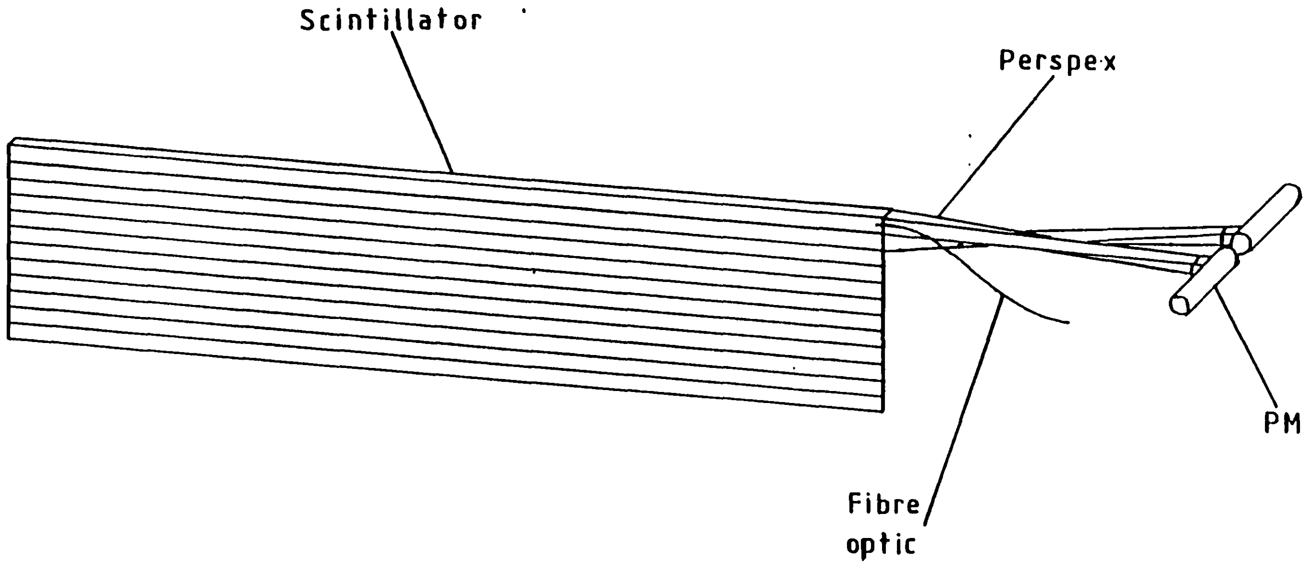

Figure 3.2

type 931B. They are compact 9 stage PMs with a side window. A group of 12 fingers, each individually wrapped in foil and tape, are held together in a box of sheet aluminium 1 mm thick. A fibre optic cable is imbedded in each strip at the junction between the light-guide and the scintillator. This fibre is used to feed light into the strip to enable monitoring of the PM gain.

3.1 The H5 Tests

In order to study the performance of various configurations of the modules, experiments were carried out at the H5 beamline of the CERN SPS. The response of the calorimeter and the position detector was studied for incident electrons and hadrons of momenta 2, 6, 10, 20, 30, 40, 60 and 80 GeV/c.

3.1.1 Experimental Layout

The experimental layout is shown in Figure 3.3. The two threshold Cerenkov counters provide electron/hadron separation. They are followed by several beam definition counters that localize the beam to a cross-section of about 1 x 1 mm^2. Finally, four calorimeter modules and two modules of the position detector mounted on a movable trolley.

The signals from all the PMs were fed into Lecroy 2249 10 bit charge integrating analog to digital converters (ADCs). The amount of lead in the calorimeter modules was varied to investigate its effect on energy resolution and linearity. For most of this discussion I will refer to results obtained using the finally

Figure 3.3

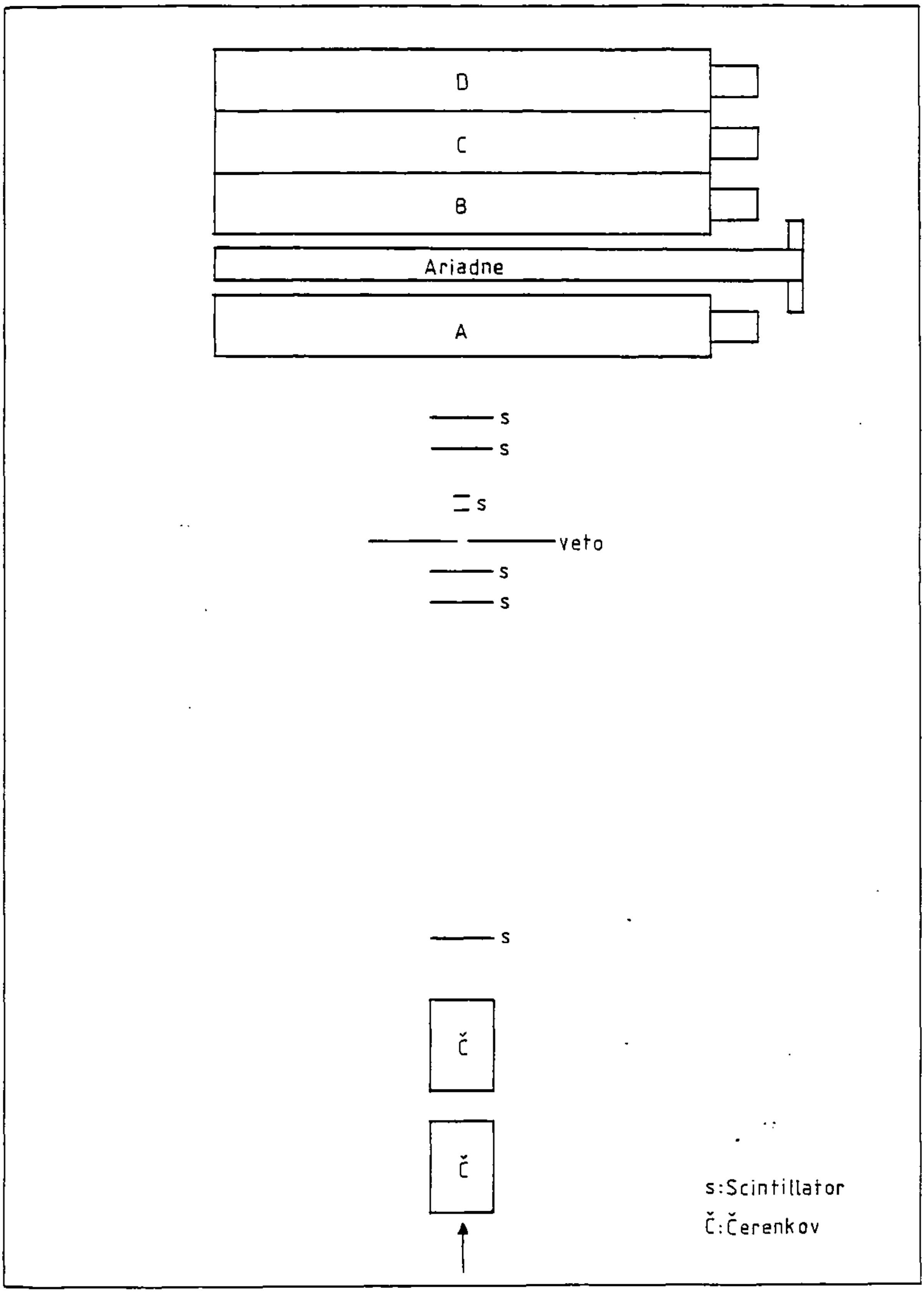

adopted setup. The A and B modules contained 7 sheets of lead each of thickness 3 mm and the C and D modules 10 sheets of lead each 3 mm thick. In terms of radiation lengths, this corresponds to about 3.5 X_0 for the A and B, and 5 X_0 for the C and D.

3.1.2 Data Acquisition

Data acquisition was performed by a Hewlett-Packard HP-21 series computer running a software system written by the Data Handling division of CERN. The user interface for the system was written by C. Williams and D. Pittuck of the Imperial College group. The computer performed the following tasks

1. Readout of the ADC's and Pattern units and writing of events to magnetic tape.
2. Monitoring the gains of the calorimeter photomultipliers.
3. Monitoring of the High Voltage supply.
4. Online booking, filling and display of histograms of user selectable ADC channels.

3.1.3 Calibration and Monitoring

The gains of all the photomultipliers were equalized using relativistic muons. For Ariadne, the high voltage was adjusted so that a relativistic muon produced a signal of about 15 ADC channels. Using the calibration scintillator block, the gains of the calorimeter module PMs were set so that the passage of a relativistic muon through this block produced a signal of about 200 ADC channels.

During periods of data taking, the gains of the Ariadne photomultipliers were monitored by means of light from a Krytron pulser that was fed via the optical fibres to each of the scintillator fingers. The calorimeter module PM gains were monitored using the light output from LEDs that were flashed at regular intervals. The flashing was done during the beam spill to allow for the possibility of compensating for PM gain sag that might be caused by the flux of particles. Muon calibration runs were performed at frequent intervals to correct for any drift in the light output from the Krytron pulser or the LEDs.

3.1.4 Linearity and Energy Resolution of ILSA

The pulse height distributions in each of the calorimeter modules for 6 GeV electrons is shown in Figure 3.4. For each event at a particular beam momentum, the sum

$$E_i = A_i + \alpha B_i + \beta C_i + \gamma D_i$$

is a measure of the energy of the incident particle. A_i, B_i, C_i, D_i are the observed signals for the i'th event in the respective calorimeter modules. The constants α, β, γ represent the relative gains of each of the modules and were obtained by minimizing the variation in E_i. This analysis showed that the values of α, β and γ were close to unity. One would expect them to be exactly one if the gains of the PMs were equalized, the ratio of sampling thickness to total thickness is the same for each module and none of the photomultipliers saturate.

Figure 3.4

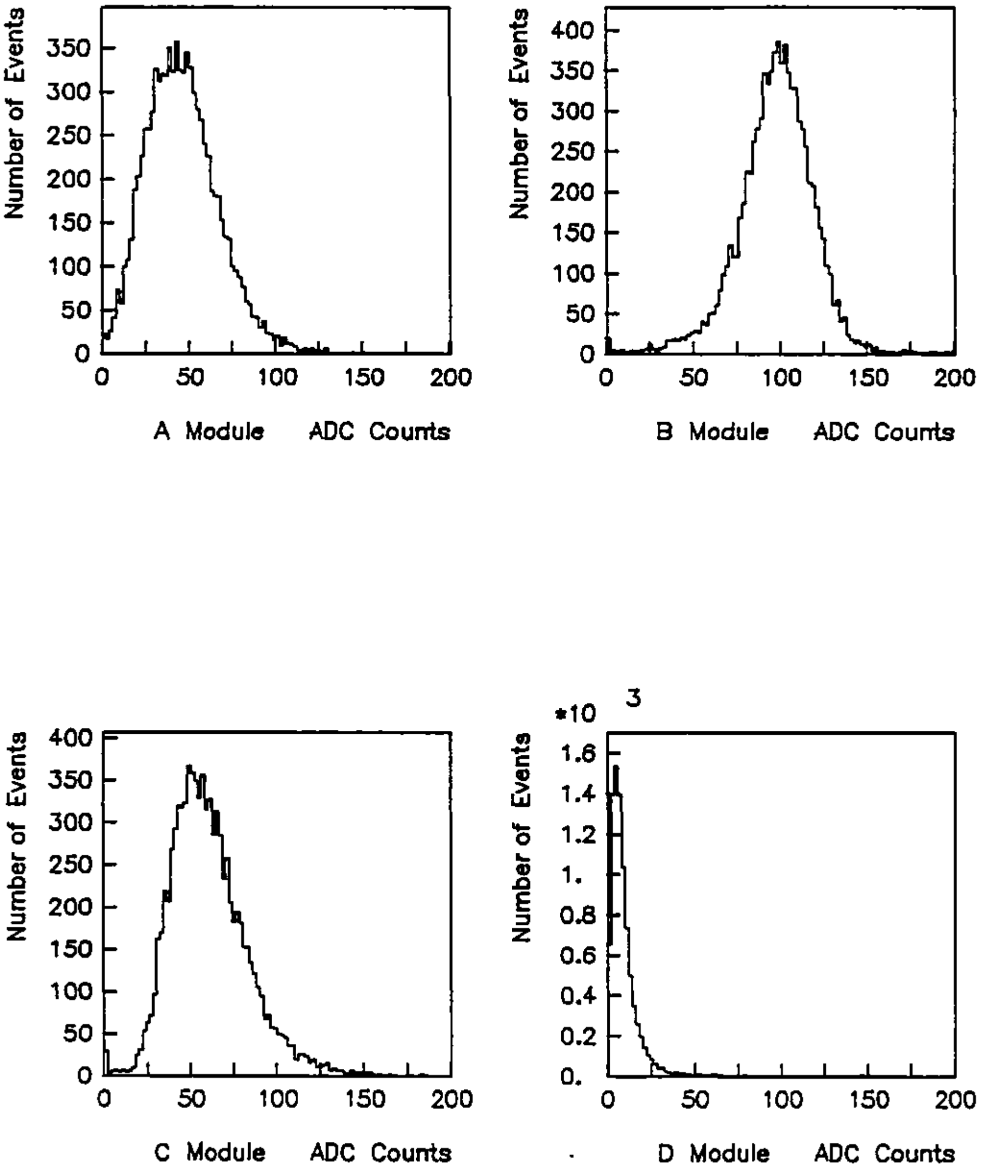

6 GeV Electrons

Setting α, β, γ to unity, the energy resolution is given by the width of the distribution of $A_i + B_i + C_i + D_i$. Figure 3.5 shows such a distribution for 6 GeV electrons. A gaussian is fitted to the distribution to give its σ and the above analysis is repeated for each value of beam momentum. The results are summarized in Table 3.1 and Figure 3.6 shows the fractional energy resolution as a function of energy.

One would expect the fractional energy resolution σ/E to be proportional to $1/\sqrt{E}$. A good fit to the data up to 40 GeV is obtained with the relation

$$\frac{\sigma(\mathrm{FWHM})}{E} = 1 + \frac{35\%}{\sqrt{E}}$$

where E is measured in GeV. This function is plotted as the solid line in Figure 3.6.

The improvement in resolution, over the WA-11 configuration, is close to the naively expected factor of $\sqrt{2}$. When the C and D modules had lead sheets of 6 mm thickness, the resolution degraded (except for low energies) and the results for this configuration are also shown in Figure 3.6(solid squares).

It is interesting to compare the measured resolution with that predicted by the Amaldi formula (section 2.1.5). Substituting the relevant parameters into the equation it predicts a value of about $25\%/\sqrt{E}$ for the fractional error (FWHM) in the energy measurement due only to sampling fluctuations. The cutoff energy E_c was taken to be 1 MeV and the fractional useful track length for this value of E_c was estimated from Figure 2.1.

Figure 3.5

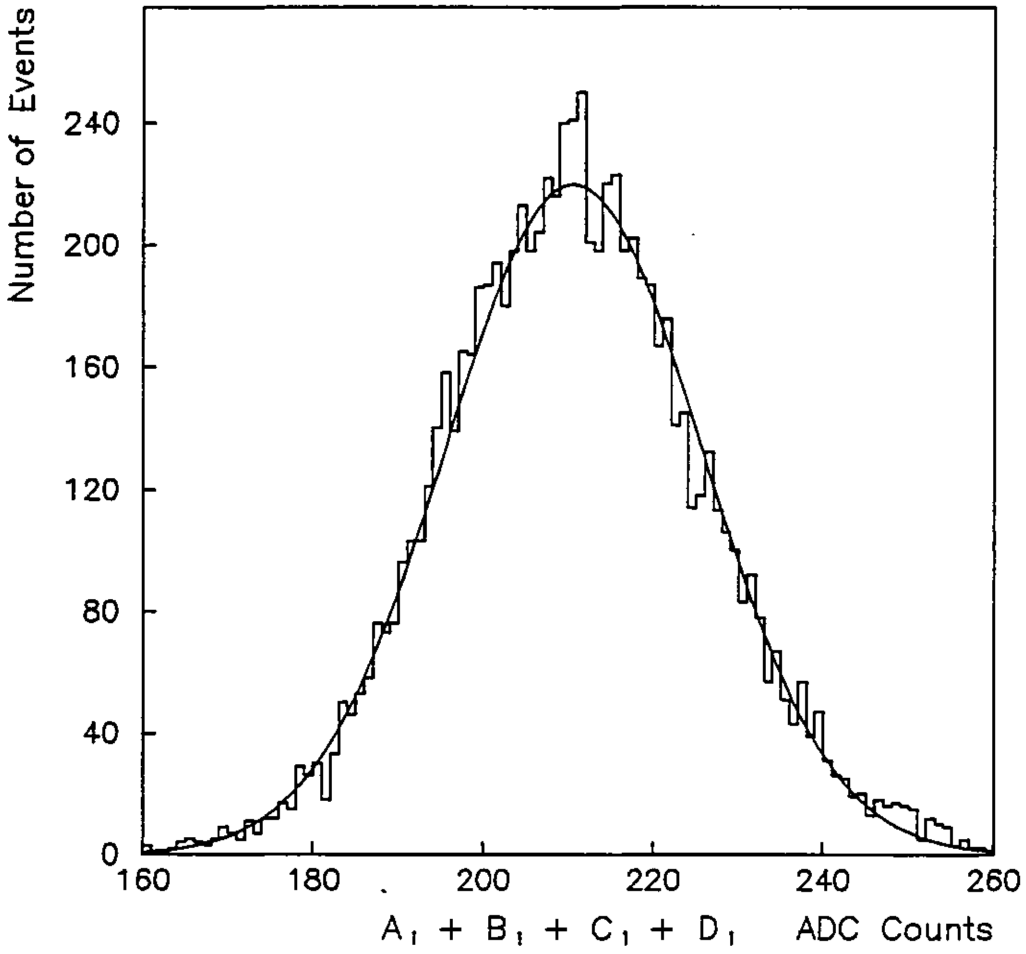

6 GeV Electrons

Figure 3.6

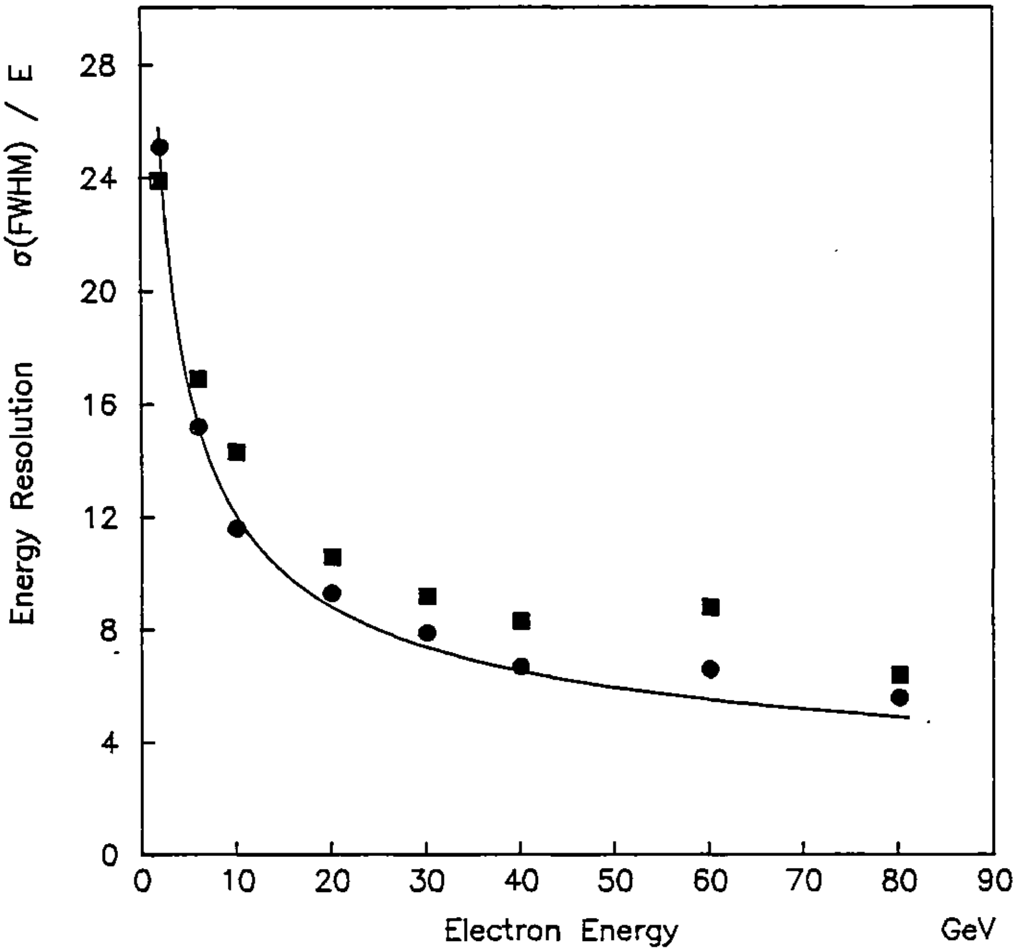

Energy Resolution σ(FWHM) / E
28
24
20
16
12
8
4
0
0
10
20
30
40
50
60
70
80
90
Electron Energy
GeV

TABLE 3.1

ILSA Energy Resolution and Linearity

Momentum GeV/c	Peak ADC Counts	FWHM ADC Counts	Resolution %
2	71.9	17.9	24.9
6	236.0	35.4	15.0
10	390.0	44.3	11.4
20	816.0	74.3	9.1
30	1240.0	95.2	7.1
40	1600.0	103.0	6.5
60	2450.0	157.0	6.4
80	3180.0	170.0	5.4

If the response of the calorimeter is linear, one would expect the peak value of the distribution of $A_i + B_i + C_i + D_i$ to be directly proportional to the incident energy. Figure 3.7 shows this relationship. The response is fairly linear upto an incident momentum of 80 GeV/c.

3.1.5 Linearity of Ariadne

Ariadne samples the shower after 3.5 X_0 and provides a measure of the number of particles and their lateral distribution at this depth in the shower. Figure 3.8 shows the average shower profile expressed in terms of the number of equivalent minimum ionizing particles at various values of the incident energy. The lateral

Figure 3.7

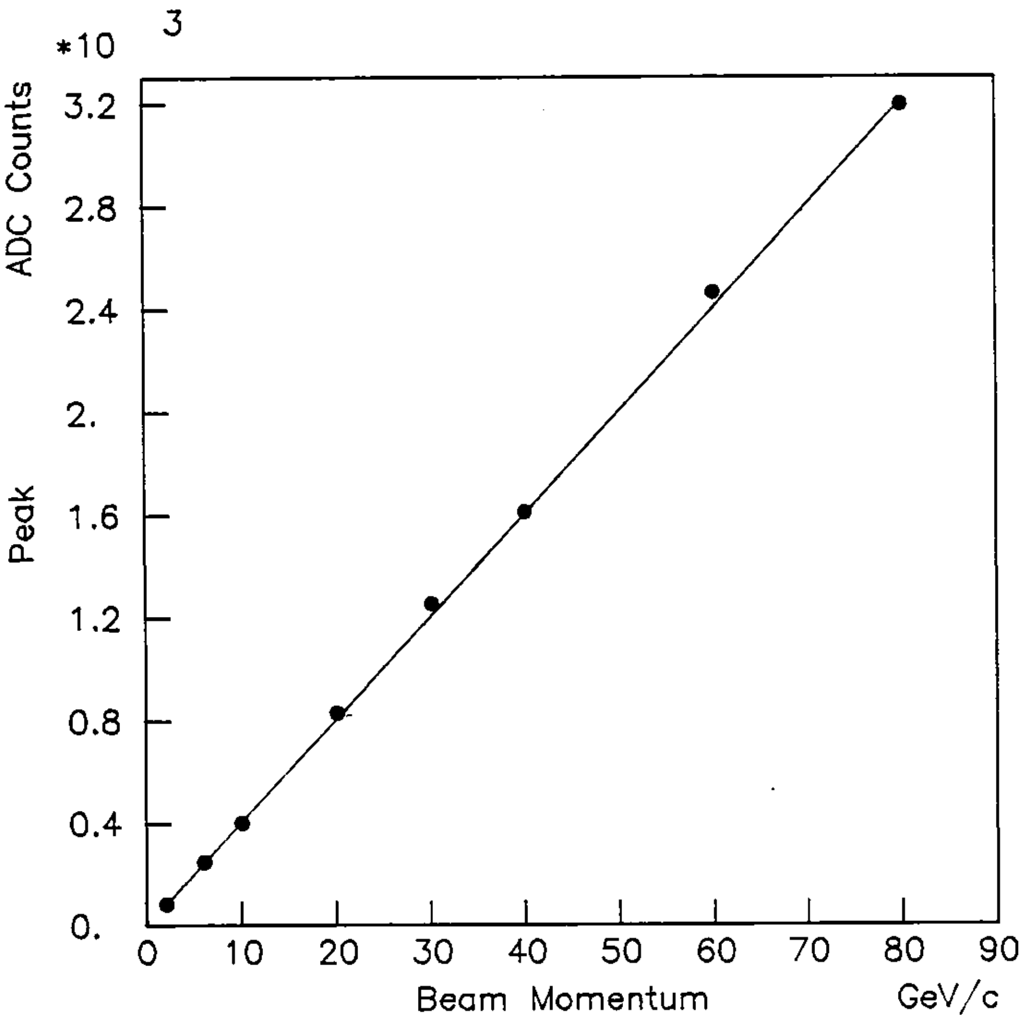
*10 3
Peak ADC Counts
3.2
2.8
2.4
2.
1.6
1.2
0.8
0.4
0.
0
10
20
30
40
50
60
70
80
90
Beam Momentum
GeV/c

Figure 3.8

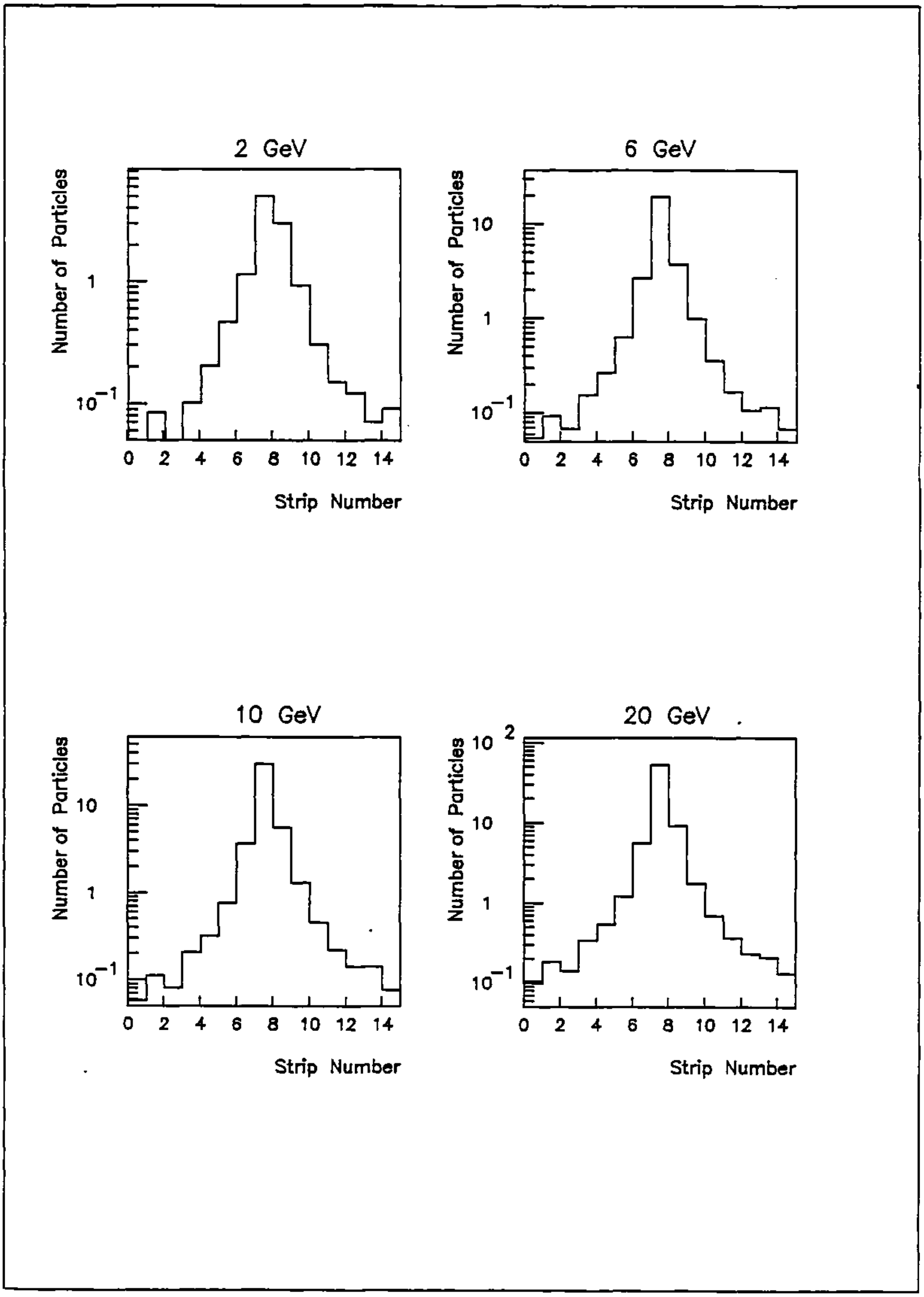
2 GeV
6 GeV
10 GeV
20 GeV
Number of Particles
Strip Number
10^{-1}
1
10
10^{2}
0
2
4
6
8
10
12
14

profile should be exponential and Figure 3.9 shows the result of fitting a function of the form

$$Y = C_1\exp[-|x-\langle x\rangle|/b_1] + C_2\exp[-|x-\langle x\rangle|/b_2]$$

to the lateral profile for 20 GeV electrons. In the above expression, $\langle x\rangle$ is the calculated centre of gravity of the shower. The lateral attenuation parameters, b_1 and b_2, are determined to be 6.5 and 35.6 mm respectively. They are only weakly dependant on the incident energy.

The total number of particles in the shower should depend on the incident energy, Figure 3.10 shows this dependance. As can be seen from this figure, the measurement made by Ariadne agrees fairly well, apart from an overall normalization, with the Universal Shower curve [ABS] up to incident energies of 40 GeV.

3.1.6 Position Resolution

The position of the incident electron was calculated from the centre of gravity of the lateral energy deposition as measured by Ariadne. The distribution of calculated centre of gravity for 6 GeV electrons is shown in Figure 3.11. A gaussian fit to this distribution gives a value for the FWHM. The dependance of FWHM on incident energy is shown in Table 3.2. The relatively poor resolution at 2 GeV of incident energy is due to statistics; the number of relativistic particles in the shower is small (about 16; see Figure 3.10) and the fluctuations are large.

As discussed in the chapter on Calorimetry, the centre of gravity does not represent the true position of the incident

Figure 3.9

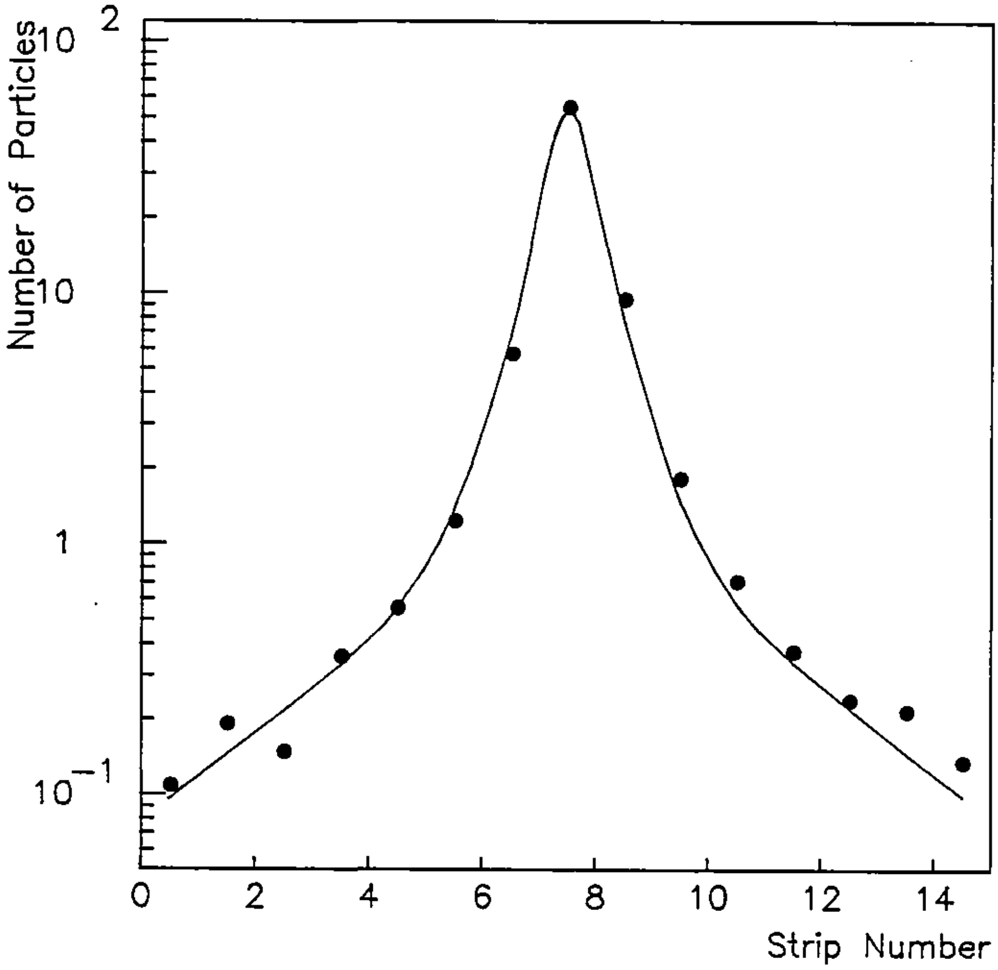

Figure 3.10

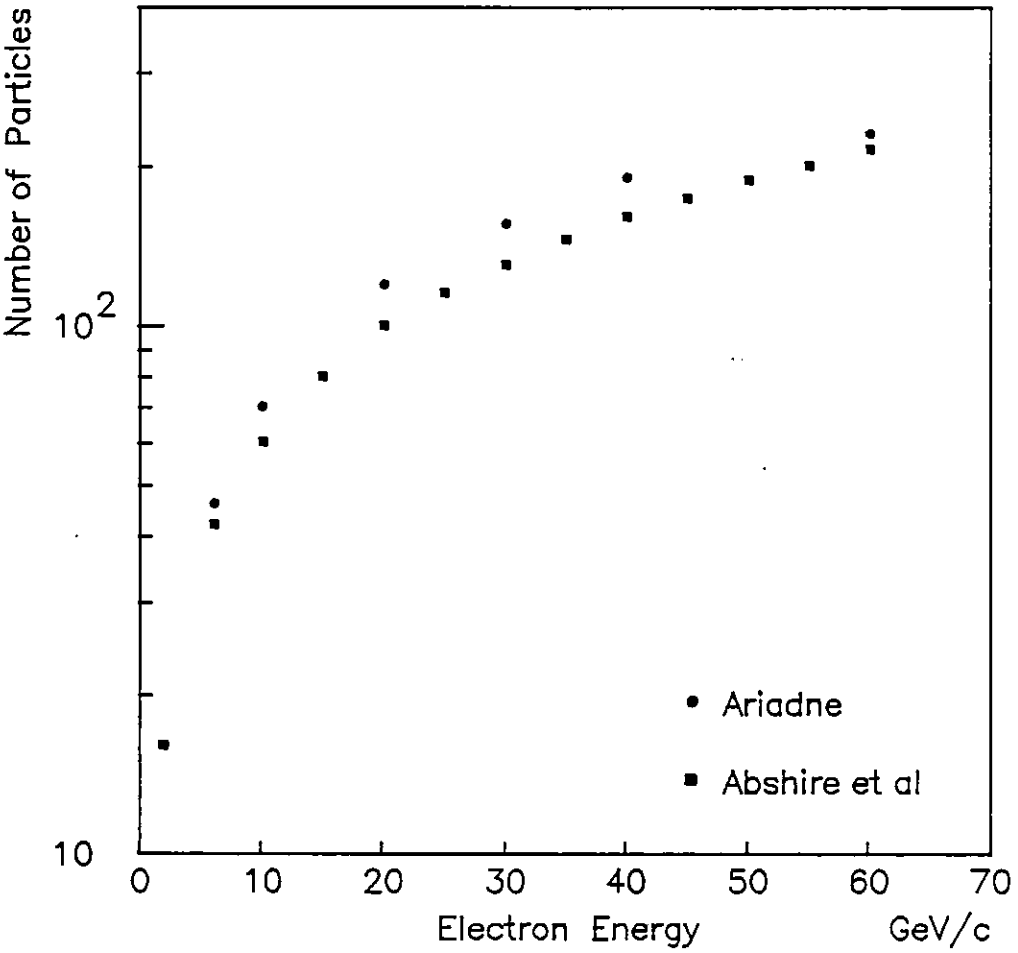
Number of Particles
10
10^2
0
10
20
30
40
50
60
70
Electron Energy
GeV/c
● Ariadne
■ Abshire et al

TABLE 3.2

Ariadne Position Resolution

Momentum GeV/c	FWHM mm
2	15.6
6	6.8
10	5.2
20	4.0
30	3.6
40	3.1
60	3.0

particle, but the correction factor is calculable. To investigate this effect, the whole detector was moved up in steps of 3 mm. The results, for 20 GeV electrons, are summarized in Table 3.3. The maximum discrepancy is about 3 mm. Since the value of δ is small, the theoretical maximum discrepancy is also small and only about 2 mm, in good agreement with the measured value given the uncertainty in the 3 mm step (± 1 mm) by which the detector was raised. Recall that $\delta = \Delta/b$ where Δ is the half width of a strip and b is the characteristic shower width.

When the beam is aligned with the gap between two fingers, one would expect the position resolution to degrade because part of the shower escapes detection. In this case the observed resolution for 20 GeV electrons is σ(FWHM) = 7.8 mm. A similar effect should

Figure 3.11

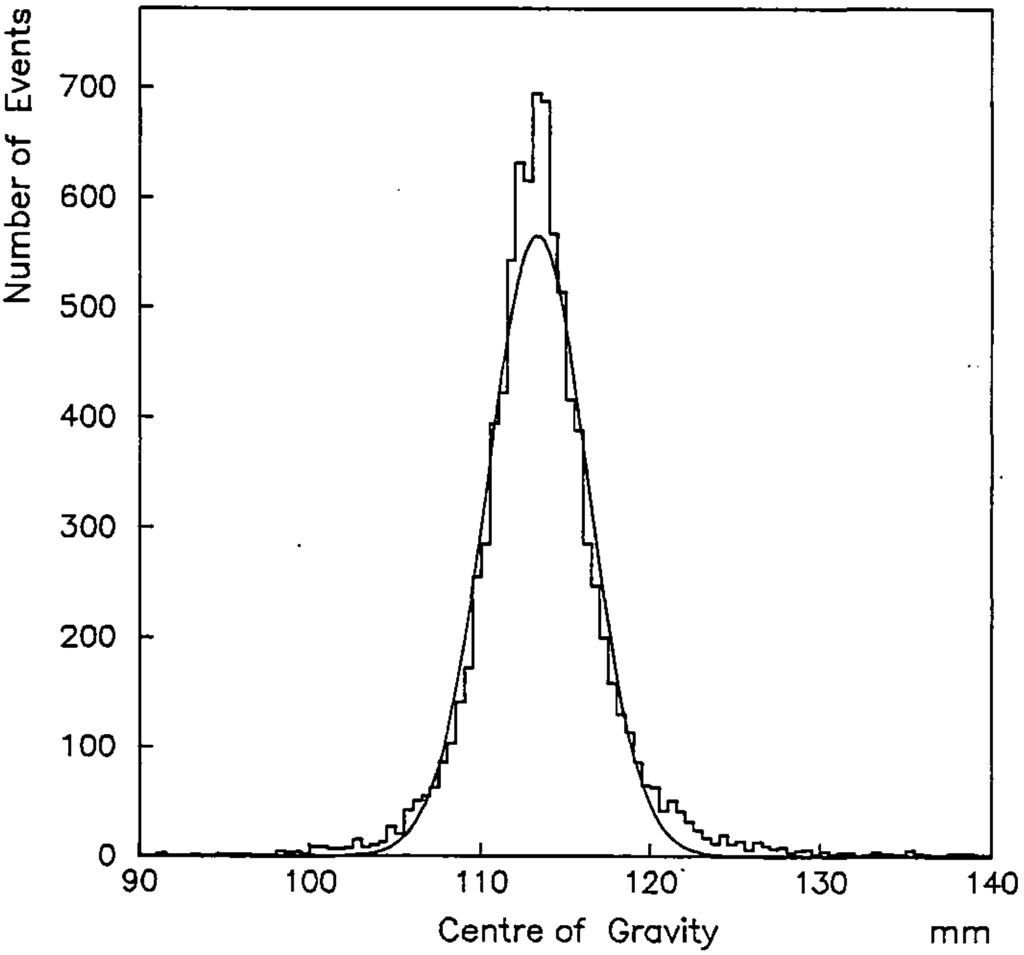
Number of Events
0
100
200
300
400
500
600
700
90
100
110
120
130
140
Centre of Gravity
mm

TABLE 3.3

Centre of Gravity vs. True Shower Position

Ariadne moved by mm	Centre of Gravity mm	C. of G. moved by mm
0	114.3	0
3	112.9	1.4
6	111.4	2.9
9	107.1	7.2
12	101.6	12.7
15	98.9	15.4

occur when the beam is aligned at the junction between two Ariadne modules and the resolution in this case is σ(FWHM) = 8.0 mm, at the same energy.

3.1.7 Attenuation Corrections

In order to calculate the energy of an incident particle, a correction must be made to the observed signal to compensate for the attenuation of light in the scintillator of the calorimeter modules. The attenuation as a function of distance from the PM is not a simple exponential as one would expect. This is caused by the fishtail shape of the light guide that tends to reflect light away from the PM for certain angles of incidence. The attenuation curve has a turnover point about 180 mm from the PM [WYL]. For

Figure 3.12

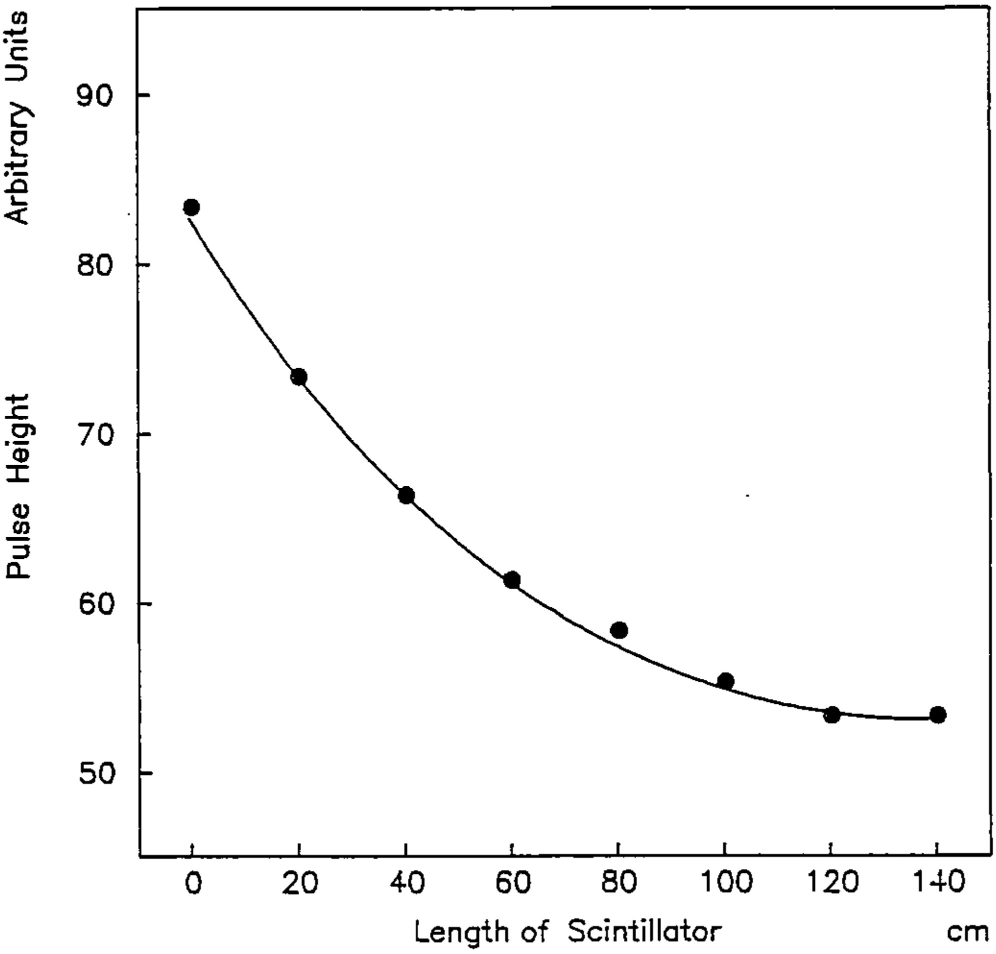

Pulse Height Arbitrary Units
90
80
70
60
50
0
20
40
60
80
100
120
140
Length of Scintillator
cm

simplicity, however, the attenuation is approximated by a function of the form

$$S(x) = S_0 \exp[\ ax + b\ ]$$

The constants a and b are determined for each module.

The attenuation curve for Ariadne is shown in Figure 3.12. It is well approximated by a function of the form

$$S(x) = S_0 \exp[\ ax + bx^2\ ]$$

Because of the large number of strips it is impractical to use different parameters for each strip. The parameters are global to all strips. Since the variation in attenuation from one strip to another is not large, this generalisation introduces no serious errors.

3.1.8 Electron-Hadron Separation

The most efficient rejection procedure is to make a cut on the fractional visible energy deposited in the calorimeter. This can be done if the energy of the incident particle is known. Figure 3.13 shows the distribution of energy deposited for electrons and hadrons of energy 6 GeV. The overlap between the two is small and a large fraction of the hadrons can be rejected.

In general, however, the energy of the incident particle is unknown. The trigger requirement in NA-14 is only that the P_t of the incident photon should exceed a certain threshold. Thus to be able to reject hadrons at the trigger level it is necessary not only to use the above cut but also to make use of the fact that the longitudinal energy deposition is different for electron and

Figure 3.13

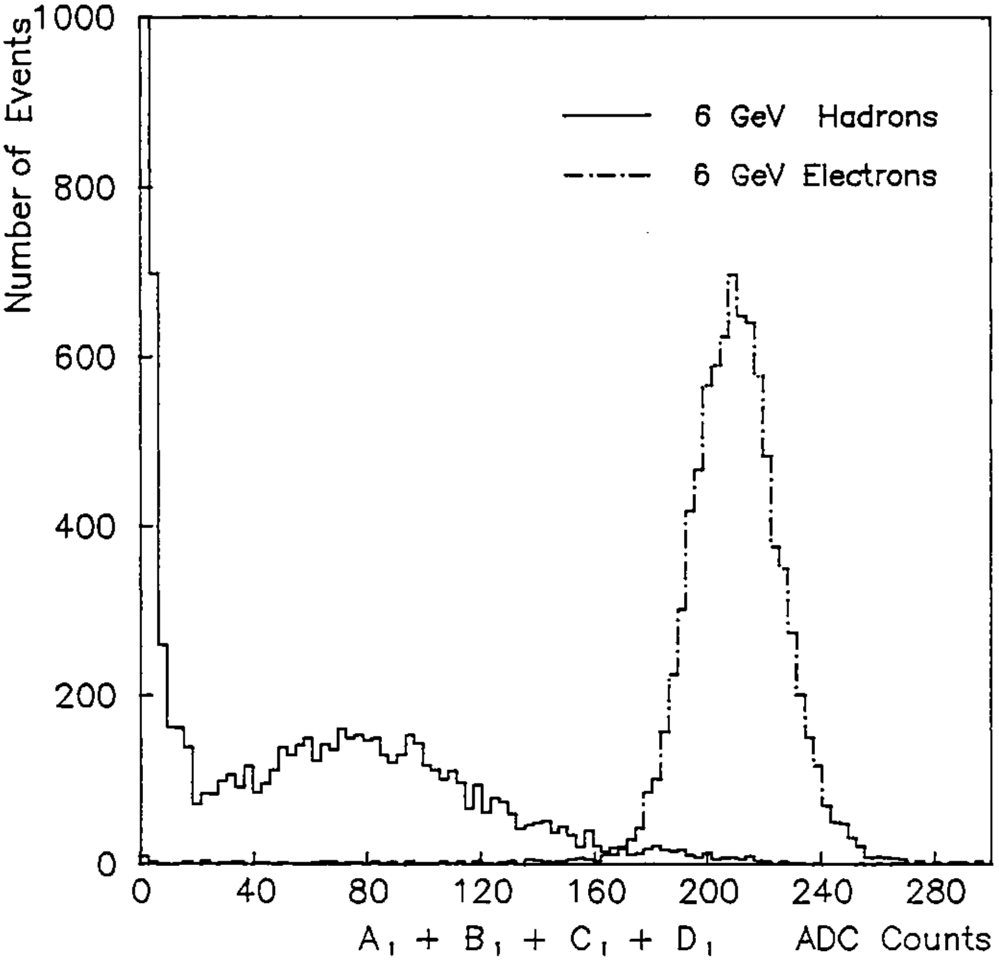

Number of Events
1000
800
600
400
200
0
0
40
80
120
160
200
240
280
A₁ + B₁ + C₁ + D₁ ADC Counts
6 GeV Hadrons
6 GeV Electrons

Figure 3.14

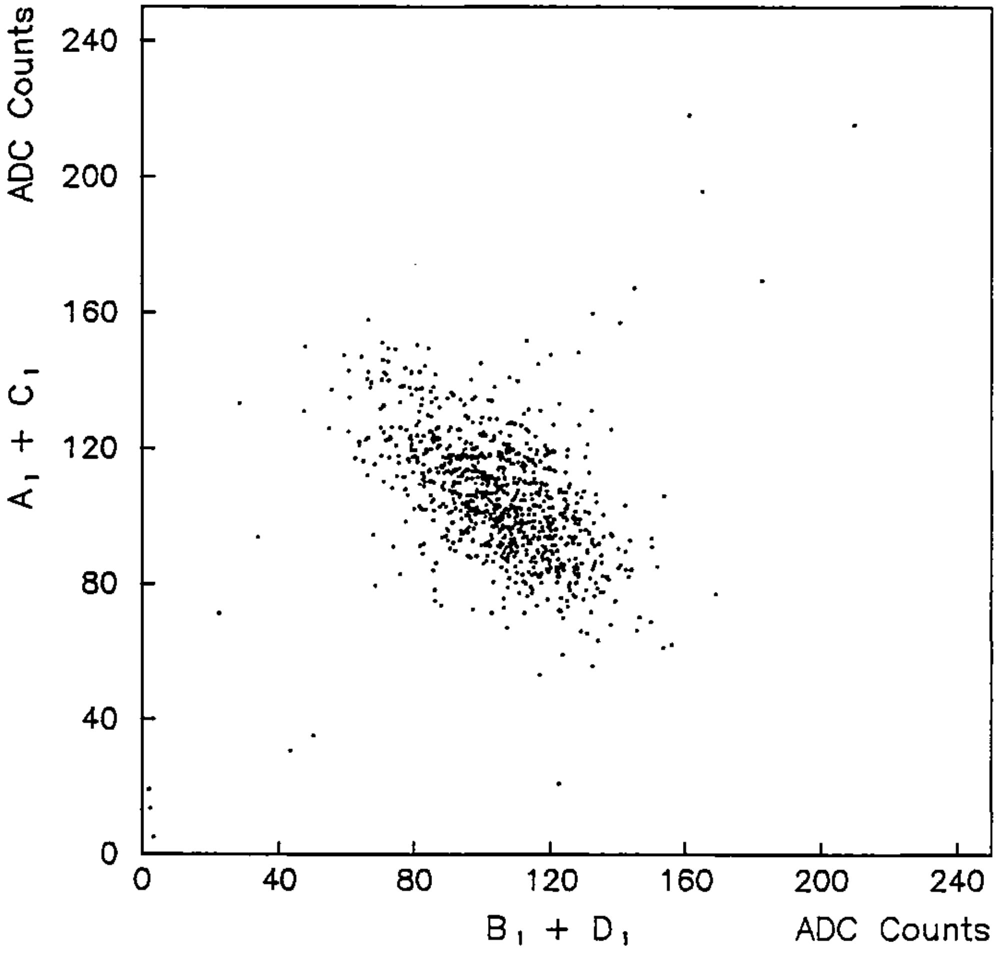

6 GeV Electrons

Figure 3.15

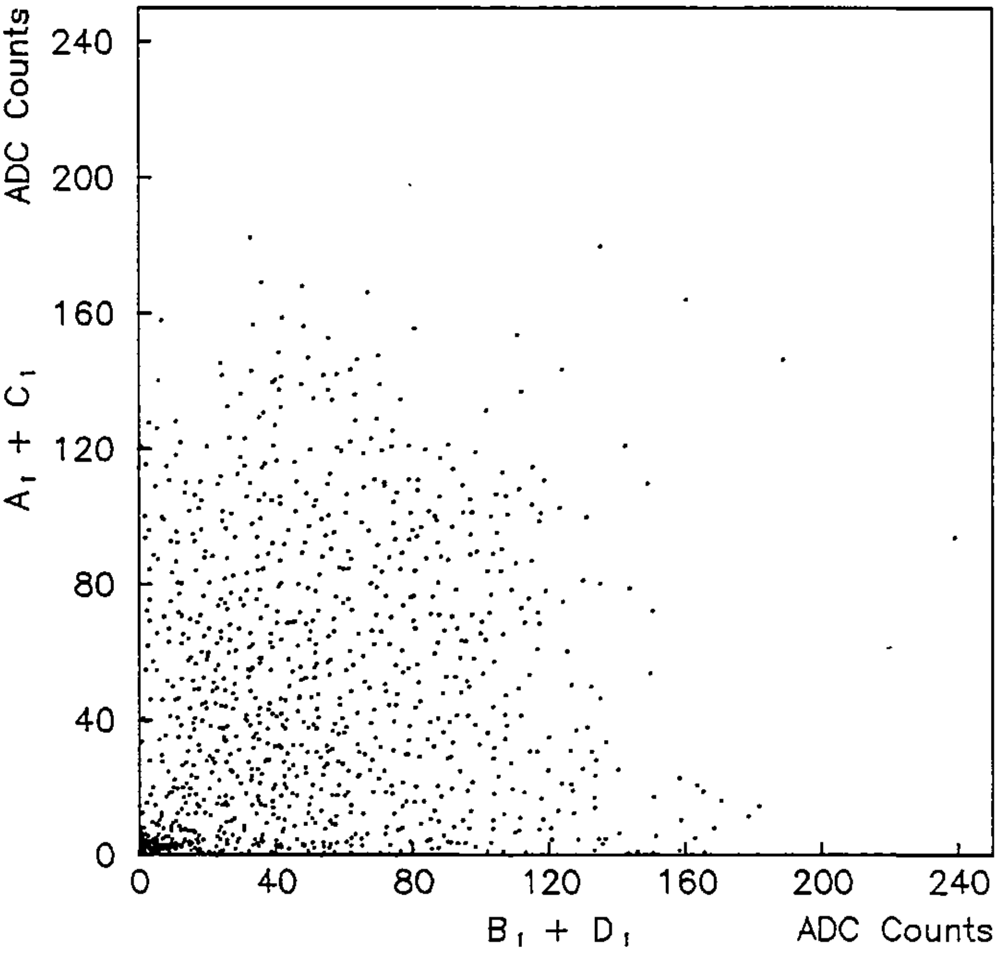

6 GeV Hadrons

hadron cascades. The sum of the signal observed in the A and C modules is plotted against the sum in the B and D modules for electrons and hadrons of 6 GeV in Figures 3.14, 3.15 respectively.

For electrons about half the energy is deposited in A+C and the other half in B+D (in fact at this value of incident energy about half the energy is deposited in B alone since the signal in the D module is only about 5% of the total, see Figure 3.4). The situation is quite different for incident hadrons. There are large fluctuations and no obvious correlation between the signal in A+C and in B+D. Thus by requiring that the energy deposit in A+C and the energy deposit in B+D both exceed a certain threshold, a significant fraction of incident hadrons can be rejected. The actual value of the rejection factor will depend on what the threshold is and on the energy distribution of the hadrons. This is because a high energy hadron could be confused with a low energy electron.

The geometrical position of ILSA in NA-14 is such that a P_t cut of 0.8 GeV/c corresponds to an incident energy of at least 5.5 to 9.0 GeV, depending on lateral position. In order to estimate the achievable hadron rejection, the thresholds are selected so that a large fraction of electrons having energies greater than 6 GeV are accepted. Then one can look at the fraction of hadrons of different energies that are accepted. Table 3.4 shows the fraction of hadrons rejected as a function of their energy and also the fraction of electrons accepted. For this analysis, the threshold on A+C and on B+D was set to be 55 ADC counts. This condition can be

TABLE 3.4

Hadron Rejection (%) as a Function of Energy

Energy GeV	Hadrons rejected	Hadrons rejected Ariadne cut	Electrons accepted	Electrons accepted Ariadne cut
2	99.5	99.9	< 0.1	< 0.1
6	95.2	97.5	98.7	97.9
10	81.4	90.5	99.0	98.8
20	65.3	79.0	99.6	99.5
30	60.1	75.8	99.6	99.5
40	59.1	75.9	99.5	99.5

fairly easily implemented in hardware and serve as a photon trigger (see section 3.3).

A further rejection is possible if information from Ariadne is used as well (Table 3.4). By requiring that at least two consecutive strips each have a pulse height corresponding to at least 1/5 of a minimum ionizing particle and that the sum of the pulse heights is at least equivalent to 3 minimum ionizing particles, the rejection improves by a factor of about 1.5-2. This cut however is not easy to implement in hardware and is best done in the offline analysis.

3.1.9 Conclusions

The H5 tests showed that a modified version of the calorimeter should be able to provide an adequate photon trigger for NA-14. These tests used incident electrons, in NA14 however, ILSA is used to detect photons. The response of a calorimeter is different for photons and electrons. Experimental observations and Monte-Carlo calculations show that the values of t_{max} and t_{med} are about 0.5-1.0 X_0 larger for photons.

To compensate for this effect and thus reduce fluctuations in the energy deposited in the A module it is necessary to introduce a passive converter of about one X_0 before the first module of ILSA. Its response to photons should then be similar to the measured response to electrons. In addition, it is necessary to incorporate a charged particle veto to reject electrons.

3.2 ILSA at NA-14

In the NA-14 experiment, ILSA is composed of four separate but essentially identical quadrants placed symmetrically about the beam direction. The front face of each quadrant is located about 13 m downstream of the experimental target. The quadrants each have a sensitive area of 1 x 1 m^2 and are separated in the horizontal and vertical directions by 2.2 m and 0.4 m respectively. Figure 3.16 shows a homothetic projection of the positions of the three electromagnetic calorimeters in NA-14.

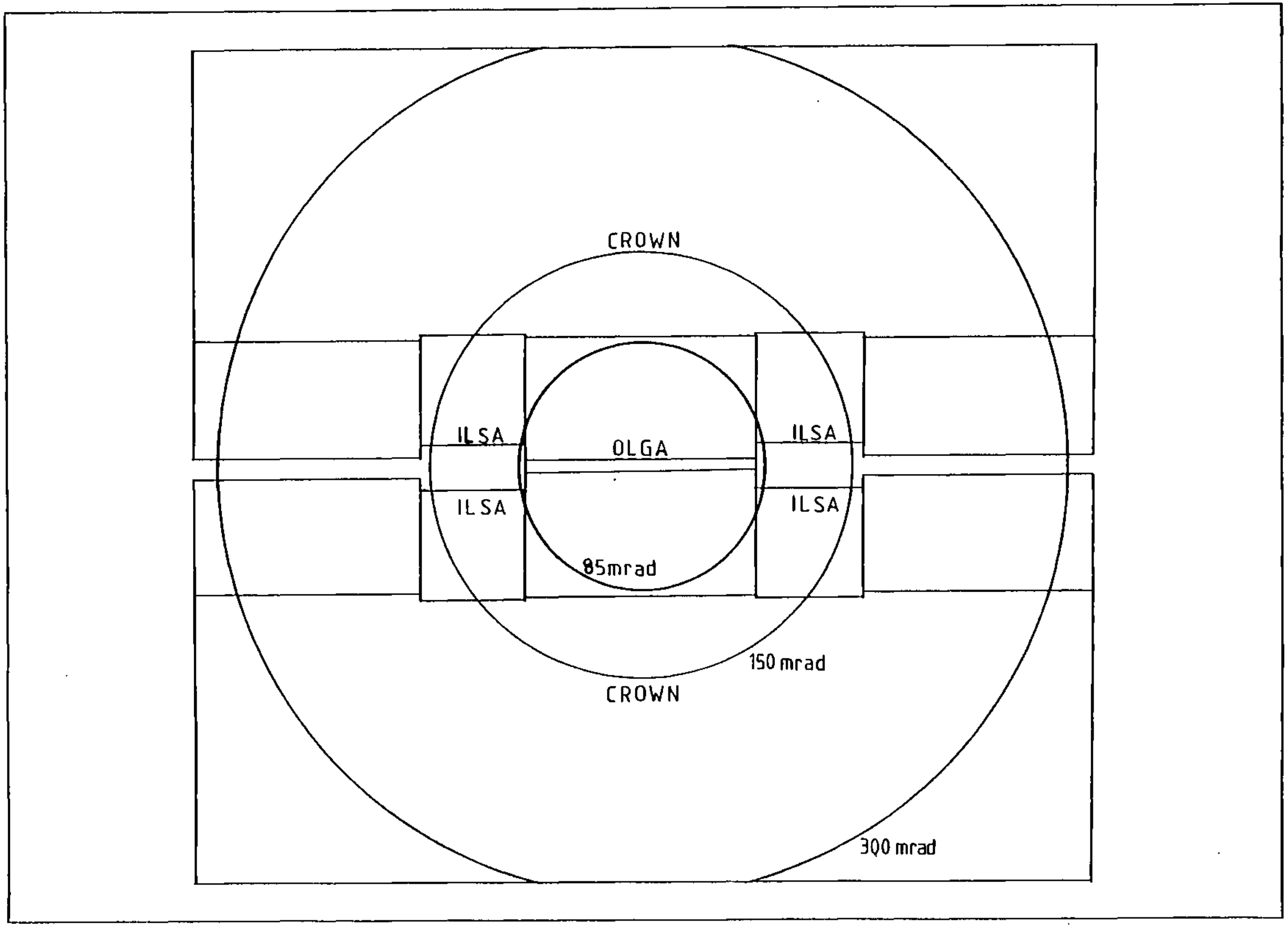
CROWN
ILSA
OLGA
ILSA
ILSA
ILSA
85mrad
150 mrad
CROWN
300 mrad

Figure 3.16

3.2.1 Layout

The layout of one quadrant of ILSA is shown in Figure 3.17. The first set of counters are charged particle vetos. They are made of slightly overlapping squares of scintillator of dimensions 260 x 260 x 10 mm^3. Each square is viewed by a separate PM. The crossings are aligned with the crossings of the calorimeter modules.

Following the veto and about 100mm downstream of it is a sheet of lead about one X_0 thick. It is a passive converter, necessary for the use of the calorimeter with photons as explained earlier. The gap between the veto and the lead sheet is there to reduce the possibility of self-vetoing that could be caused by soft electrons backscattered by the calorimeter. After the sheet of lead are 4 layers of calorimeter modules A, B, C, D. Each layer contains 4 modules and the layers are alternately aligned horizontally and vertically, the first layer being horizontal. In between the A and B layers are two planes of Ariadne modules one horizontal and the other vertical. Each plane contains 6 modules giving a total of 72 strips in each projection. In between Ariadne and the B layer is a set of 4 vertical S counters each of dimensions 1000 x 250 x 10 mm^3. The horizontal T counters are similar to the S counters and lie between the C and B planes. The S and T counters are used in the hardware photon trigger (see section 3.3).

Figure 3.17

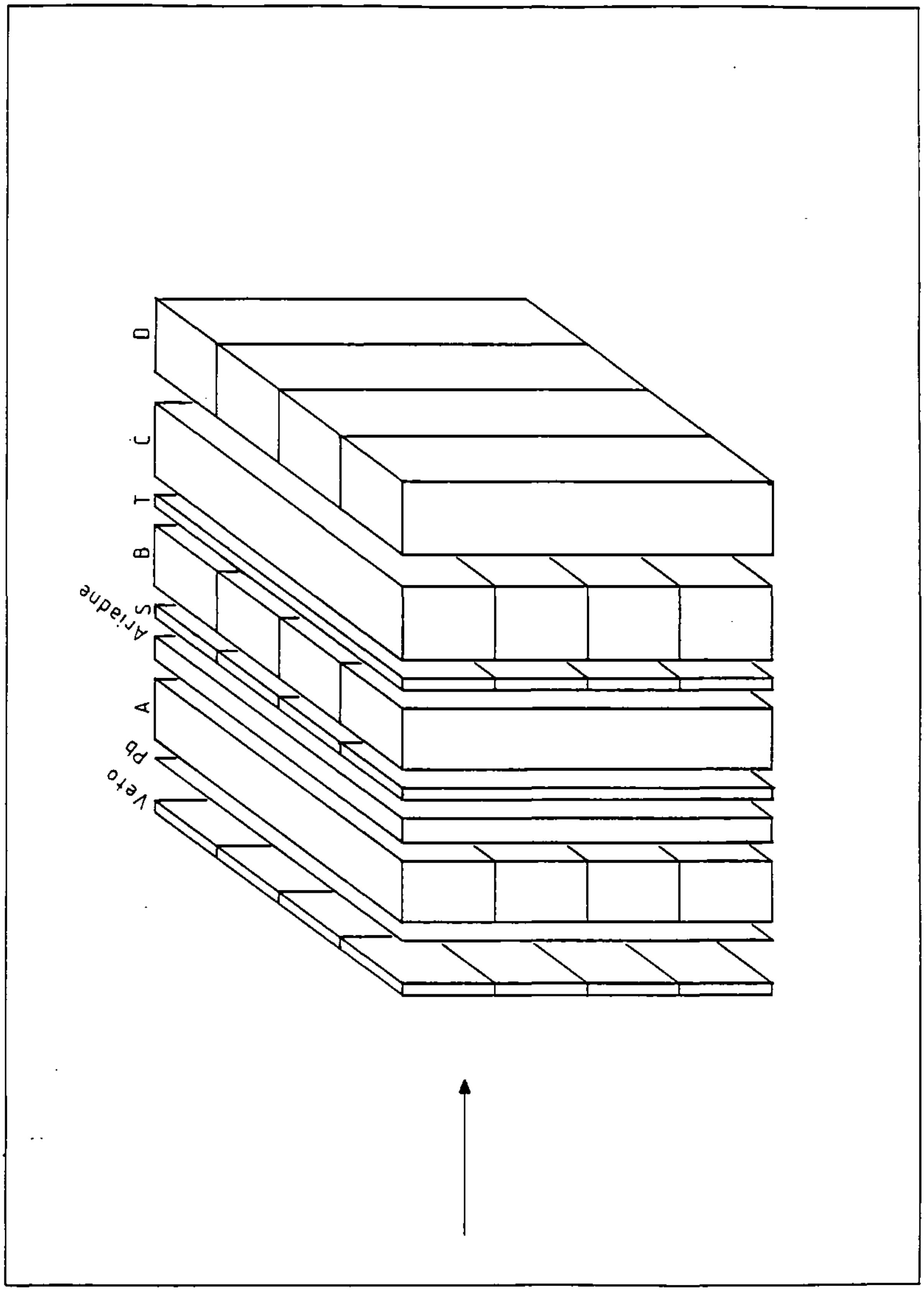

3.2.2 Electronics

The PM signals from the calorimeter modules and the S, T and V counters are split. Part of the signal is fed to the trigger electronics, the rest is digitized by ADC′s. The signals from Ariadne are directly fed into ADC′s.

The LECROY 2280 ADC system is used. Each 2282A module provides 48 channels of charge integrating ADC with 12 bit resolution. Upto 21 modules can be accommodated in a single Camac crate providing a high-density ADC system. The modules are controlled by a 2280 processor. All Camac commands and timing signals are addressed to the processor. The processor must be enabled by software, this causes it to reset the analog and digital front ends of each ADC channel in the system. When it receives a gate, the processor fans it out to the 2282A modules and initiates the conversion process. When the digitizing is completed, data from each module is serially transferred to a memory in the processor where it is stored ready to be read out.

The operation of the processor can be controlled by setting bits in its Control Word by software. Each bit enables or disables a particular function. Apart from providing raw ADC information, the 2280 offers several other useful features. These include pedestal subtraction, data compression and clusterization.

The processor contains a pedestal memory that can be loaded by software and stores a pedestal value for each channel in the system. If pedestal subtraction is enabled, the processor subtracts the pedestal values before asserting that the data is ready to be read out.

If data compression is enabled, then the data from only those channels that exceed a digital threshold (set by software and global to all channels) are stored in the memory. The data in the memory is in the form of a channel address followed by one or more data words followed by another address and more data. The Cluster Edge Size is another parameter (also set by software) that controls the data compression. It can vary from 0 to 15. If its value is N, then the data from N channels on either side of a channel exceeding the digital threshold are also available for readout. This preprocessing considerably reduces the number of data words per event and the amount of offline processing required.

3.2.3 The High Voltage System

High voltage for all the PMs in the system (apart from auxiliary Dynode supplies) is provided by one Danfysik model 150 system. It is a high density multichannel system that can be linked to a computer.

The system is controlled by a central controller designed around a microprocessor. Each high voltage channel is a DC to DC converter and two channels fit on one printed circuit card. There are 12 cards to a block. A pair of blocks is controlled by a local controller that provides the analog and digital signals required to operate the cards.

The voltage for a channel is selected by specifying a coarse and fine value. The coarse value is common to all the channels in a block and has a resolution of 20 volts. The fine value applies to each channel and can be changed in steps of 2 volts. The maximum fine value is 510 volts so two channels within the same block cannot have voltages that differ by more than 510 volts.

Communication with the computer (see chapter IV) is via a 20 mA current loop interface. This is converted to RS232-C format to enable the computer to address the system as if it were a VDU (the computer was equipped with terminal interface hardware that used the RS232-C format). The basic functions provided are

1. Select a block by specifying its number. All subsequent commands apply to this block.
2. Writing coarse and fine values for the selected block into the memory of the main controller.
3. Reading the coarse and fine memory values for a block. These numbers indicate the desired voltage and are not derived from the actual output voltage.
4. Reading of status information for a channel. This information is derived from the high voltage cards and indicates conditions such as open circuit, short circuit, out of regulation etc. It is, however, not very reliable.

3.3 The Photon Trigger

The high P_t photon trigger for a quadrant works by demanding the following :

1. The linear sum of the pulse heights in a pair of A and C counters must exceed a certain threshold. The pulse height

in at least one B counter must also exceed a threshold (the sum B+D was not used because the signal in the D counter is usually very small).

2. There must be a signal in the corresponding S and T counters equivalent to the passage of a few minimum ionizing particles.
3. The signal in the corresponding veto crossing must be less than one half of the signal produced by a single minimum ionizing particle.

The trigger condition can be represented logically by the Boolean expression

$$\sum_{i,j} T_i.(A_i+C_i).S_j.B_j.\overline{V}_{ij}$$

where the indicies i, j run from 1 to 4 for a quadrant. The '+' represents a linear sum and the Σ represents a logical sum (an OR function).

The linear sum A_i+C_i is formed using a linear fan-in. This is then fed into a LECROY type 4416 ECL discriminator. The signals from B, S, T, V are fed directly into similar discriminators. Each discriminator contains 16 channels in a single width Camac module. The threshold can be set under computer control and is common to all 16 channels. In addition, the output from any channel can be masked off or pulsed.

The actual trigger logic function is performed by special Camac modules designed and built at Imperial College. One module is required per quadrant. It receives as input the appropriate signals and produces an output signal if the trigger condition is satisfied. In addition, it has 16 output lines that indicate which crossing(s) (4i + j) produced the trigger. These signals are fed into pattern units that are read out along with the rest of the event data. Under computer control, these modules can also be instructed to remove any set of signals (eg. the veto) from the trigger requirement.

Since the discriminator threshold is common to all channels in a module, the gains of all the PMs must be roughly equalized. This was done at the start of every 10 day SPS period. The voltage on the S and T counters was raised so that they could be used to trigger on single relativistic particles. Data was collected and written to tape on the monitoring computer (see chapter IV) using only $\Sigma S_i.T_j$ as the trigger. Rough equalization was done by examining histograms of the pulse height distributions. The high voltage was adjusted so that the peak corresponding to the passage of a single relativistic particle fell in roughly the same place for each set of counters. In order to obtain accurate relative calibration constants for each calorimeter counter and Ariadne, the data tape was analysed offline. These constants were then used by the offline event reconstruction program.

Since the trigger threshold is on the P_t of the photon and not its energy, the necessary discriminator threshold is a function of the position of the corresponding counter. In order to compensate for this and ensure that the P_t threshold is more or less flat across the face of the calorimeter, the signals were attenuated by the correct amount before feeding them into the discriminators. The attenuation of light in the scintillator also contributes to an equalization since all the PMs are located away from the beam.

The final trigger is obtained by putting the photon trigger into coincidence with the experiments pretrigger. This is done individually for each of the three calorimeters and the results from the three are then OR′ed. The pre-trigger condition is selective to events in which the beam photon has interacted hadronically.

Chapter IV

DATA ACQUISITION AND ONLINE MONITORING

The successful operation of such a large number of channels requires semi-automatic methods of monitoring to perform simple checks and provide a warning of a failure in any part of the apparatus. At this stage of the experiment, my involvement with it was largly concerned with the setting up of adequate data acquisition and online monitoring facilities for ILSA. These will be described in some detail.

4.1 The Monitoring Computer

The data acquisition for NA-14 is performed by a PDP-11/45 computer. In addition to it there are two monitoring computers, a PDP-11/34 and a PDP-11/60. The 11/34 functioned as the monitoring computer for ILSA. It ran the RSX-11M operating system supplied by Digital Equipment Corporation and Data Acquisition software written by the Data Handling division of CERN. The hardware configuration of the 11/34 is shown in Figure 4.1.

The 11/34 would have to operate in two distinct modes. During periods of testing and calibration it would have control of all the electronics associated with ILSA and serve as a data acquisition computer. During periods of "real" data taking the 11/45 would perform the data acquisition for the whole experiment and

Figure 4.1

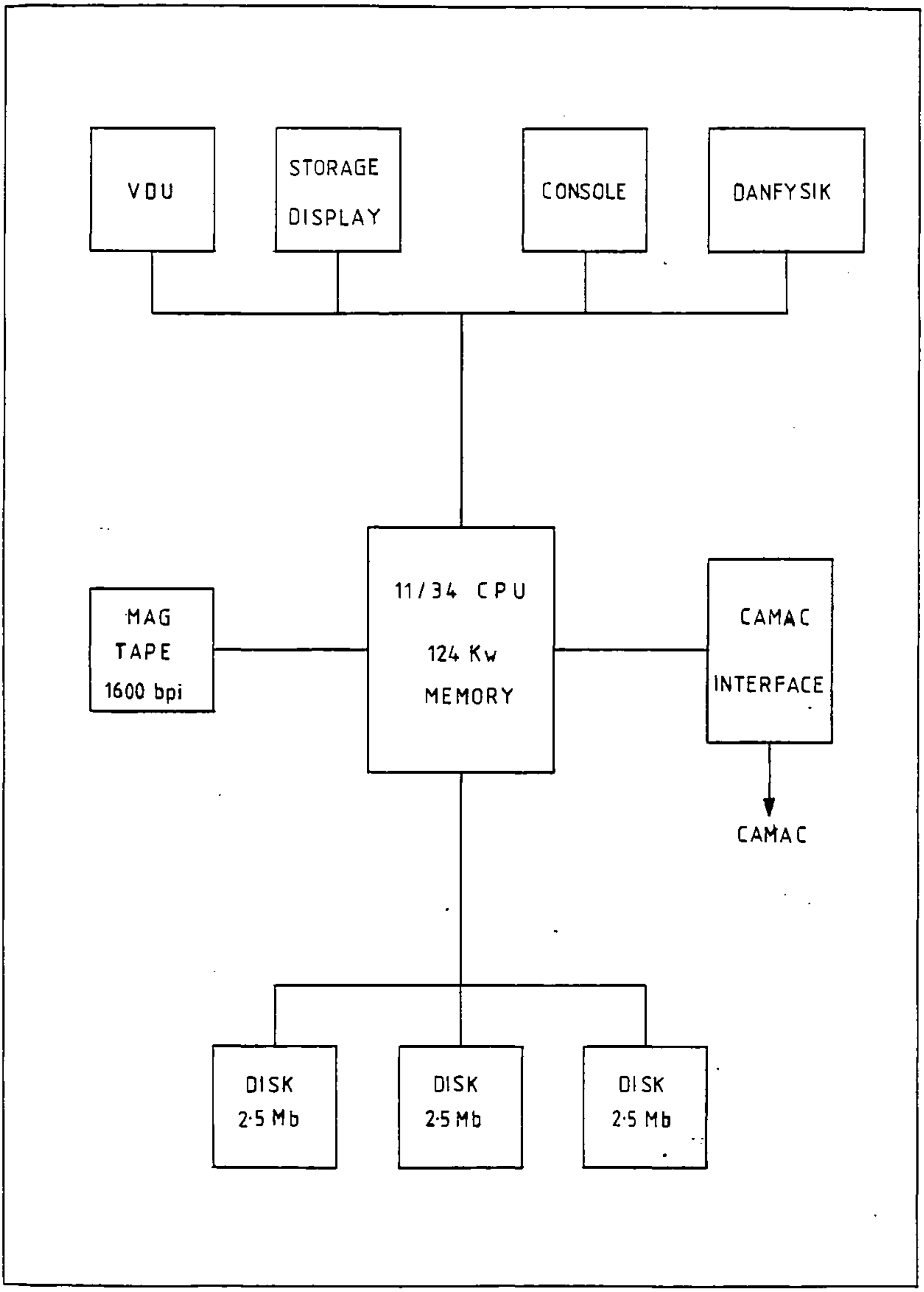
VDU
STORAGE DISPLAY
CONSOLE
DANFYSIK
MAG TAPE 1600 bpi
11/34 CPU
124 Kw MEMORY
CAMAC INTERFACE
CAMAC
DISK 2·5 Mb
DISK 2·5 Mb
DISK 2·5 Mb

the 11/34 (and 11/60) would receive events from it for monitoring. The system had to be set up in such a way as to allow an easy switchover from one mode to the other. In particular, at the level of the monitoring programs, the change should be transparent.

4.2 The Data Acquisition System

A detailed description of the CERN data acquisition system is not appropriate here. I shall only describe the general features of the system with emphasis on what had to be done to perform the data acquisition for ILSA. A detailed description of the system can be found in the Online Manual [ONL].

4.2.1 Triggers

The system would have to handle at least the following types of triggers

1. Muon calibration triggers.
2. Calorimeter LED monitoring triggers.
3. Ariadne Xenon pulser monitoring triggers.
4. Monitoring event triggers provided by the 11/45.

In general, any combination of the above trigger types can be active concurrently. All the triggers are ORed to provide a single computer interrupt. The actual trigger pattern is latched in a pattern unit and this bit pattern is used to decide what has to be done for this event. It also appears in the event header so that monitoring programs can tell what sort of event it is.

The trigger hardware layout is shown in Figure 4.2. The computer is interrupted using the front panel demand inputs of a LAM grader. There are three different types of interrupt. The SOB and EOB interrupts mark the Start of Burst and End of Burst respectively, the third is the event interrupt. The hardware is set up so that the different trigger types can be enabled or disabled under software control. This is done using a Camac output register. The different trigger signals are ANDed with the levels from the output register before being ORed to provide the event interrupt. Once an event interrupt has occured, all further interrupts are disabled by using a timing unit that functions as a flip-flop. The computer resets the timing unit when it has finished processing an event.

Access to events from the 11/45 is provided by means of a Camac memory. This memory is located in a Camac crate that can be accessed by all three computers by means of Camac branch mixer units. Synchronisation of the readout is achieved by means of a pattern unit and an output register located in the same crate. At the start of a burst the 11/34 (and/or the 11/60) clears the pattern unit. When the 11/45 has an event ready for distribution it reads the pattern unit. If the pattern unit is clear, the event is written into the Camac memory and a bit is set in the pattern unit by means of the output register. The 11/45 then generates a signal via another output register to provide an event interrupt for the 11/34 or the 11/60. In order to share the events, each machine recieves this signal every alternate burst. When the 11/34

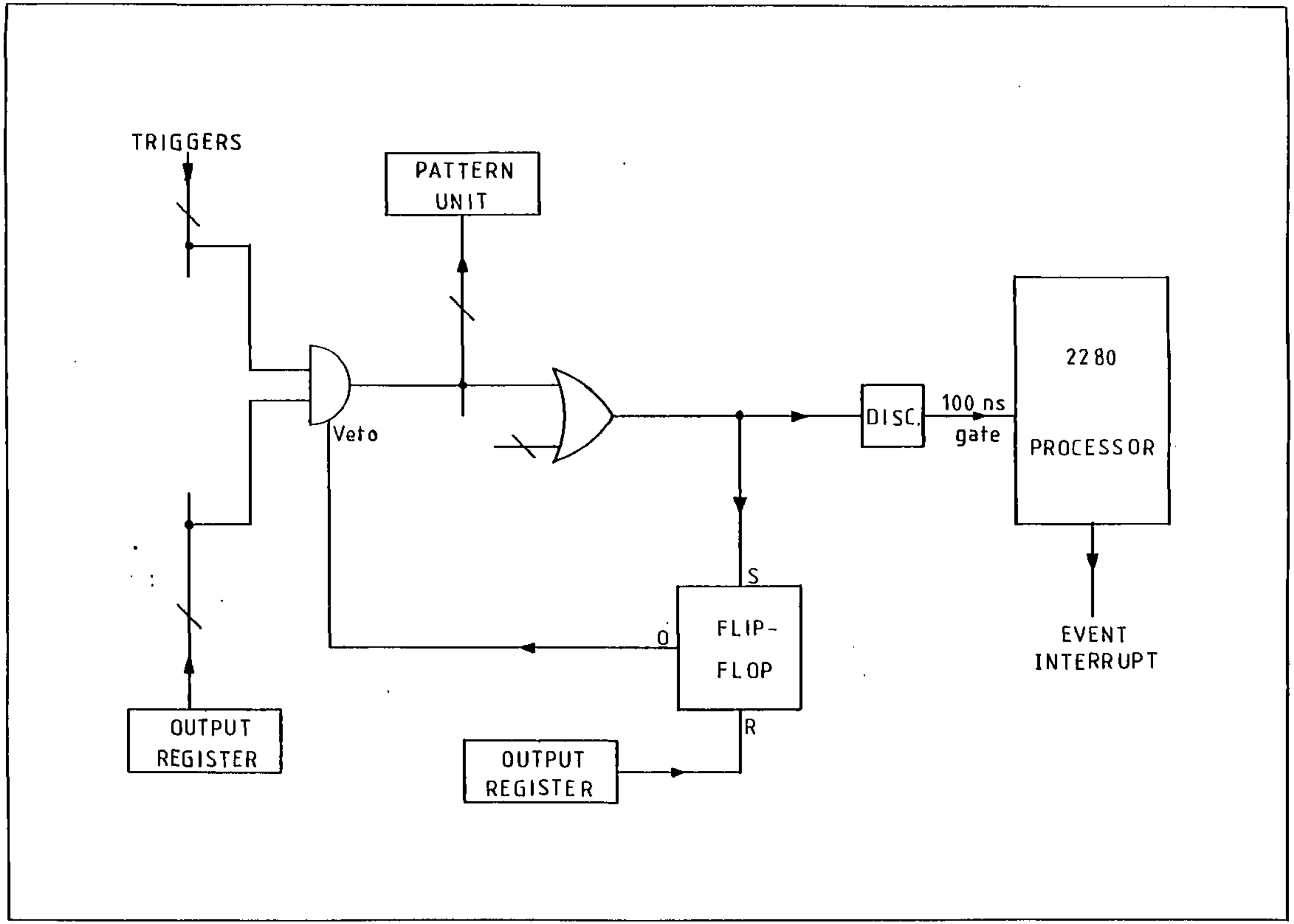
TRIGGERS
PATTERN UNIT
Veto
DISC.
100 ns gate
2280 PROCESSOR
S
FLIP-FLOP
0
R
EVENT INTERRUPT
OUTPUT REGISTER
OUTPUT REGISTER

Figure 4.2

(or 11/60) has finished reading the memory it clears the pattern unit and the cycle repeats until the end of a burst.

4.2.2 Event Readout

Data acquisition is essentially an interrupt driven Input/Output (I/O) process. In RSX, I/O with any peripheral device is controlled by the appropriate "driver". A driver for a particular device is a piece of software that is closly linked with the operating system Executive* and provides an interface between it and the device. All I/O requests are passed on to the appropriate driver via the Executive by issuing a Queue Input Output (QIO) system request.

Camac I/O operations are handled by a CERN written Camac driver. It can execute a QIO request to perform Camac read/write operations and also provides facilities for handling LAMs and Direct Memory Access (DMA) transfers. The overheads involved in executing a QIO are substantial and the system would operate rather slowly and inefficiently if a separate QIO had to be issued for each Camac operation to be performed. In order to circumvent this problem, the Camac driver can be directed to execute a whole list of Camac operations with a single QIO request. It is this feature of the Camac driver that is used to perform the event readout.

---

* Executive is the RSX name for the kernel of the operating system.

The electronics to be read out is divided into "logical pieces of equipment" identified by an equipment number that can lie in the range 1 - 32. The list of Camac commands required to perform the readout is specified for each piece of equipment. Each list has a mask associated with it. This mask is ANDed with the trigger bit pattern to decide if the list should be executed or not. Separate lists are provided to define the sequence of operations to be performed upon recieving the SOB and EOB interrupts. There may be up to 16 different SOB and EOB lists each with an associated mask. This mask is ANDed with the bit pattern of enabled triggers to determine if it is to be executed or not. These Camac lists have to be written in a language called CAM and a compiler translates the source into machine code.

There are two pieces of equipment for ILSA; the 2280 ADCs and the Camac memory. The pattern units that flag the ILSA crossing that produced the trigger are read out along with the ADCs. The mask associated with the Camac memory readout list ensures that it is only executed if the trigger came from the 11/45. For all other trigger types the 2280 ADC readout list is executed. If the 11/45 trigger is enabled, a special start of burst list is executed to clear the handshake pattern unit. At the end of a burst, scalers are read and cleared and the 2280 processor is reset. The flow of operations is shown in Figure 4.3.

The data acquisition is controlled by a program called .DAT. Upon receiving the SOB interrupt, .DAT issues the Camac list QIO. From this point the readout is controlled by the Camac driver. It

Figure 4.3

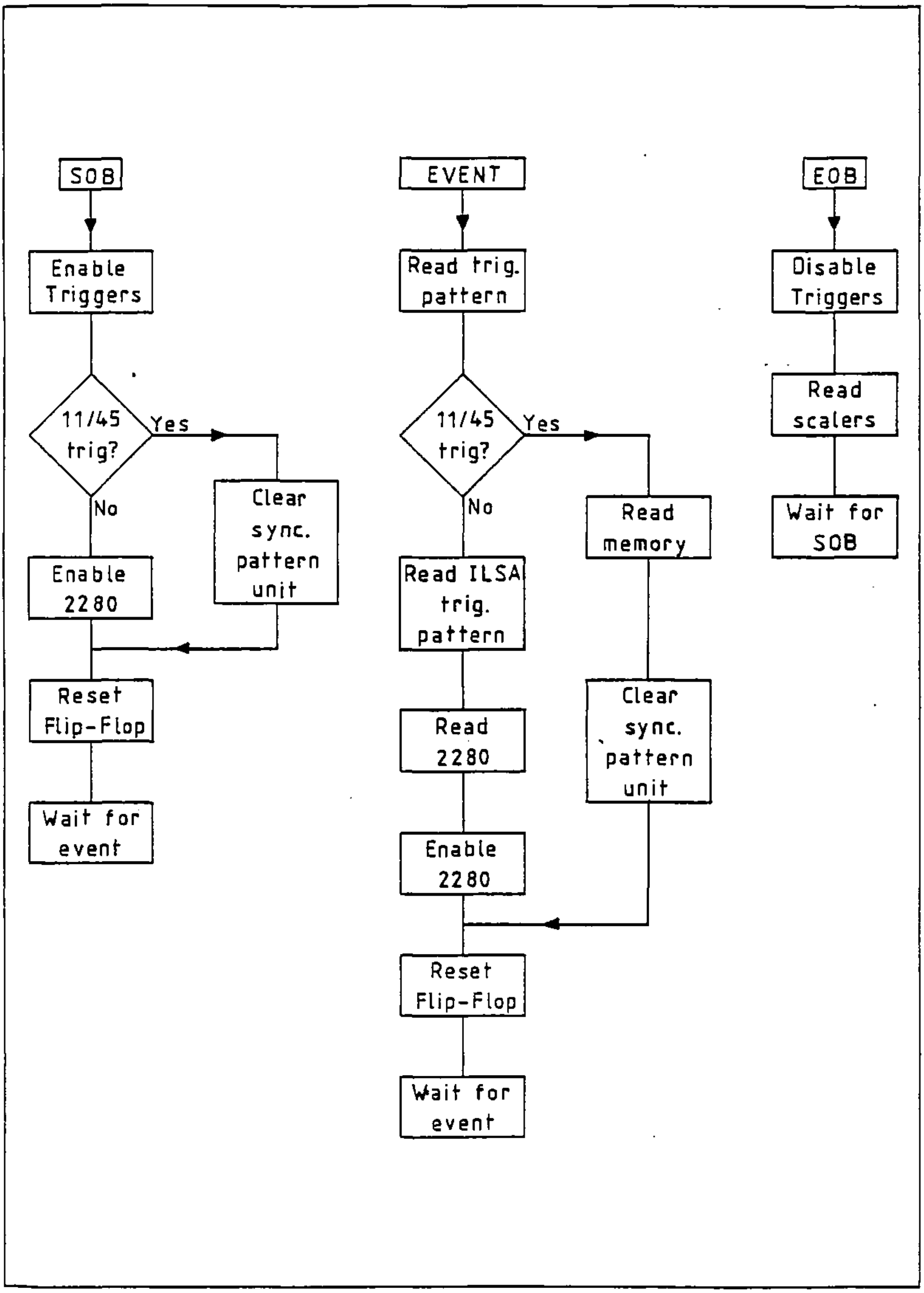
SOB
Enable Triggers
11/45 trig?
Yes
No
Clear sync. pattern unit
Enable 2280
Reset Flip-Flop
Wait for event
EVENT
Read trig. pattern
11/45 trig?
Yes
No
Read memory
Read ILSA trig. pattern
Read 2280
Clear sync. pattern unit
Enable 2280
Reset Flip-Flop
Wait for event
EOB
Disable Triggers
Read scalers
Wait for SOB

signals completion of the QIO and returns control to .DAT if there is a fatal error in the readout or when it has finished executing the EOB lists.

The events are stored in a buffer and written to tape when the buffer is full (if tape writing has been requested for the run). Outside the burst, .DAT controls the distribution of events to the various monitoring programs.

4.2.3 Start of Run Operations

The starting and stopping of runs is controlled by a program called .RUN. Options for a run such as requesting tape writing are also controlled by it. Provision is made for incorporating experiment dependent start of run operations.

For ILSA, routines were written to setup the parameters of the 2280 processor and the option of loading its pedestal memory. If pedestal loading is requested, the computer generates 50 software triggers outside the beam spill, reads all the ADCs and calculates an average for each channel. These averages are then loaded into the 2280 pedestal memory. Then, pedestal subtraction is enabled on the 2280 processor and a further 50 software triggers are generated. The average for each channel should be close to zero if the pedestal table is correct. Should the average for a channel differ from zero by more than three counts, a warning message is printed on the console, along with the corresponding channel number. The pedestal table and the Danfysik high voltage values are then written to tape if tape writing has been enabled for the run.

4.3 Monitoring Tasks

In the jargon of RSX, a task is an executable program. Since RSX is a multi-tasking system, it is more practical and efficent to have all the monitoring functions that have to be performed shared amongst several independent tasks that can execute concurrently.

In order to ensure that each task gets a fair share of events, the software priorities of all the monitoring tasks are under the control of a program called .SCHED. The currently executing task is given a certain priority and all other tasks waiting to be scheduled are given consecutively lower priorities. Each task has a time slice or an event allocation. When the highest priority task exhausts its allocation, its priority is reduced below that of all other tasks and then all processing tasks have their priorities increased by one. A task in its communicating phase (interacting with the user) is given a high priority. When it finishes communicating it is added to this round-robin scheme at the highest priority, prematurely terminating the current tasks slice.

Over a period of time, the above scheme ensures an even distribution of events to all the active monitoring tasks and minimizes system overheads due to checkpointing (swapping a task out of core and on to disk).

In general, monitoring tasks can be classified according to their function and include:

1. Those that process events, accumulating statistics and histograms.

2. Tasks that are concerned with the control and checking of a piece of equipment such as the high voltage system.
3. Gain monitoring tasks that process calibration events and check for PM gain drifts.

For ILSA, three programs were written that fall into the first category. One of them, rather general in function, allowed the user to accumulate histogrammed pulse height distributions for a selectable range of ADC channels. The histogram information was periodically written to a disk file in a standard format. They could then be displayed on a TEKTRONIX storage display using a CERN written program.

The second task maintained histograms in which each bin count represented the number of times a particular ADC channel count exceeded a user defined threshold. This provided a useful check that all the channels were operating. The profile of the histogram reflects the distribution of particles in the experiment. It also histogrammed the spatial distribution of the photon triggers and thus provided a quick rough indication that the trigger logic was functioning correctly.

The third task in this category processed scaler counts. Trigger and beam rates were counted by 32 bit scalers that were read out at the end of each burst. This task computed the mean value of the scaler counts and printed out their normalized values. The interval between printouts and the scaler number with respect to which the normalization was done are user defined options.

Three tasks fell into the second category. One of them controlled the Danfysik high voltage system. It maintained two disk files that held the coarse and fine values for all channels in the system. One of these files was updated whenever a voltage change was made. The other was only updated under user request. Either of these files could be loaded into the Danfysik memory at any time. The high voltage for any channel (specified either by its number or by an alphanumeric mnemonic) could be changed from a terminal. In addition, it periodically read the status information for a block of channels and warned of any abnormalities via a message printed on the system console. It cycled through all blocks in the system over a period of about 20 minutes. This task was also capable of receiving instructions to change the voltage for a channel from another task in the system.

In order to control and test the trigger electronics two tasks were written. One allowed the user to change thresholds and masks on any of the discriminators. It also controlled the trigger logic units allowing any set of signals to be removed from the trigger requirement. Thus it was easy to change the P_t threshold and the trigger conditions during a run.

The other program checked that the trigger electronics was functioning correctly. It made use of the test facilities of the 4416 discriminators. By selecting the appropriate mask, any combination of outputs can be pulsed. To perform an exhaustive test of all possible combinations would require an enormous amount of time. Instead, the program selected random masks for each of the discriminators. It instructed the trigger units to remove a random set of signals from the trigger and then calculates if this combination should have produced a trigger and if so, from which crossing. This result is compared with the output from the trigger logic. If there is a difference, the program pauses and prints out each of the masks along with the expected and actual result.

Finally, a gain monitoring task that warned of possible gain changes in any of the PMs in the detector. It analysed calibration events, LED pulses for the calorimeter and Xenon lamp pulses for the position detector. For each channel it calculated a mean and a standard deviation. After it had processed a sufficient number of events, it compared the means with a disk file of reference values and printed out a message if either the percentage drift or the standard deviation was above a user defined threshold. It also has the code required to compute the approximate voltage change necessary to compensate for the drift and send a message to the high voltage control program to make the change. This feature was tested while the program was being developed but was never actually used. It was feared that it would get into a positive feedback loop and destroy PMs.

All the above programs were written in FORTRAN, except for some assembler routines. These were written in MACRO-11 and performed array, string and bit manipulations. Because of the limited virtual address space of the PDP-11 (32k words) and the limited physical memory (124k words) some of the tasks were overlaid. Although none of them actually did require more than 32k words, the resulting decrease in the task image size allowed the system to function more efficiently.

Chapter V

PHOTON RECONSTRUCTION

The offline analysis program for NA-14 is still in its development stage. As far as the photon reconstruction is concerned, it is done separately for each of the calorimeters because of their different nature. So far, no serious attempt has been made to combine the data from the calorimeters. This will be done when each of them is fairly well understood and their respective reconstruction programs have stabilized.

The photon reconstruction program for ILSA was originally written by E.J.W West. It has since been modified and improved mainly by P. Gregory and myself. I shall describe the reconstruction process for ILSA and discuss some of the outstanding problems.

Because of the lack of modularity in the calorimeter, the obvious starting point for the photon reconstruction is Ariadne. This has the added advantage that it would also provide some degree of hadron rejection as indicated by the H5 test results. Working on a quadrant basis, the general flow of operations is

1. Find clusters in each projection of Ariadne and calculate their centres of gravity.
2. Apply cuts on these clusters.
3. Associate the clusters to give impact coordinates.

4. Partition the energy in the calorimeter amongst the impacts, correcting for attenuation and using an energy sharing procedure when more than one impact falls in the same calorimeter module.

5.1 Ariadne Clusterization

This is the first non-trivial step in the reconstruction chain. The ADC counts for Ariadne are corrected by the appropriate calibration factor so that they are in units of the number of equivalent relativistic muons. The cluster finding routine scans the fingers in a plane until it encounters one that has a signal equivalent to at least 1/5 th of a relativistic muon. This marks the start of a cluster. The scan is continued until a strip is found that has less than 1/5 th of the signal produced by a relativistic muon. This marks the end of a cluster. The above procedure is repeated until all clusters in all planes have been found. For each cluster, its centre of gravity and its standard deviation are calculated.

The above criteria are rather generous. Many of the clusters found will not be genuine in the sense that they are not typical of those caused by photon showers. It is necessary to reject most of them because they do not satisfy certain cuts. The parameters for these cuts are determined from a study of the H5 data. Genuine clusters are those that possess the following characteristics:

1. They must be at least 2 strips wide.

2. The sum of the pulse heights in all strips of the cluster must exceed that produced by the passage of 3 relativistic muons.
3. The energy deposit in the A+C (B+D) modules corresponding to this Z (Y) plane cluster must be at least 0.5 Gev. If the cluster centre of gravity lies within 40 mm of the edge of a module, the energy deposit in the adjacent module is also taken into account before applying this cut. If an adjacent module does not exist, the value of the cut is reduced to 0.25 GeV. This cut effectively imposes a lower limit of about 1.0 GeV on the energy of the reconstructed photon.
4. All strips of the cluster must lie within the sensitive area of the calorimeter. This cut is necessary because the sensitive area of Ariadne is greater than that of the calorimeter.

The centre of gravity of the surviving clusters is not corrected to compensate for the discreet sampling. As discussed earlier, the maximum correction factor is small.

5.2 Cluster Association and Energy Sharing

Having found the clusters and their centres of gravity, it is now necessary to associate them to give an impact coordinate. The assignment of unambiguous space points is impossible when information on only two orthogonal projections is available and more than one cluster is present per projection. The calorimeter is of no help because the information it provides is again in the same two projections and even if it were not, it is not sufficiently modular. The only other information available is the total signal associated with each cluster. The clusters in each plane are sorted in descending order of the signal in each. They are then paired off.

Two problems have been ignored. The treatment of cases where the number of clusters in each plane is different and the fact that no correction for attenuation has been made. These problems are discussed in more detail later.

The assignment of an energy to an impact coordinate is also done in projections. The energy for a cluster in the Z (Y) plane is obtained from the signal in the corresponding A+C (B+D) modules. For each module, the clusters associated with it fall into three classes :

1. Those that are fully contained within the module.
2. Those that have their centre of gravity lying in the module but which have a tail that overlaps with an adjacent module.
3. Those that have their centre of gravity lying in an adjacent module but overspill into this module.

The energy in the module is divided amongst all the clusters that fall into the above classes. The division is done in proportion to the cluster signal that lies in the module. The program cannot handle cases where more than three clusters overlap with a single module.

This algorithm will certainly work if all the clusters belonged to the first class. Its validity for the other classes is not clear because the correlation between the cluster signal that overlaps with a module and the fraction of energy that is deposited in it is unknown. However, it is the best that can be done with the information available. Since the impact coordinates are known, the calorimeter signal can be corrected for attenuation and an impact 4-vector computed.

The data for the following analysis is part of the data collected during a 10 day run in April 1982. It was the first set of data for which most of ILSA was operating satisfactorily. The incident proton intensity varied between 2.0 10^{12} and 4.0 10^{12} protons per pulse. For ILSA, the P_t threshold was set at 800 MeV/c. Because of an uncertainty in the relative gains of the veto counters, they were excluded from the hardware trigger. Since the digitized veto signals are available for each event, their effect could be studied offline. Only those events for which the hardware trigger came from ILSA are analysed. The energy and P_t spectrum of the reconstructed trigger photon is shown in Figures 5.1 and 5.2 respectively. The effect of the trigger threshold at 800 MeV/c is clearly visible.

Figure 5.1

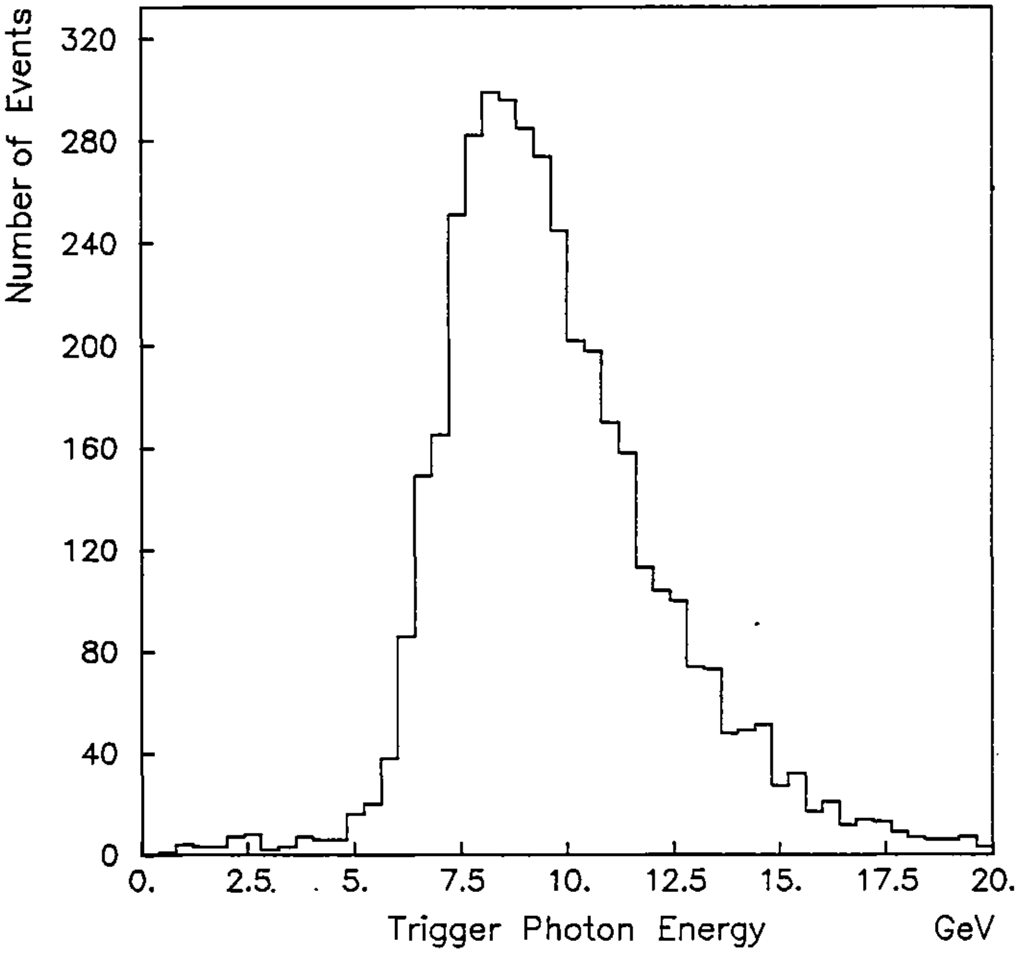
Number of Events
320
280
240
200
160
120
80
40
0
0.
2.5
5.
7.5
10.
12.5
15.
17.5
20.
Trigger Photon Energy
GeV

Figure 5.2

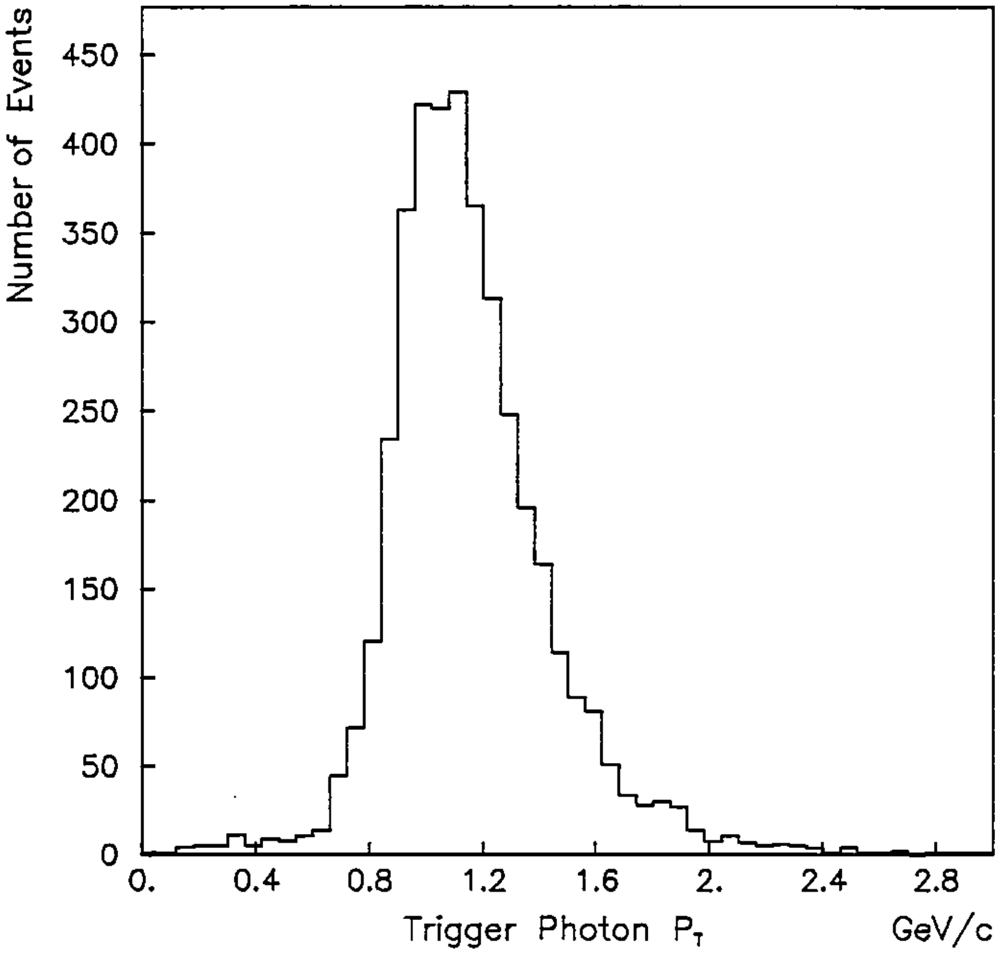
Number of Events
450
400
350
300
250
200
150
100
50
0
0.
0.4
0.8
1.2
1.6
2.
2.4
2.8
Trigger Photon P_T
GeV/c

5.3 The Pizero

An obvious test of the performance of a photon calorimeter is its ability to reconstruct the π^0 through its dominant two photon decay mode. The square of the effective mass of a pair of photons is given by the expression

$$M^2 = 2E_1E_2(1-\cos\theta)$$

where E_1 and E_2 are the energies of the two photons and θ the opening angle between them. The distribution of effective mass combinations for events that have at least two reconstructed photons in ILSA is shown in Figure 5.3. The π^0 signal is clearly visible.

There is no sign of an enhancement at the η mass (549 MeV). The reason for this is that the acceptance is very small. Except for energetic η's (> 12 GeV), the photons from an η decay cannot both lie in the same ILSA quadrant and the probability of them lying in different quadrants is small. Monte-Carlo calculations performed by P. Gregory indicate that the number of η's in the sample of events shown in Figure 5.3 is only about 60.

The energy and P_t spectrum of the π^0's is shown in Figures 5.4 and 5.5 respectively. Any pair of photons that have an effective mass lying in the range 135 ± 35 MeV/c^2 are assumed to come from the decay of a π^0. Thus the background in this sample of events is about 30%.

The width of the π^0 signal should reflect the energy and position resolution of ILSA and the relative calibration of the calorimeter modules. Assuming no correlation between the quantities

Figure 5.3

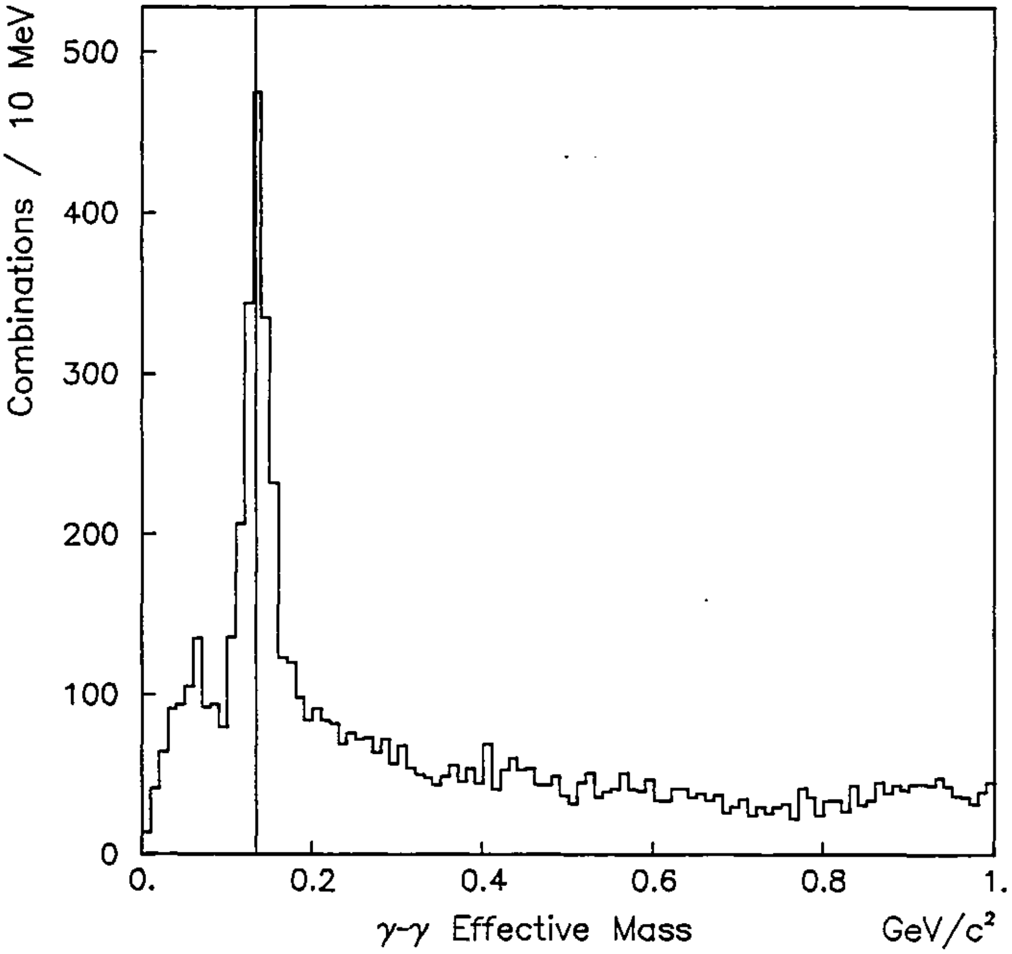
Combinations / 10 MeV
500
400
300
200
100
0
0.
0.2
0.4
0.6
0.8
1.
γ-γ Effective Mass
GeV/c²

E_1, E_2 and θ; the square of the fractional error in the effective mass is given by the expression

$$\left[\frac{\Delta M}{M}\right]^2 = \frac{1}{4}\left[\left[\frac{\Delta E_1}{E_1}\right]^2 + \left[\frac{\Delta E_2}{E_2}\right]^2 + \left[\frac{4E_1E_2}{M^2} - 1\right](\Delta\theta)^2\right]$$

A naive estimate of the expected width can be obtained from the above expression. Taking the mean π^0 energy to be 12 GeV (Figure 5.4) and the case of a symmetric decay, we have $E_1 = E_2 = 6.0$ GeV. The fractional energy resolution (FWHM) for photons of this energy (based on the H5 measurements) is about 15%. The corresponding position resolution of Ariadne is about 6 mm. Since ILSA is situated about 13 m downstream of the target, this corresponds to an angular resolution $\Delta\theta(\text{FWHM}) \simeq 0.7$ mrad. Substituting these values into the above expression yields a value of 15 MeV for the expected FWHM of the π^0 signal. The observed width is of the order of 30 MeV.

There are several factors contributing to this discrepancy.

1. Poor relative calibration of the calorimeter modules and drifts in gain.
2. Asymmetric decays of the π^0. The P_t trigger threshold tends to select asymmetric decays since, for a given π^0 energy, an asymmetric decay is more likely to produce at least one photon that satisfies the trigger requirement. Since the fractional energy resolution rapidly degrades with decreasing photon energy, the observed width is a function of the asymmetry of the decay.

Figure 5.4

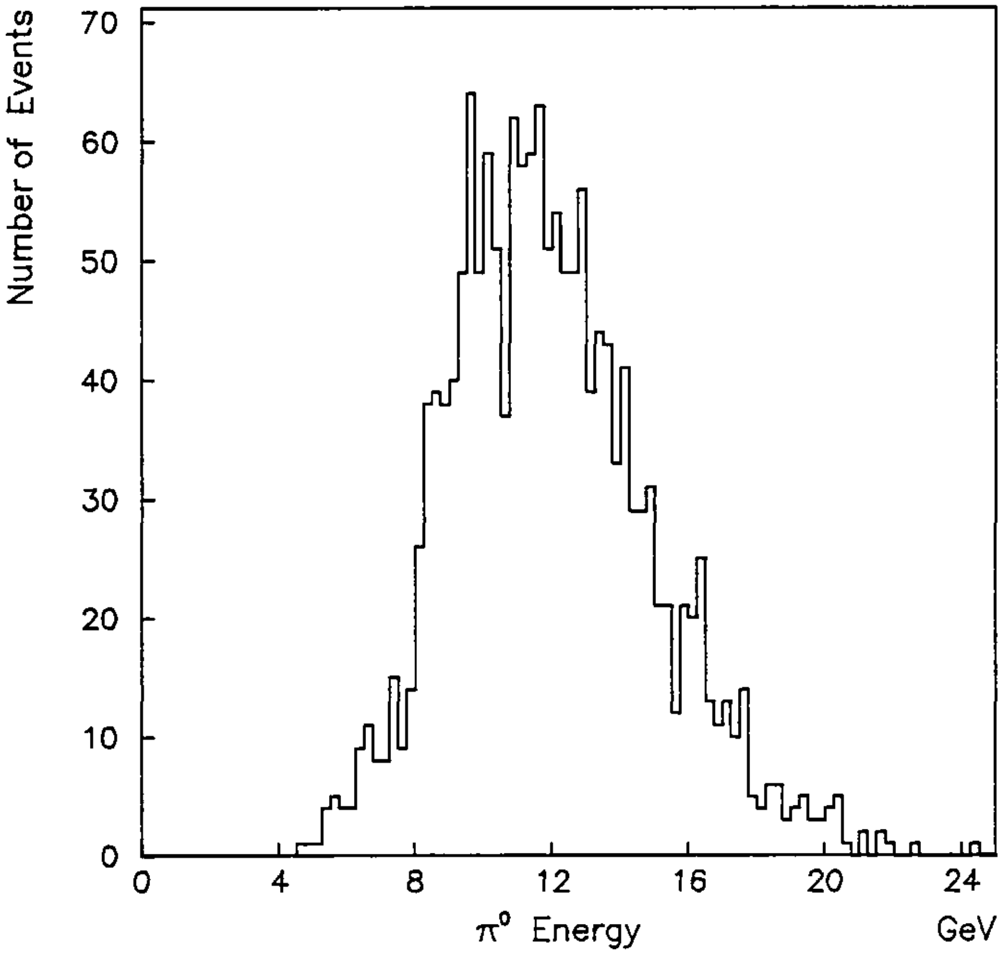
Number of Events
70
60
50
40
30
20
10
0
0
4
8
12
16
20
24
π^0 Energy
GeV

Figure 5.5

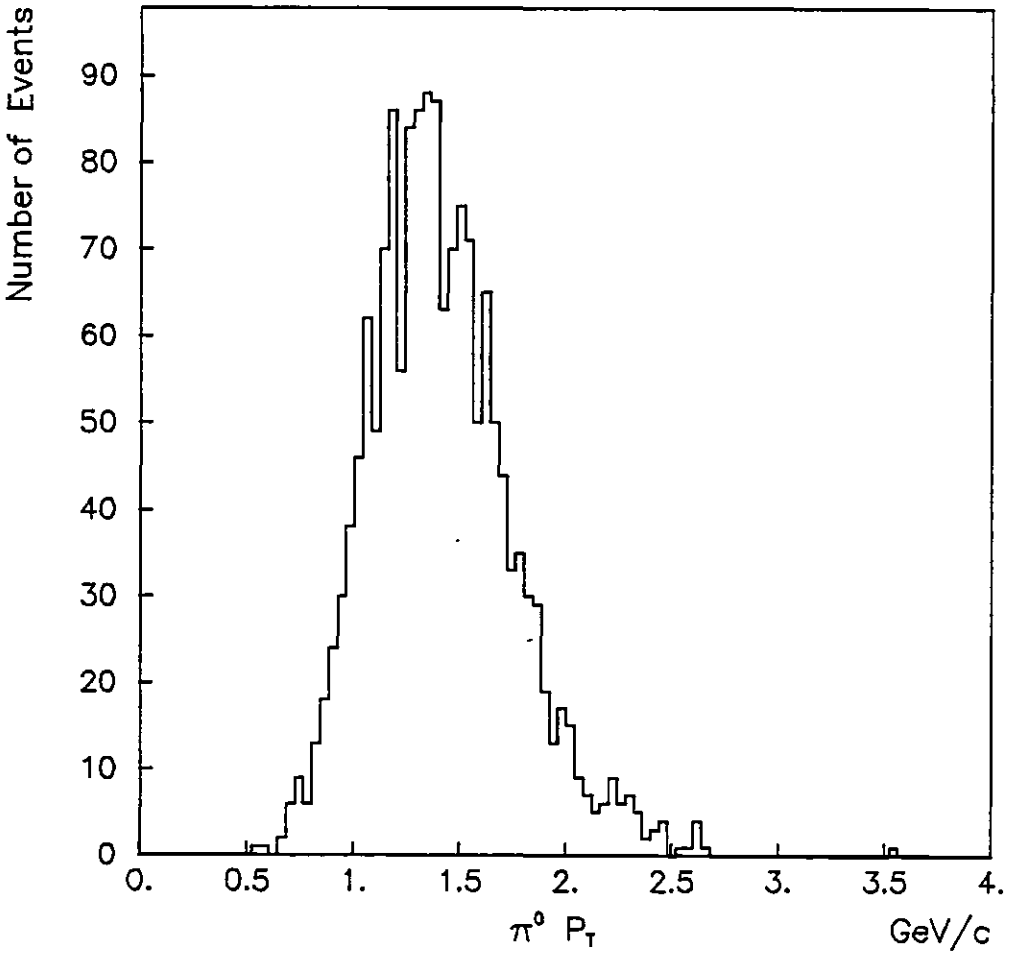
Number of Events
90
80
70
60
50
40
30
20
10
0
0.
0.5
1.
1.5
2.
2.5
3.
3.5
4.
π^0 P_T
GeV/c

3. The energy sharing procedure used when more than one cluster overlaps with a single calorimeter module.

The relative gains of the calorimeter modules are obtained from muon calibration runs at the start of an SPS period. Using this procedure, the relative gains can only be estimated to within about 10%. At present, no correction is made for drifts in gain that are known to occur over the 10 day period. In some cases the drift can be as large as 30%. Using information from the LED calibration events that are available on tape it should be possible to compensate for these gain drifts.

An estimate of the effect of asymmetric decays on the width of the π^0 signal can be made if the mean asymmetry is known. Figure 5.6 shows the distribution of the asymmetry ϵ defined as

$$\epsilon = \frac{E_1}{E_1+E_2}$$

where E_1 is the energy of the higher energy photon. It peaks at about 0.8. Assuming that all the photons from the decay of π^0's have this value of asymmetry, we have $E_1 = 9.6$ GeV and $E_2 = 2.4$ GeV. Using these values, the expected width becomes about 19 MeV. The estimate obtained from a Monte-Carlo is about 20 MeV.

The effect of incorrect energy sharing can be estimated by looking at the width of the π^0 signal for those events that have only one cluster per module. For these "clean" π^0's, the width is about 27 MeV.

Figure 5.6

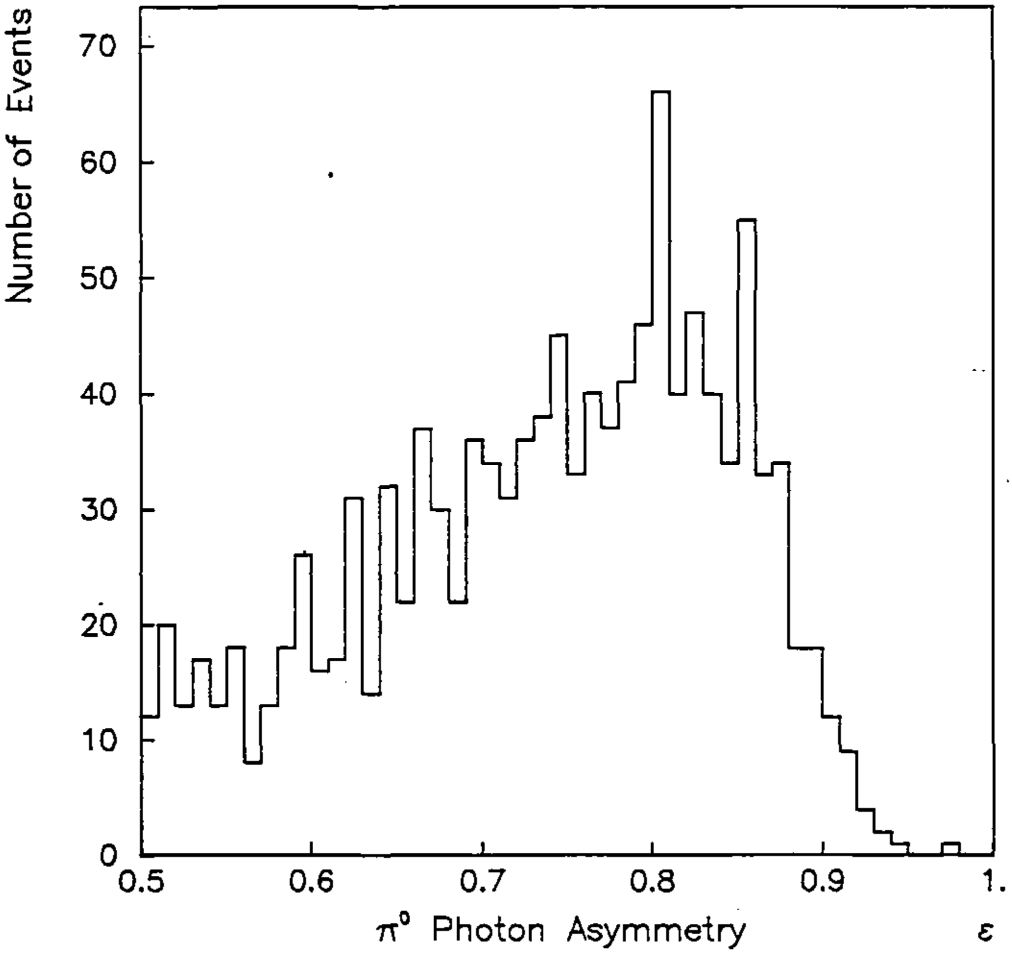
Number of Events
70
60
50
40
30
20
10
0
0.5
0.6
0.7
0.8
0.9
1.
π^0 Photon Asymmetry
ε

It would appear that a large contribution to the width of the π^0 signal comes from poor calibration and gain drifts. In principle, both of these effects can be corrected for and should result in an improvement.

5.4 Pattern Recognition Inefficiencies

There are two problems connected with the cluster association procedure; unequal numbers of clusters in the two projections and the lack of any attenuation corrections.

An unequal number of clusters could be caused by statistical fluctuations or inefficient/dead channels. The contribution from these is small. The dominant effect comes from cluster merging. If two impacts have a separation that is small in one projection, then the clusters in that projection will merge. The separation in one projection plotted against the separation in the other projection for events that have only two reconstructed clusters in each projection is shown in Figure 5.7. The effect of cluster merging begins to occur at separations of about 100 mm.

The cluster cuts require a minimum width of two strips. If two clusters are to be separated by at least one strip, this cut imposes a minimum separation of about 45 mm. In general, however, the clusters are more than two strips wide; the mean value for 6 GeV photons is about five strips. Clusters of this width will begin to merge if they are separated by less than about 90 mm, in agreement with the effect observed in Figure 5.7.

Figure 5.7

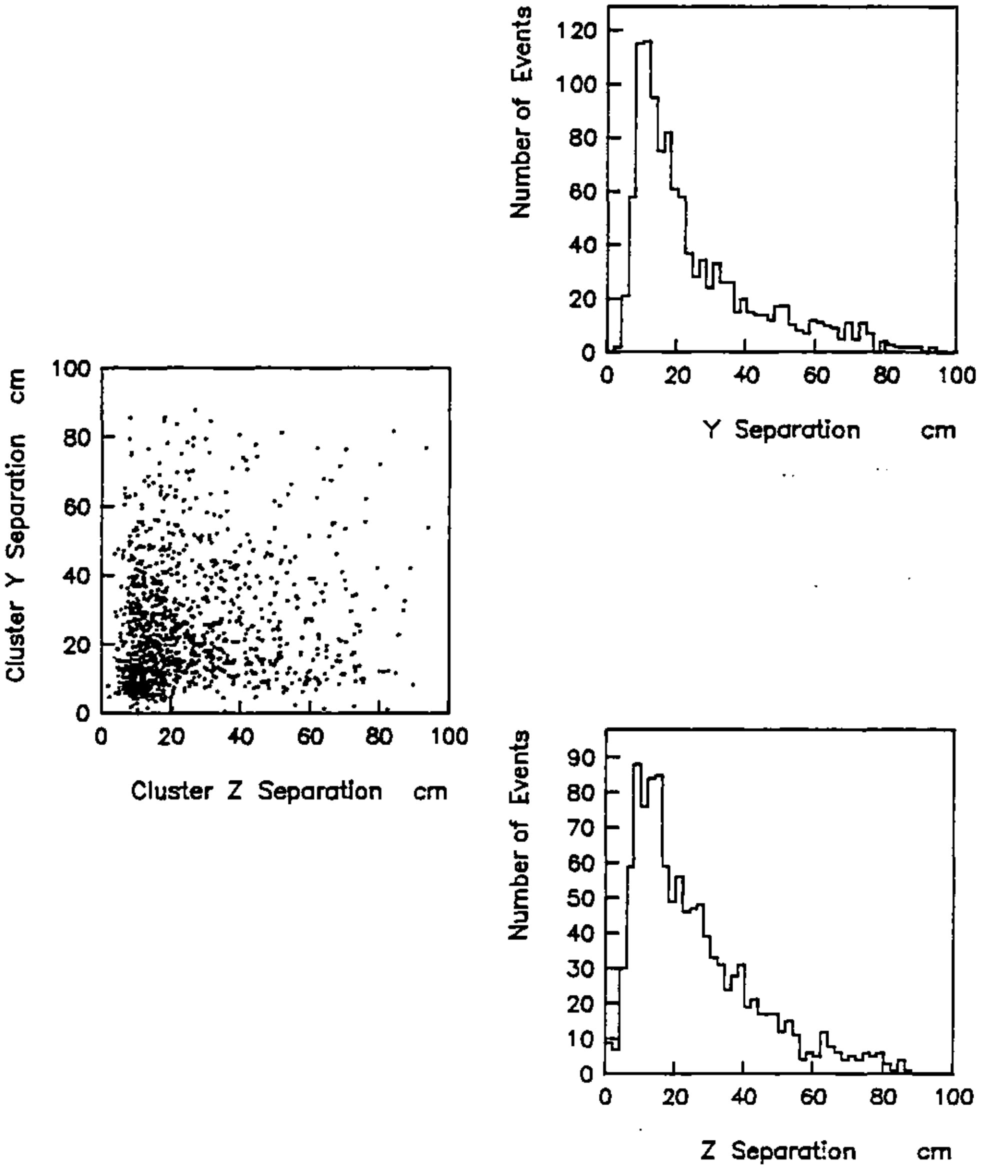
Number of Events
120
100
80
60
40
20
0
0
20
40
60
80
100
Y Separation cm
Cluster Y Separation cm
100
80
60
40
20
0
0
20
40
60
80
100
Cluster Z Separation cm
Number of Events
90
80
70
60
50
40
30
20
10
0
0
20
40
60
80
100
Z Separation cm

The effect of cluster merging on the π^0 reconstruction efficiency is quite large. A Monte-Carlo calculation indicates that about 25% of the neutral pions will decay into two photons that will be separated by less than 100 mm in at least one projection when they hit ILSA. The azimuthal angle of the π^0 decay photons is shown in Figure 5.8. This distribution should be flat and the observed fall near $\theta = 0$ and $\theta = \pm \pi/2$ is due to cluster merging. Assuming a flat distribution, an estimate of the number of undetected π^0s can be obtained. It is about 26%, in fair agreement with the Monte-Carlo prediction.

If the overlap is not too large, it should be possible to recognize the presence of two distinct peaks and thus split the cluster. A cluster splitting algorithm was developed to deal with unusually wide clusters. In order to test the algorithm, events were selected in which at least one quadrant had only one cluster in one projection and more than one cluster in the other projection and no quadrant had more than one reconstructed impact. The algorithm was applied to this sample of events and attempted to split any cluster that was more than 5 strips wide. In addition, after the split, each of the two new clusters had to have a signal equivalent to at least 5 relativistic muons. It success was limited by the large number of "false" splittings that it produced. Most of these were the result of statistical fluctuations and calibration non-uniformities that caused single clusters to appear as two merged clusters. A small fraction of the merged clusters can be recovered and a π^0 reconstructed from them. The false splittings appear as low effective mass combinations. This is shown in Figure 5.9. The small number of π^0's that are reconstructed without using the splitting algorithm are due to decays in which the photons lie in different quadrants. Clearly, more work will have to be done to resolve this problem.

The second pattern recognition problem arises from the cluster association algorithm. As stated earlier, the clusters are associated according to pulse heights that have not been corrected for attenuation. The reason for this is that the correction cannot be made until the coordinate in the other projection is known (ie. it can only be done after the association has been made). As a result, the association could be incorrect. This is of importance when the veto is imposed offline. An incorrect association would mean that the wrong veto crossing would be examined to see if it had fired.

The magnitude of the effect is estimated from a Monte-Carlo that puts in the measured Ariadne attenuation and simulates the association procedure. Assuming that Ariadne is perfectly calibrated, it predicts that about 15% of the associations will be incorrect.

A possible solution to this problem would be to adopt an iterative procedure. The clusters are associated as at present and the discrepancy between the signals in the Y and Z plane clusters is noted. The signals are then corrected for attenuation. If the initial association was incorrect, the discrepancy between the Y and Z plane signals will increase and a different association can be tried. This procedure has not yet been tested.

Figure 5.8

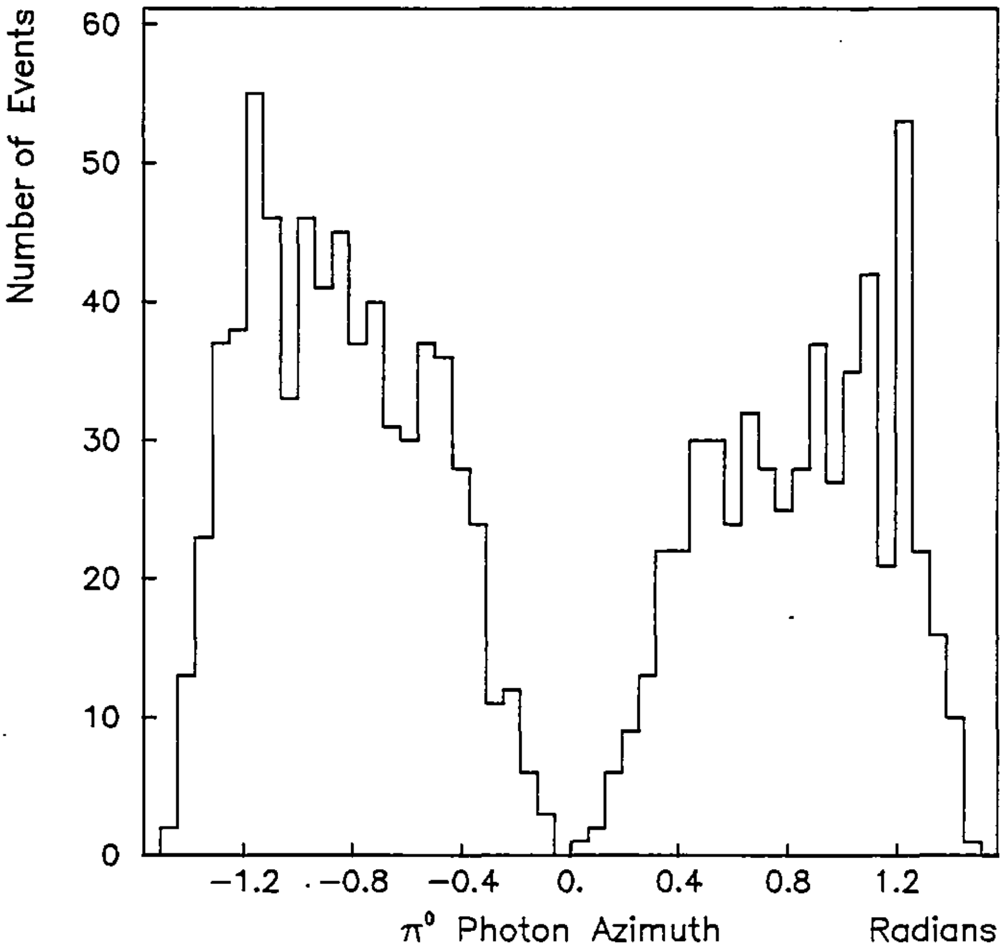

Number of Events
0
10
20
30
40
50
60
−1.2
−0.8
−0.4
0.
0.4
0.8
1.2
π^0 Photon Azimuth
Radians

Figure 5.9

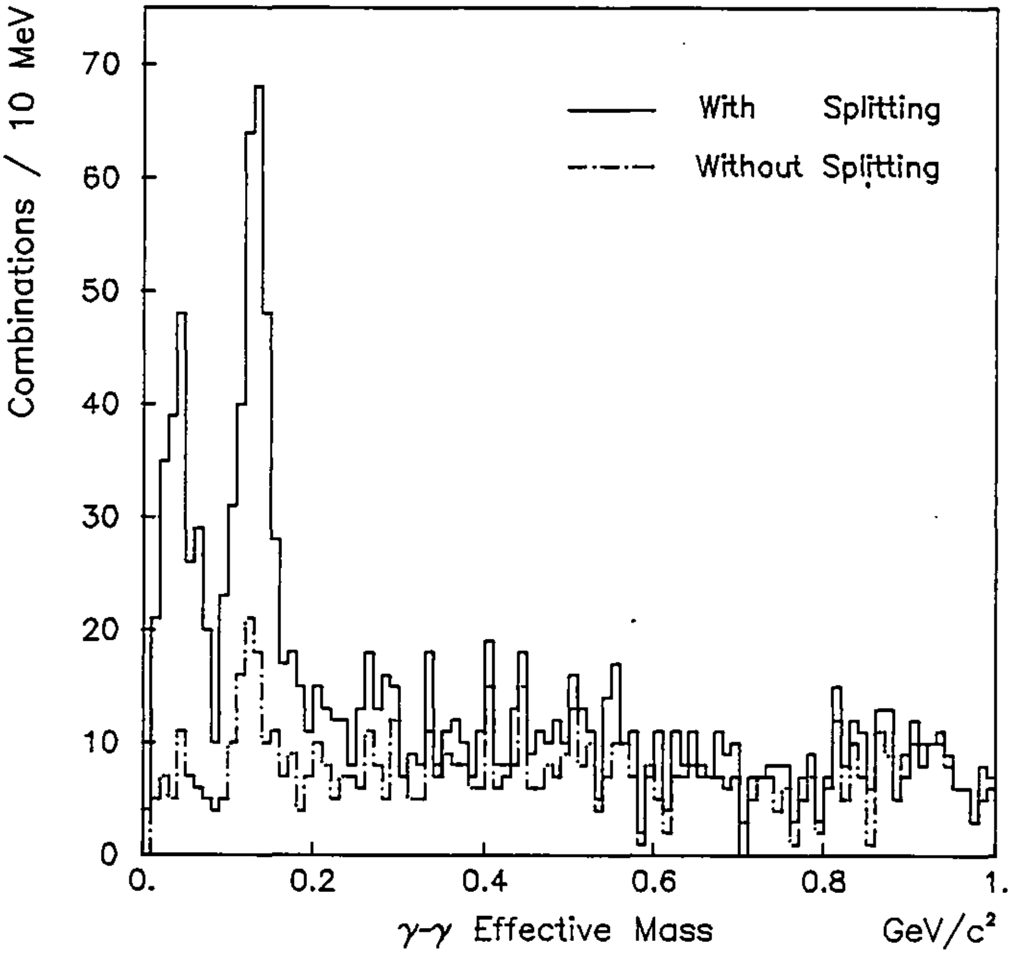
With Splitting
Without Splitting
Combinations / 10 MeV
0
10
20
30
40
50
60
70
0.
0.2
0.4
0.6
0.8
1.
γ-γ Effective Mass
GeV/c^2

5.5 Reconstruction Efficiency

Vital to the success of the experiment in its attempt to study the Compton QED process is its ability to distinguish between single photons and those that are the product of π^0 decays. Thus the question of π^0 reconstruction efficiency is an important one.

In order to estimate the number of π^0's that should be seen by ILSA, Monte-Carlo simulations were written by myself and several other members of the collaboration. These programs generated π^0's with various parametrizations of energy and P_t distributions. It was found that the ratio $R = N_p/N_t$ was relatively model independent. N_p is the number of events in which both the photons hit ILSA, at least one having a P_t greater than 1 GeV/c and the other having an energy of at least 2.0 GeV (to be well above the cut imposed by the reconstruction procedure). N_t is the number of events that should have produced an ILSA trigger ie. at least one photon having a P_t greater than 1 GeV/c hit ILSA. The predicted value of R is about 14%. The observed value, calculated from the numbers in Table 5.1 is 3.6%.

At first sight, these figures suggest a very poor π^0 reconstruction efficiency, however, the Monte-Carlo only considers geometry and the trigger threshold, several other effects have not been taken into consideration. A full Monte-Carlo simulation of ILSA is now under development and the results obtained from it will be published elsewhere [MOR].

At present, it is only possible to make a crude estimate of the contribution from the effects that have not been taken into

TABLE 5.1

Pizero Reconstruction Statistics

Total number of events processed	745754
Number of ILSA triggers	116657
Number of reconstructed photons	50840
Number of reconstructed charged hits	98403
Number of events with at least one photon having a $P_t \geq 1.0$ GeV/c	16682
Number of π^0's above background (± 10%) having one photon with a $P_t \geq 1.0$ GeV/c and the other photon with an energy ≥ 2.0 GeV	600

consideration. This will at least indicate if there are severe deficiencies in the reconstruction process.

The major contributions come from the following effects:

1. Conversion of photons before reaching ILSA. The amount of material in the region between the target and ILSA is estimated to be about 0.2 X_0 [VIR]. This will result in a loss of about 16% of the photons.
2. Non-conversion of a photon in the passive converter and the first layer of calorimeter modules. The reconstruction procedure will not find a photon if there the signal in Ariadne is less than than the equivalent of three relativistic muons. Thus if the photon does not shower in the 4.5 X_0 before it, it will not be reconstructed. An EGS Monte-

Carlo calculation performed by P. Gregory indicates that about 5% of 6 GeV photons will deposit less that the required signal in Ariadne.

3. The contribution of photons from η decay. Experiments at the ISR [KOU] have measured an η/π^0 ratio of about 0.5 at a P_t of 3 GeV/c. Since the branching ratio for $\eta \rightarrow \gamma\gamma$ is about 40%, this is a large effect that will increase the observed value of N_t by about 20%.
4. Cluster merging. The effect of cluster merging has already been discussed and it is estimated that about 25% of the neutral pions are lost because of it.
5. Veto inefficiencies. The charged particle veto is imposed offline and a hit map of the reconstructed impacts that are not considered to be photons (because the corresponding veto has fired) shows a depopulation close to the beam edge. There is a corresponding enhancement in the hit map for photons. Since there is no misalignment between the veto counters and ILSA this suggests that many charged particles, deflected by the field of Goliath, miss the veto but do hit ILSA and cause a trigger. Recall that there is a separation of about 100 mm between the veto counters and the first layer of calorimeter modules. These charged particles can be rejected when track information is available. In order to estimate the magnitude of the effect, a fiducial surface of ILSA is defined that does not include a band 100 mm wide around the edges of an ILSA quadrant,

close to the beam. The Monte-Carlo prediction for R then decreases by about 20% while the observed value of R only decreases by 10%.

The total contribution of all the above effects significantly decreases the discrepancy between the predicted and observed values of R resulting in an overall efficiency of about 70%. A more quantitative estimate can only be obtained when events generated by a full Monte-Carlo simulation are fed through the reconstruction program. For the moment, it can only be said that there does not appear to be any gross inefficiency in the reconstruction procedure.

The next step will be to tackle the so far unresolved problems of cluster association and cluster merging. This will result in a real improvement in the reconstruction efficiency and can be tested using the Monte-Carlo.

Chapter VI

PRELIMINARY RESULTS

In this chapter I shall present some preliminary results of an analysis that I have carried out on the inclusive high P_t ($\geq$ 1.7 GeV/c) spectrum of photoproduced neutral pions reconstructed by ILSA. A similar analysis has been carried out for OLGA by other members of the collaboration and their results have been presented elsewhere [PET]. A comparison is made between the spectra observed in ILSA and OLGA and the inclusive P_t spectrum of neutral pions produced in the reactions $\pi^- p \rightarrow \pi^0 X$ and $\pi^+ p \rightarrow \pi^0 X$.

At present this analysis is in its very early stages and it is clear from the preceeding chapter that problems remain to be solved in the reconstruction procedure. In view of this, the results presented here are to be regarded as being very preliminary.

6.1 Data Analysis

The data sample for the ILSA analysis is the same as that used to test the π^0 reconstruction efficiency. Any pair of photons having an effective mass lying in the range 135 ± 35 MeV/c^2 are assumed to come from the decay of a π^0. In addition, at least one of the photons must have a P_t of at least 1 GeV/c. No energy cut was imposed on the other photon in order to increase the statistics, however, as explained in the previous chapter, the reconstruction procedure effectively imposes an energy cut of 1 GeV. In order to be well above the trigger threshold, the P_t of the π^0 had to exceed 1.65 GeV/c. A total of 342 events survive all these cuts and an estimated 75% of them are above background.

A full Monte-Carlo simulation of ILSA is not available at present so it is not possible to correct the data for all the reconstruction inefficiencies mentioned in the previous chapter. However, the correction that would have to be applied to compensate for them should be relatively independent of P_t.

In order to compare these results with the inclusive spectrum of neutral pions produced in $\pi^- p$ and $\pi^+ p$ interactions, the parametrization of Donaldson et. al. [DON] is used. They have measured the angular dependence of inclusive π^0 production in the above interactions at energies of 100 and 200 GeV and have fitted their data for $x_l \lesssim 0.8$ ($x_l = [P_l/P_{max}]_{cm}$) with a parametrization of the form

$$E \frac{d^3\sigma}{dp^3} = A \frac{(1 - x_d)^f}{(P_t^2 + m^2)^n} \quad \mu b/GeV^2$$

where $x_d = \sqrt{x_t^2 + (x_l - x_0)^2}$ and $x_t = [P_t/P_{max}]_{cm}$. The parameters A, f, x_0, n and m^2 are given for incident π^+ and π^-.

Using this parametrization, it should be possible to estimate the VMD contribution to photoproduction at large P_t. If all VMD contributions to the photon structure, apart from the low mass vector mesons (ρ^0,ω^0), are neglected, then one can relate large P_t particle production induced by the photon to the average of that induced by π^+ and π^-. The normalization between the two can be obtained from the relations

$$\sigma_{tot}(\rho^0 p) = \frac{1}{2} [\sigma_{tot}(\pi^+ p) + \sigma_{tot}(\pi^- p)] \simeq 25 \text{ mb}$$

$$\sigma_{tot}(\gamma p) \simeq 125 \ \mu\text{b}$$

Averaging the parameters for π^+ and π^- given by Donaldson et. al. and introducing the normalization factor gives the following values for the parameters;

$A = 51.93$, $f = 3.21$, $x_0 = 0.14$, $n = 5.03$ and $m^2 = 0.96$

Taking a fixed incident photon energy of 100 GeV, a Monte-Carlo is used to generate neutral pions with x_t and x_l distributions according to the above parametrization. The ILSA trigger P_t and reconstruction procedure energy cuts are introduced and the P_t spectrum of neutral pions that should be detected in ILSA is computed. Since no absolute normalization is available at this stage, this spectrum is normalized to the number of events actually reconstructed in ILSA at a P_t of 1.7 GeV/c.

The data sample for the OLGA analysis was collected during a test period in November 1981 with similar beam and trigger conditions to the sample used for the ILSA analysis. It is not possible to perform the ILSA analysis on the same data because at that stage ILSA was not operating satisfactorily. Thus there is no relative normalization between the two results. However, the same Monte-Carlo is used to compute the P_t spectrum of neutral pions that should be reconstructed by OLGA and this spectrum is again normalized to the number of events actually reconstructed by OLGA at a P_t of 1.7 GeV/c.

6.2 The Inclusive π^0 P_t Spectrum

The inclusive π^0 P_t spectrum reconstructed in ILSA and OLGA is shown in Figures 6.1 and 6.2 respectively. The result obtained from the Monte-Carlo calculation is also shown.

For ILSA, apart from the data point at 2.1 GeV/c, the results agree very well with the Monte-Carlo. Given the rather poor statistics, the uncertainties in the acceptance and in the muon induced background at high P_t, it is not possible to draw any firm conclusions at this stage. The P_t spectrum seems to agree with that observed in π^-p and π^+p interactions up to a P_t of about 2.5 GeV/c suggesting that contributions from the non VMD nature of the photon will only begin to appear at values of P_t greater than 3.0 GeV/c.

The results for OLGA show a similar agreement with the Monte-Carlo and do not contradict the results obtained for ILSA. The spectrum for OLGA, apart from the few events above 3 GeV/c of P_t, falls more rapidly with P_t than the spectrum for ILSA. However, this difference is also observed in the Monte-Carlo.

6.3 Conclusions

While this analysis was being performed, the statistics has been increased by a factor of at least 20. Several members of the collaboration have been working on the unsolved problems in the reconstruction procedure and in developing a full Monte-Carlo simulation of ILSA and the other two calorimeters. When this is done it will be possible to make accurate corrections for the acceptance.

Figure 6.1

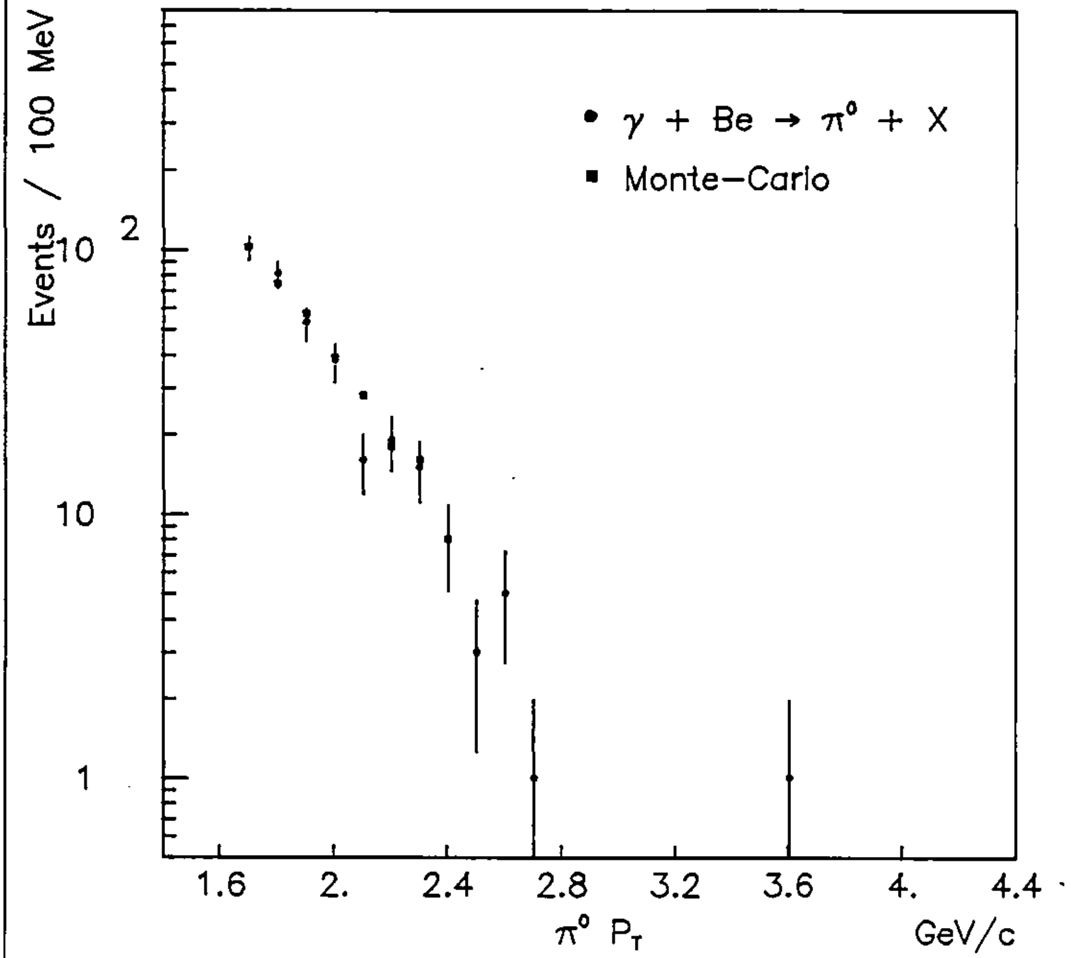

ILSA

Figure 6.2

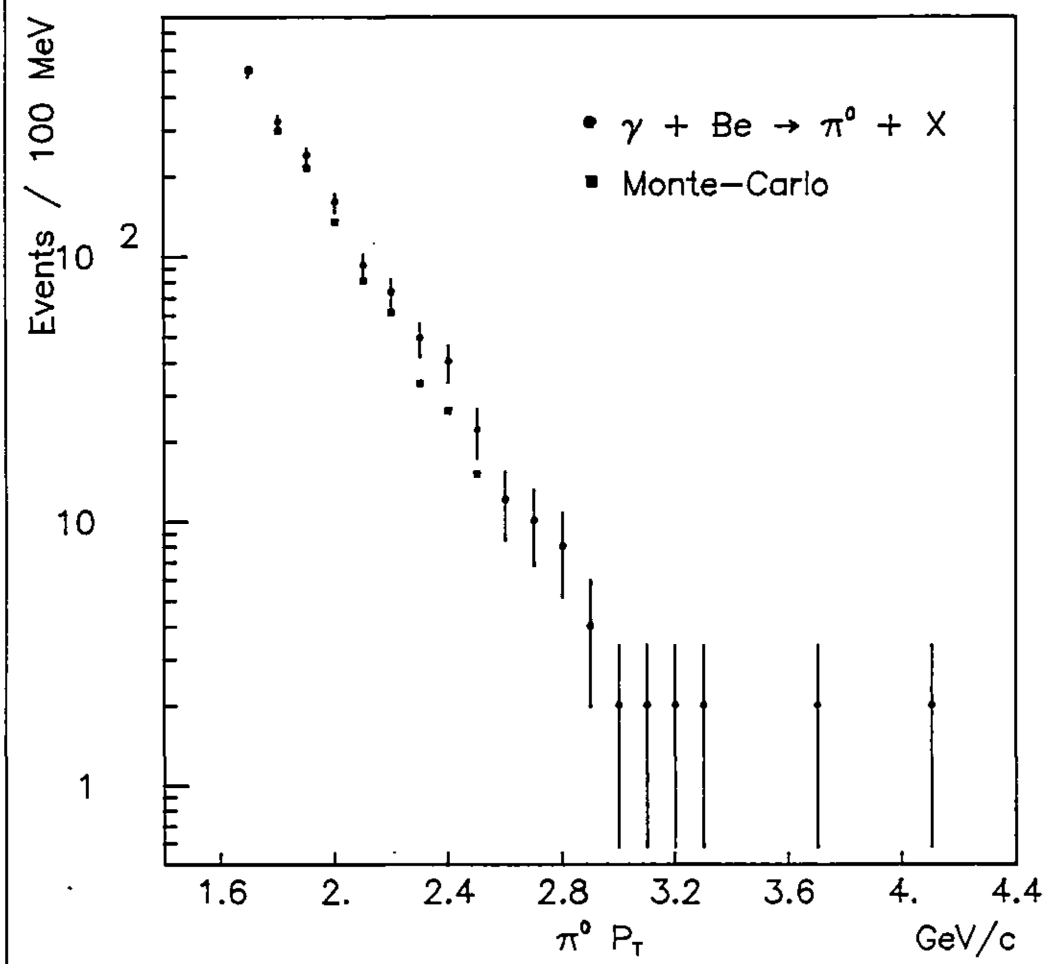

OLGA

The next stage will be to combine the data from the different calorimeters. This will result in a large increase in the acceptance for neutral pions and also enable a better selection of single photon candidates. Much work has been done on the rejection of the muon induced background at high P_t and will enable a more confident estimate of the single photon and π^0 P_t spectrum to be made. Hopefully, the experiment will then be able to answer some questions on the structure of hadrons and the interesting nature of the photon.

REFERENCES

[ABS] G. Abshire et. al. NIM 164 (1979) 67

[AKO] G.A. Akopdjanov NIM 140 (1977) 441

[AMA] U. Amaldi CERN-EP/80-212

[BAT] G. Bathow Nucl. Phys. B20 (1970) 592

[BUS] Yu. B. Bushnin et. al. NIM 120 (1974) 391

[COU] F. Couchot Ph.D Thesis,LAL Orsay,LAL 80-04

[CRA] C.J. Crannel et. al. Phys. Rev. 182 (1969) 1435

[CRAW] D.F. Crawford & H. Messel Phys. Rev. 128 (1962) 2352

[DON] G. Donaldson et. al. Phys. Lett. 73B (1978) 375

[ELL] J. Ellis et. al. Nucl. Phys. B111 (1976) 253

[FAB] C.W. Fabjan & T. Ludlam CERN-EP/82-37

[FEY77] R. P. Feynman & R. D. Field Phys. Rev. D15 (1977) 2590

[FEY78] R. P. Feynman et. al. Phys. Rev. D18 (1978) 3320

[FIS] G. Fisher NIM 156 (1978) 81

[FOR] R.L. Ford & W.R. Nelson SLAC-210 (1978)

[HIT] D. Hitlin et. al. NIM 137 (1976) 225

[IGU] K. Iguchi & A. Niegawa OCU-69 (1980) Osaka Preprint

[IGU80] K. Iguchi et. al. Progr. Theor. Phys. 63 (1980) 1711

[IWA] S. Iwata DPNU-3-79

[KAT] T. Katsura et. al. NIM 105 (1972) 245

[KOU] C. Kourkoumelis et. al. Phys. Lett. 84B (1979) 277

[LLE] C. H. Llewellyn Smith Phys. Lett. 79B (1978) 83

[LON] E. Longo & I. Sestili NIM 128 (1975) 283

[MOR] J. Morris Ph.D Thesis,Univ. of London,to be published

[NAG] H.H. Nagel Z. Physik 186 (1965) 319

[NEL] W.R. Nelson Phys. Rev. 149 (1966) 201

[ONL] CERN OC-DEC On-line Data Acquisition System Manual

[PET] P. Petroff XVII Rencontre de Moriond, Les Arcs, 1982

[PIN] K. Pinkau Phys. Rev. 139 (1965) B1548

[ROS] B. Rossi High Energy Particles
Prentice-Hall,New York (1952)

[VIR] T. Virdee Private Communication

[WIN] M. Winter Ph.D Thesis,CRN Strasbourg,CRN/HE 81-03

[WIT] E. Witten Nucl. Phys. B120 (1977) 189

[WYL] A. Wylie Ph.D Thesis,Univ. of London,1979

[YUD] T. Yuda NIM 73 (1969) 301